



DISSERTATION

Simulation of the dynamics of laser-cluster interaction

ausgeführt zum Zwecke der Erlangung des akademischen Grades eines
Doktors der technischen Wissenschaften

unter der Leitung von

O.Univ.Prof. Dipl.-Phys. Dr.rer.nat. Joachim Burgdörfer
Institut für Theoretische Physik (E136)

eingereicht an der Technischen Universität Wien
Fakultät für Physik

von

Cornelia Deiss
Matrikelnummer: 9925280
Rechte Wienzeile 9/3
1040 Wien

Wien, am 30. Januar 2009

Kurzfassung

Mit Größen von einigen Dutzend Atomen bis hin zu mehreren Millionen Atomen bilden Cluster ein Zwischenstadium zwischen Gasen und Festkörpern. Die bei der Bestrahlung von Clustern mit kurzen Laserpulsen im Femtosekundenbereich beobachteten hochgeladenen schnellen Ionen, hochenergetischen Elektronen, sowie UV- und Röntgenphotonen, zeugen von einem äußerst effizienten Energietransfer. Die Größe des Systems und die Fülle von physikalischen Vorgängen stellen eine wesentliche Herausforderung für eine theoretische Beschreibung der Wechselwirkung dar. Im Rahmen dieser Dissertation wurde eine "Classical Trajectory Monte Carlo" Simulation entwickelt, welche Einblicke in die Teilchendynamik während der Wechselwirkung von Laserpulsen mit großen Argonclustern (mit mehr als 10000 Atomen) gewährt. Elastische Elektron-Ion Streuung, Elektron-Elektron Streuung, Elektronenstoßionisation und -anregung, sowie Dreikörperrekombination und Auger Zerfall wurden als stochastische Prozesse implementiert. Stark vereinfacht lässt sich die Dynamik wie folgt zusammenfassen: das starke Laserfeld ionisiert die Clusteratome und treibt die quasifreien Elektronen. Durch Stoßionisation werden weitere freie Elektronen und hohe ionische Ladungszustände produziert. Sobald einige der freien Elektronen den Cluster verlassen, fühlen die Ionen eine positive Gesamtladung. Der Cluster beginnt zu expandieren und zerfällt schlussendlich in einer Coulomb Explosion. Selbst bei gemäßigten Laserintensitäten (ca. 10^{15} Wcm^{-2}) kommt es während des Laserpulses zur Erzeugung von Löchern in den innersten atomaren Schalen durch Stoßionisation, was zur Emission von charakteristischer Röntgenstrahlung führt. Die hierzu benötigte kleine Population von hochenergetischen Elektronen wird in der Nähe der Clusterpole erzeugt, wo die Kombination von Aufladung und Polarisation des Clusters zu stark erhöhten elektrischen Feldstärken führt. Die aus der Simulation gewonnenen quantitativen Voraussagen für die Röntgenemission stimmen über weite Parameterbereiche sehr gut mit Röntgenspektroskopieexperimenten überein. Die Abhängigkeit der Röntgenausbeute von der Laserintensität, Pulslänge und Clustergröße wurde untersucht. Hierbei wurde klar, dass zur Beschreibung gewisser Parameterabhängigkeiten die Emissionseffizienz eines einzelnen Clusters nicht alleine ausreicht, sondern auch die Veränderung der Gesamtzahl an emittierenden Clustern im Laserfokus in Betracht gezogen werden muss.

Abstract

Ranging in size from a few atoms to several million atoms, clusters form a link between gases and solids. When irradiating clusters with intense femtosecond laser pulses, the production of energetic and highly charged ions, hot electrons, and extreme UV and X-ray photons, gives evidence of a very efficient energy conversion. The size of the system and the multitude of mechanisms at play provide a considerable challenge for the theoretical treatment of the interaction. In this thesis, we have developed a Classical Trajectory Monte Carlo simulation that gives insight into the particle dynamics during the interaction of laser pulses with large argon clusters (with more than 10000 atoms per cluster). Elastic electron-ion scattering, electron-electron scattering, electron-impact ionization and excitation, as well as three-body recombination and Auger decay are included via stochastic events. In a strongly simplified picture, the dynamics of the laser-cluster interaction can be summarized as follows: the intense laser field ionizes the cluster atoms and drives the population of quasi-free electrons. In collision events, further free electrons and high ionic charge states are created. As some electrons leave the cluster, the ions feel a net positive charge, and the cluster ultimately disintegrates in a Coulomb explosion. Even at moderate laser intensities (approx. 10^{15} Wcm^{-2}), impact ionization produces inner-shell vacancies in the cluster ions that decay by emitting characteristic X-ray radiation. The small population of fast electrons responsible for these ionization events is produced near the cluster poles, where the combination of polarization and charging of the cluster leads to strongly enhanced field strengths. We achieve a good agreement over large parameter ranges between the simulation and X-ray spectroscopy experiments. We also investigate the dependence of X-ray emission on laser intensity, pulse duration and cluster size. We find that in order to understand certain parameter dependencies, one needs to consider the impact of the parameter variation on both the emission from a single cluster and on the total number of emitting clusters.

Contents

| | | |
|-----------|--|-----------|
| 1 | Introduction | 1 |
| I | Numerical Model | 6 |
| 2 | Basic ingredients | 7 |
| 2.1 | Crystalline structure and initial conditions | 7 |
| 2.2 | Test particle discretization | 7 |
| 2.3 | Equations of motion | 8 |
| 3 | Evaluation of the mean-field | 11 |
| 3.1 | Space discretization | 11 |
| 3.2 | Solving the Poisson equation | 13 |
| 4 | Elastic scattering processes | 17 |
| 4.1 | Elastic electron-ion scattering | 17 |
| 4.2 | Electron-electron scattering | 19 |
| 5 | Ionization, excitation and recombination | 22 |
| 5.1 | Modeling the argon ion | 22 |
| 5.2 | Field ionization | 25 |
| 5.3 | Electron-impact ionization | 26 |
| 5.4 | Electron-impact excitation | 27 |
| 5.5 | Three-body recombination | 29 |
| 5.6 | Auger decay | 30 |
| II | Single cluster results | 32 |
| 6 | Charge distribution and mean field | 35 |
| 6.1 | Cluster polarization | 35 |
| 6.2 | Cluster charging | 39 |

| | |
|---|------------|
| 7 Ionization of the cluster ions | 41 |
| 8 Electron dynamics | 45 |
| 8.1 Energy distributions | 45 |
| 8.2 Fast-electron dynamics | 47 |
| 8.3 Wake fields | 51 |
| 9 Cluster disintegration | 57 |
| 9.1 Ion dynamics | 57 |
| 9.2 Dynamics inside an expanded cluster | 59 |
| 9.3 Influence on the K-shell vacancy production | 61 |
| III Comparison with X-ray spectroscopy | 66 |
| 10 Description of the experiments | 67 |
| 11 Extracting X-ray yields | 70 |
| 11.1 From inner-shell vacancies to X-rays | 70 |
| 11.2 Absolute X-ray yield | 70 |
| 12 Laser intensity | 73 |
| 12.1 Absolute X-ray yields | 73 |
| 12.2 Charge state distributions | 75 |
| 13 Pulse duration | 79 |
| 13.1 Absolute X-ray yields | 79 |
| 13.2 Effect of ion shielding | 80 |
| 13.3 Charge state distributions | 82 |
| 13.4 Evolution of the X-ray yield at constant laser energy | 84 |
| 13.5 Evolution of the X-ray yield at constant laser intensity | 87 |
| 14 Cluster size | 89 |
| 15 Conclusion and Outlook | 96 |
| Appendix | 102 |
| A Time propagation | 102 |
| B The chaining mesh | 103 |

| | |
|---|------------|
| C Calculating the mean field | 105 |
| C.1 Cloud-in-Cell charge assignment | 105 |
| C.2 Cyclic reduction | 106 |
| C.2.1 Inverting the matrix | 107 |
| C.2.2 Buneman scheme | 108 |
| C.2.3 Summary | 108 |

| | |
|---------------------|------------|
| Bibliography | 110 |
|---------------------|------------|

Chapter 1

Introduction

Ranging in size from a few atoms to several million atoms agglomerated at solid densities, clusters form a link between gases and solids. When exposed to laser radiation, clusters combine advantages of both phases. On the one hand, since the *local* atomic density in the cluster is close to a solid ($n_{\text{local}} \sim 10^{22}$ atoms/cm³), the absorption of the laser pulse energy is locally as strong as in laser-solid interactions. On the other hand, the low *mean* atomic density of the cluster jet ($n_{\text{mean}} \sim 10^{14}$ to 10^{17} atoms/cm³) ensures a debris-free interaction, just as a gaseous target. Moreover, the large distance between the clusters (of the order of micrometers) allows for the study of the response of individual clusters in a well-defined laser field, undisturbed by propagation effects. Features such as the production of energetic and highly charged ions [Ditmire et al., 1997], ejection of hot electrons [Springate et al., 2003], or the emission of extreme UV and X-ray photons [Dobosz et al., 1997; Kumarappan et al., 2001b; Rozet et al., 2001], give evidence of the very efficient coupling to an infrared laser field and have made the interaction of intense short and ultra-short laser pulses with clusters a topic of considerable interest over the past decade [Krainov and Smirnov, 2002]. A potential application of these systems would be as debris-free sources for ultrafast X-ray diagnostics, but to this end further optimization is needed [Fukuda et al., 2004, 2008]. This calls for a deeper investigation of the mechanisms relevant to the efficient energy conversion during the laser-cluster interaction.

In a strongly simplified picture, the dynamics of the laser-cluster interaction in the tunneling regime can be summarized as follows (see fig. 1.1 and Deiss et al. [2005, 2006a,b,c]): the intense laser field ionizes the cluster atoms and drives the population of quasi-free electrons. The electrons can further ionize the cluster ions in collision events and, depending on their kinetic energy, create inner-shell vacancies in the cluster ions. These vacancies decay emitting characteristic X-ray radiation. As some electrons leave the cluster,

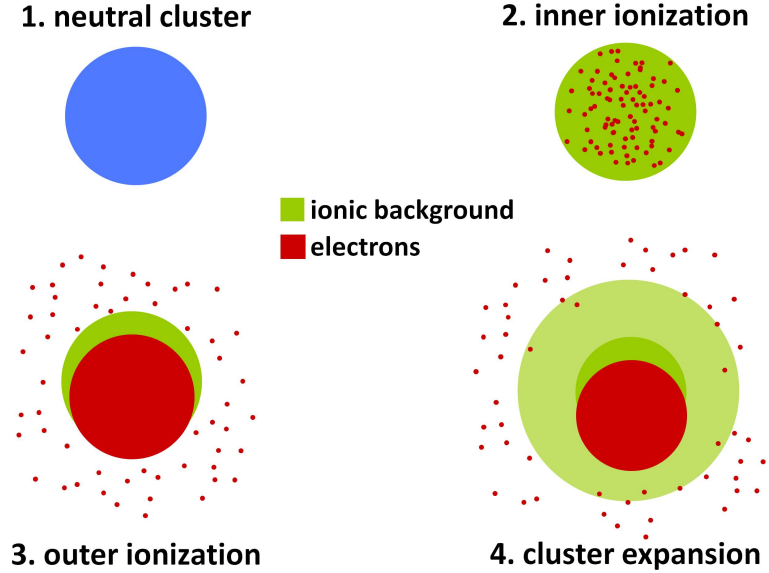


Figure 1.1: Stages of the cluster dynamics.

the ions feel a net positive charge, and the cluster ultimately disintegrates in a Coulomb explosion.

The size of the system and the multitude of mechanisms at play provide a considerable challenge for the theoretical treatment of the interaction [Saalman et al., 2006]. The description of this system unites aspects of atomic physics, plasma physics, as well as solid-state and surface physics. One approach to the problem is treating the cluster as a “nanoplasma” exposed to a laser field [Ditmire et al., 1996; Micheau et al., 2008]. In this model, energy absorption occurs predominantly at the so-called “nanoplasma resonance” when, during the cluster expansion, the plasma frequency in the cluster matches the laser frequency. The inclusion of the cluster boundaries and of an inhomogeneous ionic background during the expansion is however problematic within this theoretical framework [Megi et al., 2003]. The more straight-forward approach of molecular dynamics simulations is limited to clusters of about 1000 atoms [Fennel et al., 2007b; Georgescu et al., 2007; Rose-Petruck et al., 1997; Saalman and Rost, 2003], and the scaling to larger cluster sizes is involved [Last and Jortner, 2007]. Clusters of $\sim 10^4$ atoms have been simulated using a microscopic particle-in-cell (MPIC) code [Jungreuthmayer et al., 2004], but typical runs of such codes take several weeks, making the in-depth study of the parameter dependencies tedious and im-

practical. For large clusters, the method of choice appears to be a mean field approach, for example implemented as particle-in-cell (PIC) simulation [Fukuda et al., 2006; Taguchi et al., 2004]. In this case, particular attention has to be paid to the correct inclusion of particle-particle effects otherwise neglected or underestimated due to the averaging over several particle positions [Deiss et al., 2006b].

From an experimental point of view, the spectroscopy of the emitted electrons (see for example Lezius et al. [1997] and Kumarappan et al. [2001a]) and ions (for example Kumarappan et al. [2003] or Fennel et al. [2007a]) gives information on the system a few microseconds after the femtosecond laser pulse and the cluster disintegration. X-ray spectroscopy, on the other hand, presents the advantage of measurements on a much shorter time-scale, down to a few femtoseconds [Dobosz et al., 1997; Lamour et al., 2005]. The inner-shell vacancies responsible for the observed characteristic X-ray radiation in the keV range can not be explained by field ionization unless laser pulses with a peak intensity of the order of $I \sim 10^{21} \text{ Wcm}^{-2}$ are involved. Consequently, at lower laser intensities, the origin of these vacancies must be impact ionization by energetic electrons. The X-ray emission thus probes the high energy tail of the electron energy distribution, thereby providing valuable insights into the electronic dynamics, which are the key to a detailed theoretical understanding of the laser-cluster interaction.

Recent experiments [Lamour et al., 2005; Prigent, 2004] on rare-gas clusters found an unexpectedly low laser intensity threshold for X-ray production. When irradiating large clusters of $N > 10000$ argon atoms with infrared ($\lambda = 800 \text{ nm}$) laser pulses of duration $\tau = 61 \text{ fs}$ (at full width half maximum), characteristic $K\alpha$ X-ray radiation (3.1 keV) could be measured for laser intensities as low as $I_{th} \approx 1.9 \cdot 10^{15} \text{ Wcm}^{-2}$ (see fig. 1.2). At first glance, the electrons in the cluster appear to be mainly accelerated by the laser field. The maximum energy a free electron can reach in an oscillating laser field is equal to twice the ponderomotive energy U_P :

$$U_P[\text{eV}] = 9.33 \cdot 10^{-20} \lambda^2[\text{nm}] I[\text{Wcm}^{-2}]. \quad (1.1)$$

One would expect a threshold for the production of inner-shell vacancies by electron-impact ionization, that corresponds to the intensity, where the laser accelerates the free electrons to the binding energy of the inner-shell electrons. However, at the experimentally measured threshold intensity, one only has $2U_P \approx 225 \text{ eV}$. This value is more than an order of magnitude below the binding energy $E_K = 3.1 \text{ keV}$ of K-shell electrons in argon. In fact, the condition $2U_P = E_K$ is only fulfilled for $I \approx 2.6 \cdot 10^{16} \text{ Wcm}^{-2}$. This first observation already points to the presence of additional efficient heating

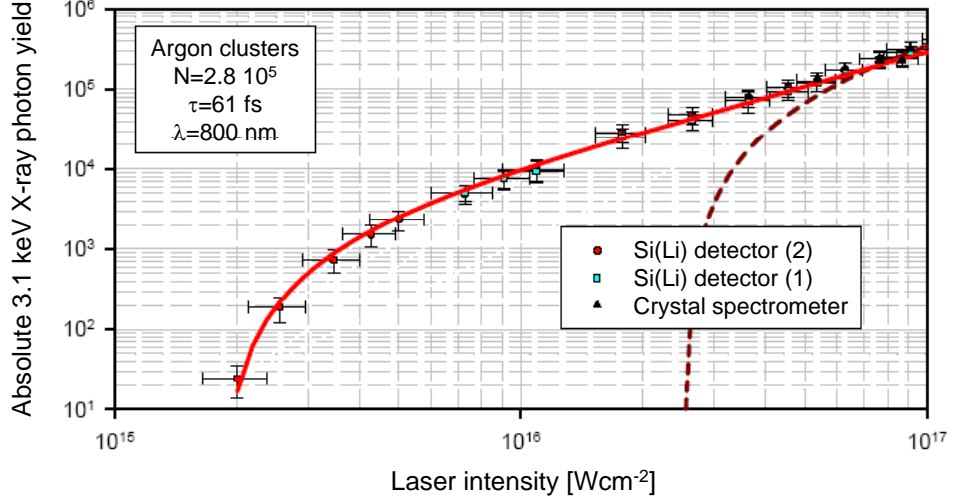


Figure 1.2: Experimentally measured intensity dependence of the absolute X-ray yield for $\lambda = 800$ nm, $\tau = 61$ fs and $N = 2.8 \cdot 10^5$ argon atoms per cluster [Prigent, 2004]. The intensity threshold for X-ray production lies at $I_{th} \approx 1.9 \cdot 10^{15} \text{ Wcm}^{-2}$. The dashed line indicates the position of the threshold predicted by $2U_P = E_K$ (see text).

mechanisms at play in a cluster environment, which allow the electrons to be effectively accelerated well beyond the ponderomotive energy. Furthermore, high resolution X-ray spectroscopy reveals that the X-rays are emitted from highly charged argon ions (mean charge state Ar^{14+}), which raises questions as to the ionization mechanisms at work.

The aim of this thesis is to elucidate the dynamics of the laser-cluster interaction theoretically. To this end we have developed a mean-field particle simulation which we describe in detail in part I. In part II, we analyze in detail the interaction of a single cluster with an infrared laser pulse. A special focus will be put on understanding the dynamics of the fast electrons, which are at the origin of the inner-shell vacancies responsible for the emission of X-ray photons. A comparison of simulation data and experimental results from X-ray spectroscopy will be performed in part III. To this end the emission from

cluster distributions has to be taken into account, as the clusters experience different peak laser intensities depending on their position in the laser beam. The influence of parameters such as laser intensity, pulse duration or cluster size on the X-ray emission will also be investigated.

Part I
Numerical Model

Chapter 2

Basic ingredients

2.1 Crystalline structure and initial conditions

The crystalline structure of argon clusters with more than approximately 1000 atoms is still a matter of debate. Random alternations between face-centered cubic (fcc) and hexagonal-close packed (hcp) have been observed [van de Waal et al., 2000]. We opt for the bulk arrangement of solid argon [Gray, 1963] and fix the initial positions of the argon atoms on a fcc lattice with a lattice constant of 10.06 a.u. (5.32 Å). This yields an atomic density of $n_{\text{Ar}} = 3.9 \times 10^{-3}$ a.u. ($2.66 \times 10^{22} \text{ cm}^{-3}$) and a nearest-neighbor distance of 7.1 a.u.. The crystal is cut to form a sphere of radius $R_{cl} = (N/(4\pi/3n_{\text{Ar}}))^{1/3}$ determined by the number N of atoms in the cluster. The crystal is turned by a random angle to avoid any alignment of the laser polarization with a low-order symmetry axis of the lattice. All electrons ionized during the simulation are initialized at the position of their parent atom (or ion) with zero velocity. The simulations show little sensitivity to the precise initial conditions, yielding the same results when the atoms are initially distributed randomly in the cluster sphere (provided the correct density n_{Ar} is maintained), or when the ionized electrons are placed at a given distance from the parent ions.

2.2 Test particle discretization

The large size of the clusters in the experiments with $N \sim 10^4 - 10^6$ argon atoms calls for a test-particle representation of the ionic and electronic ensembles. The representation fraction $\alpha_{rep} = N_{\text{simul}}/N$ relates the actual number of cluster atoms N and the number of atoms N_{simul} treated explicitly in the simulation. The N_{simul} test-atoms are chosen randomly from the

N atoms initialized on the crystalline lattice. As the electronic ensemble is created by ionization of the test-atoms (or ions), the same representation fraction α_{rep} is valid for the number of simulated electrons. In the course of the simulation, all quantities related to the number of particles have to be scaled by α_{rep} . Depending on computer resources, cluster size and pulse length, representation fractions of $\alpha_{rep} = 0.1 - 1$ are chosen.

2.3 Equations of motion

Due to the large number of particles, a full ab-initio approach (e.g. via a molecular dynamics simulation) still seems impractical with today's computer resources. We therefore introduce some major simplifications to the computational treatment of the system. We opt for a Classical Trajectory Monte Carlo (CTMC) simulation with a mean field approach. This ensures that collisional events between particles, which are neglected by the mean field treatment, are included in the simulation via stochastic forces.

The test-particle ensemble consisting of $k = 1, \dots, \alpha N_e(t)$ quasi-free electrons and $j = 1, \dots, N_{\text{simul}}$ ions with mass M and charge state $q_j(t)$ obeys the following Langevin equations (atomic units are used unless otherwise stated):

$$\ddot{\mathbf{r}}_k^{(e)} = -\mathbf{F}_L(t) - \mathbf{F}_{\text{mean}}(\mathbf{r}_k^{(e)}, t) + \mathbf{K}_{\text{stoc}}(\mathbf{r}_k^{(e)}, \dot{\mathbf{r}}_k^{(e)}, t), \quad (2.1a)$$

$$M\ddot{\mathbf{r}}_j^{(i)} = q_j(t)\mathbf{F}_L(t) + q_j(t)\mathbf{F}_{\text{mean}}(\mathbf{r}_j^{(i)}, t). \quad (2.1b)$$

These equations of motion are solved using the velocity Verlet algorithm (see appendix A). All particles move in the laser field $\mathbf{F}_L(t)$ and the position dependent mean field $\mathbf{F}_{\text{mean}}(\mathbf{r}, t)$. The stochastic forces $\mathbf{K}_{\text{stoc}}(\mathbf{r}_k^{(e)}, \dot{\mathbf{r}}_k^{(e)}, t)$ represent the stochastic momentum changes the electrons experience due to collision events. This approach can also be viewed as a generalization of classical transport theory (CTT) [Burgdörfer and Gibbons, 1990] for a dynamical system open to both particle number variation $N_e(t)$ and energy exchange with the many-particle reservoir (ions and electrons), as well as with the laser field.

The laser field

Typical radii of the cluster are of the order of 10 nm, which is much smaller than the $\lambda = 800$ nm wavelength of the laser used in the experiments. The laser can thus be described as a uniform time-dependent external electric

field:

$$\mathbf{F}_L(t) = \mathbf{F}_0 \sin^2 \left(\frac{\pi t}{2\sqrt{2}\tau} \right). \quad (2.2)$$

The pulse duration τ corresponds to the experimentally accessible full width at half maximum (FWHM) of the laser intensity envelope. For a laser pulse linearly polarized along the z-axis, this becomes:

$$\mathbf{F}_L(t) = F_0 \hat{\mathbf{z}} \sin(\omega t) \sin^2 \left(\frac{\pi t}{2\sqrt{2}\tau} \right), \quad (2.3)$$

with $\omega = 0.057$ a.u.. The peak laser field and the peak laser intensity are related in the following way:

$$I = \frac{c}{8\pi} F_0^2, \quad (2.4)$$

which translates into the following conversion formula:

$$F_0[\text{a.u.}] \approx 5.338 \cdot 10^{-9} \sqrt{I[\text{Wcm}^{-2}]}. \quad (2.5)$$

As soon as the laser field is strong enough to ionize the argon atoms, the cluster becomes conducting. In order to evaluate the resulting attenuation of the impinging electromagnetic wave, we compare the skin depth δ_{skin} to the cluster radius. The skin depth is linked to the laser frequency ω and the dielectric function $\epsilon(\omega)$ of the cluster:

$$\delta_{\text{skin}} = \frac{c}{\omega \Im \sqrt{\epsilon(\omega)}}, \quad (2.6)$$

where c is the speed of light and $\Im \sqrt{\epsilon(\omega)}$ stands for the imaginary part of $\sqrt{\epsilon(\omega)}$. By modeling the cluster as a polarizable sphere (see also section 6.1), the dielectric function can be expressed in terms of the bulk plasma frequency ω_P , the eigenfrequency of the sphere $\omega_0 = \omega_P/\sqrt{3}$ and the damping constant γ (controlled by the collision rate):

$$\epsilon(\omega) = 1 + \frac{\omega_P^2}{\omega_0^2 - \omega^2 - i\omega\gamma}. \quad (2.7)$$

The treatment as a polarizable sphere is no longer appropriate if the cluster is of the order of, or larger than the wavelength of the laser. The eigenfrequency ω_0 of the cluster, and thus its optical properties, depend then on the cluster radius R_{cl} [Kolwas, 1996]. In our case, however, we always have $R_{cl} \ll \lambda$ and we can use $\omega_0 = \omega_P/\sqrt{3}$. The plasma frequency is determined by the electronic density $\omega_P = \sqrt{4\pi n^{(e)}}$. With typical values of $\omega_P \sim 0.1$ to 0.7 a.u. and $\gamma \sim 0.01$ to 1 , the skin depth is found to be of the order $\delta_{\text{skin}} \sim 10^3$ to 10^4 a.u., which is considerably larger than the cluster radii R_{cl} we study. We therefore neglect the wave attenuation across the cluster in all our simulations.

The mean field

Electron-electron, ion-ion and electron-ion interactions are taken into account by the time-dependent mean field $\mathbf{F}_{\text{mean}}(\mathbf{r}, t)$, which depends on the positions of all test particles and will be discussed in further detail in chapter 3. In a nutshell, the mean field is computed on a two-dimensional cylindrical grid by solving the Poisson equation for the charge distribution evaluated from the test particle positions.

The stochastic forces

The changes in momentum of the electrons participating in a collision event are included formally in the equations of motion (2.1) as the stochastic forces $\mathbf{K}_{\text{stoc}}(\mathbf{r}_k^{(e)}, \dot{\mathbf{r}}_k^{(e)}, t)$. Inelastic processes (e.g. electron-impact ionization) can additionally be accompanied by a change in the number of particles $N_e(t)$. All collision processes are treated as stochastic events controlled by their probability to occur during the time step Δt , which takes typically the form

$$P = \sigma n_{\text{target}} \dot{r}_k \Delta t \quad (2.8)$$

σ stands for the cross-section of the considered process, n_{target} is the collision partner density, and $\dot{r}_k \Delta t$ the distance traveled during the time interval by the particle under consideration. By drawing a random number $x \in [0; 1]$ one decides whether an event takes place by checking if $x < P$. When considering the stochastic particle-particle interactions (elastic or inelastic) of a given particle, we pair it at each time step with a partner particle chosen randomly from its spatial surroundings (see appendix B). While it is possible to evaluate the probabilities (2.8) using averaged values, such as the mean ionic charge state or the mean electron energy, picking a random partner from the test particle ensemble allows for a better sampling of the distribution functions relevant for the considered process. All stochastic processes considered in our model are discussed in chapters 4 and 5.

Chapter 3

Evaluation of the mean-field

The mean field $\mathbf{F}_{\text{mean}}(\mathbf{r}, t)$ accounts for the electrostatic interactions between the particles and is treated by a particle-mesh (PM) approach [Hockney and Eastwood, 1988]: at each time step the particles are assigned to mesh cells and a discrete charge distribution is determined. The Poisson equation is then solved on the mesh, and the force acting on a particle is determined according to the particle's position in the mesh. The introduction of the mesh is necessary as the straight-forward approach of evaluating all particle-particle forces explicitly is infeasible for the large number of simulated particles ($N \gg 10000$) necessary for describing the dynamics of large clusters. The gain in speed by the PM-approach is obtained at the cost of a reduced resolution: within a mesh cell, the forces between the particles are not resolved. This can be remedied in part by the inclusion of stochastic forces $\mathbf{K}_{\text{stoc}}(\mathbf{r}_k^{(e)}, \dot{\mathbf{r}}_k^{(e)}, t)$ that incorporate the effect of close encounters (i. e. collisions) between the particles.

3.1 Space discretization

We divide the simulation volume in an effective 2D mesh that takes advantage of the rotational symmetry around the laser polarization axis. This reduction from 3D to 2D entails better statistics (i. e. more particles per mesh cell) and a faster solution of the Poisson equation. We introduce axisymmetrical cylindrical coordinates (R, z) :

$$\begin{aligned} R &= \sqrt{x^2 + y^2} \\ z &= z \end{aligned} \tag{3.1}$$

The entire simulation volume is discretized in 257×513 cells in (R, z) . The grid spacing is determined by the number of cells on one cluster radius R_{cl} in

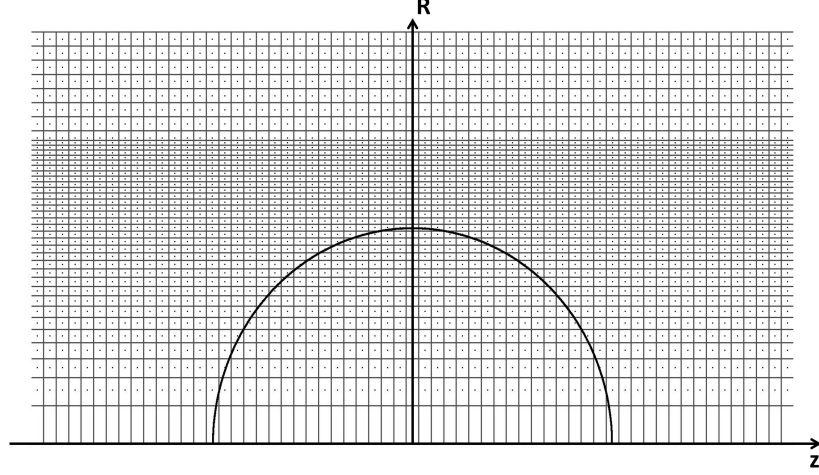


Figure 3.1: The discretization of the simulation volume makes use of the rotational symmetry around the laser polarization axis z . Each cell corresponds to a cylindrical shell. The black line represents the initial cluster radius R_{cl} ($N_R = N_z = 16$). The dots mark the cell centers (R_i, z_j) . For $i > 2N_R$ the step size in R direction is constant.

R -direction N_R and in z -direction N_z . In z -direction the centers of the cells (R_i, z_j) are equally spaced with step-size Δz :

$$\begin{aligned} z_j &= j\Delta z \quad j = -256, \dots, 256 \\ \Delta z &= \frac{R_{cl}}{N_z}. \end{aligned} \quad (3.2)$$

In radial direction, the cell centers are placed so as to obtain cells of equal volume up to R_{2N_R} . In order to increase the spatial resolution close to the laser axis, we chose a smaller step in R -direction for the cells closest to the z -axis (R_0, z_j) . These cells then have only half the volume of the neighboring cells. To include more space in the simulation volume, the step size in R -direction is constant from $i = 2N_R + 1$ to $i = 256$ and chosen so as to achieve $R_{256} = z_{256}$:

$$\begin{aligned} R_i &= R_{cl} \sqrt{\frac{i}{N_R}} & i = 0 \dots 2N_R \\ R_i &= R_{2N_R} + \frac{256\Delta z - R_{2N_R}}{256 - 2N_R} (i - 2N_R) & i = 2N_R + 1 \dots 256 \end{aligned} \quad (3.3)$$

The discrete charge distribution $\rho_{i,j}$ is evaluated at each time step by assigning every test particle to a cell of the discretization grid. The cell indices (i, j) corresponding to a particle at (R, z) are determined according to equations (3.2) and (3.3). In order to reduce artificial fluctuations in the charge distribution when a particle moves from one cell to the next, we make use of the Cloud-In-Cell (CIC) method [Hockney and Eastwood, 1988] where the particle is not treated as a point particle, but as a homogeneous charge distribution over a given volume (see appendix C.1).

3.2 Solving the Poisson equation

Once the charge distribution ρ is known, the Poisson equation has to be solved to obtain the electrostatic potential ϕ . In axisymmetrical cylindrical coordinates (R, z) , the equation has the following form:

$$\frac{\partial^2 \phi(R, z)}{\partial R^2} + \frac{1}{R} \frac{\partial \phi(R, z)}{\partial R} + \frac{\partial^2 \phi(R, z)}{\partial z^2} = -4\pi\rho(R, z) \quad (3.4)$$

The discretized Poisson equation for the discrete potential $\phi_{i,j} = \phi(R_i, z_j)$ can be written as:

$$a_i \phi_{i+1,j} + b_i \phi_{i-1,j} + \phi_{i,j+1} + \phi_{i,j-1} + (c_i - 2)\phi_{i,j} = d_{i,j} \quad (3.5)$$

with:

$$\begin{aligned} a_i &= \frac{\Delta z^2}{R_{i+1} - R_{i-1}} \left(\frac{2}{R_{i+1} - R_i} + \frac{1}{R_i} \right) \\ b_i &= \frac{\Delta z^2}{R_{i+1} - R_{i-1}} \left(\frac{2}{R_i - R_{i-1}} + \frac{1}{R_i} \right) \\ c_i &= -\frac{2\Delta z^2}{(R_{i+1} - R_i)(R_i - R_{i-1})} \\ d_{i,j} &= -4\pi\rho_{i,j}\Delta z^2. \end{aligned} \quad (3.6)$$

As the coefficients a , b and c are independent of the index j , eq. (3.5) can be rewritten as:

$$\phi_{(j-1)} + \mathbf{A}\phi_{(j)} + \phi_{(j+1)} = \mathbf{d}_{(j)}, \quad (3.7)$$

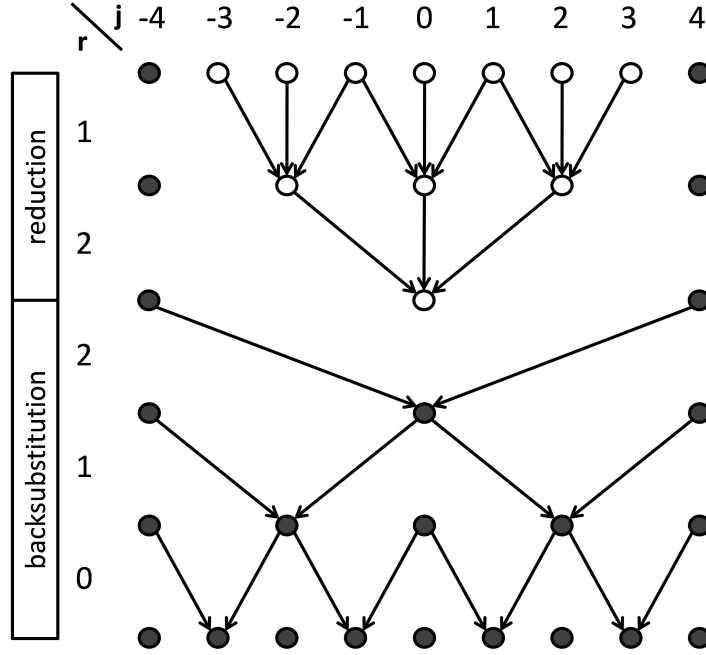


Figure 3.2: Schematic of the cyclic reduction procedure for $j = -4, \dots, 4$. Empty circles symbolize unknown, and filled circles known values of $\phi_{(j)}$. $\phi_{(-4)}$ and $\phi_{(4)}$ are given by the boundary conditions. In the case of 7 unknown lines, 2 reduction steps and 3 backsubstitution steps are needed to determine all $\phi_{(j)}$. The arrows indicate the points that contribute to a new value.

$\phi_{(-256)}$ and $\phi_{(256)}$ being fixed by the boundary conditions (3.12), the remaining system of 511 equations (3.7) can be solved by cyclic reduction [Cohen, 1994; Hockney and Eastwood, 1988]. The general idea behind the cyclic reduction procedure is illustrated for a small system of 7 equations in fig. 3.2 and will be discussed in detail for our 511 equations in appendix C.2. By taking three consecutive equations of the system (3.7):

$$\begin{aligned}
 \phi_{(j-2)} + \mathbf{A}\phi_{(j-1)} + \phi_{(j)} &= \mathbf{d}_{(j-1)} \\
 \phi_{(j-1)} + \mathbf{A}\phi_{(j)} + \phi_{(j+1)} &= \mathbf{d}_{(j)} \\
 \phi_{(j)} + \mathbf{A}\phi_{(j+1)} + \phi_{(j+2)} &= \mathbf{d}_{(j+1)},
 \end{aligned} \tag{3.14}$$

multiplying the second equation by $-\mathbf{A}$ and adding all three, one performs one level of cyclic reduction and reduces the total number of equations by a factor of 2:

$$\phi_{(j-2)} + \mathbf{A}^{(1)}\phi_{(j)} + \phi_{(j+2)} = \mathbf{d}_{(j)}^{(1)} \tag{3.15}$$

with (\mathbf{E} stands for the identity matrix):

$$\begin{aligned}\mathbf{A}^{(1)} &= 2\mathbf{E} - \mathbf{A}^2 \\ \mathbf{d}_{(j)}^{(1)} &= \mathbf{d}_{(j-1)} - \mathbf{A}\mathbf{d}_{(j)} + \mathbf{d}_{(j+1)}.\end{aligned}$$

This procedure can be iterated and after $r = 8$ reductions the 511 initial equations of (3.7) are reduced to only one equation:

$$\mathbf{A}^{(8)}\phi_{(0)} = \mathbf{d}_{(0)}^{(8)} - \phi_{(-256)} - \phi_{(256)} \quad (3.16)$$

where $\mathbf{A}^{(8)}$ is a known function of \mathbf{A} , $\mathbf{d}_{(0)}^{(8)}$ of \mathbf{A} and $\mathbf{d}_{(j)}$, and $\phi_{(-256)}$ and $\phi_{(256)}$ are determined by the boundary conditions (3.12). One can therefore solve (3.16) for the central line $\phi_{(0)} = \phi_{i,0}$. Once $\phi_{(0)}$ is known, the 2 equations of the 7th reduction cycle allow to determine $\phi_{(128)}$ and $\phi_{(-128)}$. By consecutive backsubstitution from $r = 8$ to $r = 0$ one finally obtains all values $\phi_{i,j}$ (see appendix C.2).

The mean field $\mathbf{F}_{\text{mean}}(R_i, z_j)$ is obtained by taking the gradient of the potential $\phi_{i,j}$:

$$\begin{aligned}F_R^{\text{mean}}(R_i, z_j) &= -\frac{\phi_{i+1,j} - \phi_{i-1,j}}{R_{i+1} - R_{i-1}} \\ F_z^{\text{mean}}(R_i, z_j) &= -\frac{\phi_{i,j+1} - \phi_{i,j-1}}{2\Delta z}.\end{aligned} \quad (3.17)$$

The mean field contribution to the force acting on a given particle k located at (R, z) is obtained by interpolating the discrete mean field using the same algorithm as for charge assignment (appendix C.1).

Chapter 4

Elastic scattering processes

An important contribution to the stochastic forces \mathbf{K}_{stoc} acting on a test particle are momentum changes due to elastic scattering processes. Due to the huge mass difference between the collision partners, elastic electron-ion scattering involves essentially only a change in the direction of the momentum of one electron, as the momentum transfer to the ion can be neglected. Scattering of two electrons on the other hand, call for the change of two momenta so as to preserve the total kinetic energy of the two particles.

4.1 Elastic electron-ion scattering

We obtain realistic differential cross sections $d\sigma_{e-i}(\theta, E)/d\theta$ for scattering of electrons at argon ions by performing a partial-wave analysis [Salvat and Mayol, 1993] using parametrized Hartree-Fock potentials [Szydlik and Green, 1974]. The data is pre-calculated for a wide range of electron energies and all relevant ionic charge states of argon $q = 1, \dots, 16$ assuming the ionic ground state, and serves as input. The usage of these realistic potentials ensures a proper description of large-angle scattering ($\theta \gtrsim 90^\circ$), which is determined by the non-Coulombic short-ranged potentials of the ionic cores. $d\sigma_{e-i}/d\theta$ is typically dominated by few low-order partial waves giving rise to generalized Ramsauer-Townsend minima [Mott and Massey, 1965] and diffraction oscillations [Burgdörfer et al., 1995] (fig. 4.1). We assume for simplicity the electronic ground state occupation for each q and neglect core-excited configurations. For the interstitial region a muffin-tin potential is employed in order to account for solid-state effects [Salvat and Mayol, 1993]. The potential shape in this region has, however, no significant influence on the cross sections at backward angles. The latter exceeds the pure Coulomb case by several orders of magnitude for all charge states and over a wide

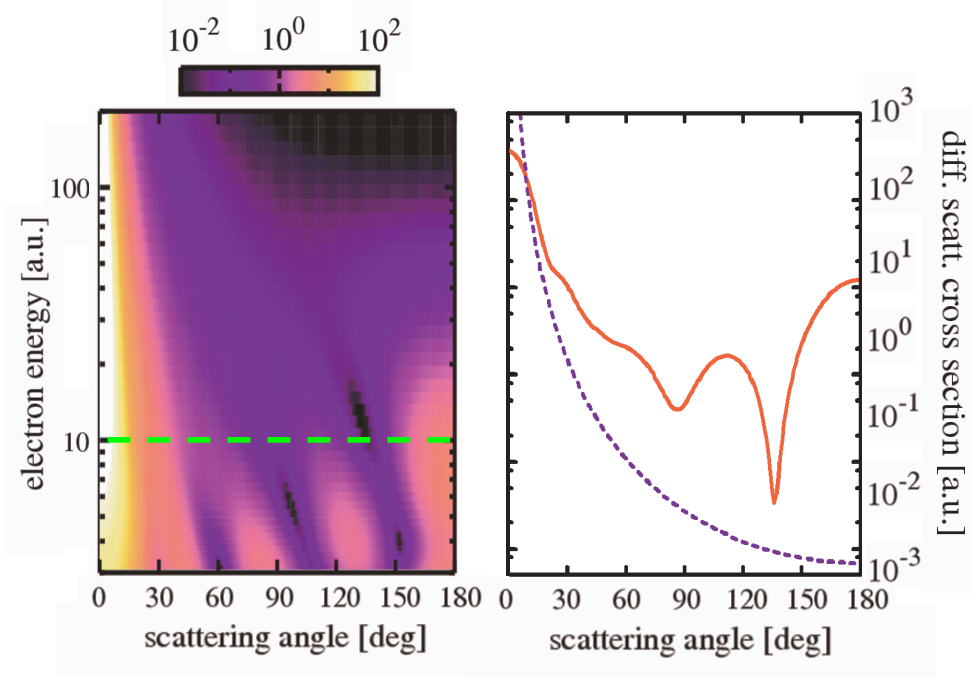


Figure 4.1: Left: Differential cross-section distribution $d\sigma_{e-i}(\theta, E)/d\theta$ in a.u. for elastic electron scattering at Ar^{2+} ions. The cross section was calculated by partial-wave analysis for a parameterized Hartree-Fock potential [Salvat and Mayol, 1993; Szydlik and Green, 1974]. Right: $d\sigma_{e-i}(\theta)/d\theta$ for an electron with fixed kinetic energy $E = 10$ a.u. (solid line). For comparison, the Rutherford cross-section $\left(\frac{q}{4E}\right)^2 \frac{1}{\sin^4(\theta/2)}$ is also displayed (dashed line).

range of electron energies (fig. 4.1).

Whether an elastic electron-ion scattering takes place for a given electron k with kinetic energy E_k is decided at each time step by pairing it up randomly with an ion j from the same chaining cell and comparing a random number to the scattering probability:

$$P_{e-i} = \sigma_{e-i}(q_j, E_k) n^{(i)}(\mathbf{r}_k^{(e)}) v_k^{(e)} \Delta t. \quad (4.1)$$

In case of a scattering event, the scattering angle θ_{scatt} is determined by another random number and the differential cross-section $d\sigma_{e-i}(\theta, E_k, q_j)/d\theta$ (see Salvat and Mayol [1993]). The azimuthal scattering angle ϕ_{scatt} is chosen randomly from the interval $[0, 2\pi]$. The velocity vector of the electron is then rotated according to these two scattering angles. For an original velocity $\mathbf{v}_k^{(e)}$

(in cartesian coordinates):

$$\mathbf{v}_k^{(e)} = v \begin{pmatrix} \cos \phi \sin \theta \\ \sin \phi \sin \theta \\ \cos \theta \end{pmatrix} \quad (4.2)$$

the velocity $\mathbf{v}'_k^{(e)}$ after scattering is given as (see [Deiss, 2005]):

$$\mathbf{v}'_k^{(e)} = v \begin{pmatrix} \sin \phi & \cos \theta \cos \phi & \cos \phi \sin \theta \\ -\cos \phi & \sin \phi \cos \theta & \sin \theta \sin \phi \\ 0 & -\sin \theta & \cos \theta \end{pmatrix} \begin{pmatrix} \cos \phi_{scatt} \sin \theta_{scatt} \\ \sin \phi_{scatt} \sin \theta_{scatt} \\ \cos \theta_{scatt} \end{pmatrix} \quad (4.3)$$

4.2 Electron-electron scattering

Electron-electron scattering is treated following the model proposed in Nanbu [1997]. K. Nanbu performed numerical simulations for a particle undergoing a succession of N_{coll} small-angle Coulomb collisions in a plasma during the time interval Δt . From the results he extracted analytical estimates for the distribution function of the cumulative angle θ_{ee} by which the particle has been deflected during Δt . The succession of small-angle binary collisions can therefore be approximated by a single collision with a large scattering angle θ_{ee} . Apart from the requirement that the plasma properties should not change during Δt , no restrictions apply to the choice of the time step. This constitutes the advantage of this approach compared to the more straightforward binary collision model [Takizuka and Abe, 1977]. In that model each small-angle scattering event is calculated one-by-one, and the time step has to be chosen much smaller than the relaxation time.

We start out by forming random electron pairs (k, k') within each cell of the chaining mesh. The relative velocity of two paired electrons is denoted by $\mathbf{u}_{kk'} = \mathbf{v}_k^{(e)} - \mathbf{v}_{k'}^{(e)}$. As shown by Nanbu [1997], the expectation value of $\sin^2 \frac{\theta_{ee}}{2}$ can be well approximated by:

$$\left\langle \sin^2 \frac{\theta_{ee}}{2} \right\rangle = \frac{1 - e^{-s}}{2}, \quad (4.4)$$

where the isotropy parameter s is determined by the expectation value of the single-scattering angles $\chi_1 \ll 1$ and the number of small-angle collisions N_{coll} that took place during the time-step Δt :

$$s = \frac{\langle \chi_1^2 \rangle N_{\text{coll}}}{2}. \quad (4.5)$$

For small values of the isotropy parameter s the test particles are hardly deviated from their original directions, whereas for large s the scattering becomes isotropic. This should also be reflected in the distribution function $f(\theta_{ee})$, which is approximated based on simulation data as:

$$f(\theta_{ee}) = \frac{A}{4\pi \sinh A} \exp(A \cos \theta_{ee}). \quad (4.6)$$

By imposing the condition (4.4), one gets:

$$\coth A - A^{-1} = e^{-s} \quad (4.7)$$

The values $A(s)$ can be precalculated by the Newton method [Press et al., 1986] and serve as input for the simulation. Now that the distribution function $f(\theta_{ee})$ is known, the corresponding random sampling of $\cos \theta_{ee}$ can be determined to be:

$$\cos \theta_{ee} = \frac{1}{A} \ln (e^{-A} + 2x \sinh A), \quad (4.8)$$

where $0 < x < 1$ is a random number. For a small isotropy parameter s , A becomes very large and small angles θ_{ee} make the largest contribution to $f(\theta_{ee})$. In order to avoid an exponential overflow of $\sinh A$ due to the large A , (4.8) is modified for small s so as to mimic a Gaussian profile with a narrow width for $f(\theta_{ee})$. For large s on the other hand, the scattering can be seen as isotropic and (4.8) simplified accordingly. One finally gets:

$$\cos \theta_{ee} = \begin{cases} 1 + s \ln x & \text{for } s < 0.01 \\ \frac{1}{A} \ln (e^{-A} + 2x \sinh A) & \text{for } 0.01 < s < 6 \\ 2x - 1 & \text{for } s > 6 \end{cases} \quad (4.9)$$

The only unknown parameter in this set of equations is the isotropy parameter s , which we will now try to express by parameters accessible by the simulation. The maximal impact parameter b_{\max} determines the number N_{coll} of small-angle collisions [Nanbu, 1997]:

$$N_{\text{coll}} = n^{(e)} \pi b_{\max}^2 u_{kk'} \Delta t. \quad (4.10)$$

In a plasma the impact parameter is limited by the screening of the particles and b_{\max} is set equal to the Debye length $\lambda_D = \sqrt{T/(4\pi n^{(e)})}$ [Mitcher, 1973]. For an arbitrary impact parameter b , the deflection angle χ_1 for a collision between two charged particles with charges q_1 and q_2 and reduced mass μ is [Mitcher, 1973]:

$$\tan \frac{\chi_1}{2} = \frac{|q_1 q_2|}{4\pi \epsilon_0 \mu u_{12}^2 b} = \frac{b_0}{2b}. \quad (4.11)$$

Taking into consideration the limitation of b by b_{\max} , and assuming small-angle scattering events, one gets:

$$\langle \chi_1^2 \rangle = 2 \left(\frac{b_0}{b_{\max}} \right)^2. \quad (4.12)$$

For an electron-electron collision, b_0 can be expressed in atomic units as:

$$b_0 = \frac{4}{u_{kk'}^2}. \quad (4.13)$$

Eq. (4.5) can thus be rewritten in terms of parameters accessible by the simulation:

$$s = 16\pi n^{(e)} u_{kk'}^{-3} \Delta t. \quad (4.14)$$

The procedure for performing electron-electron scattering can be summarized as follows:

- Within one chaining cell, build electron pairs (k, k') and evaluate their relative velocity $\mathbf{u}_{kk'}$ and their center of mass velocity $\mathbf{u}_M = (\mathbf{v}_k^{(e)} + \mathbf{v}_{k'}^{(e)})/2$.
- Determine the isotropy parameter s from (4.14).
- Determine A from the tabulated values of $A(s)$.
- Draw a random number x and evaluate the scattering angle θ_{ee} from (4.9).
- Perform the rotation of $\mathbf{u}_{kk'}$ by θ_{ee} and a random $\phi_{ee} \in [0; 2\pi]$ in analogy to (4.3).
- Evaluate the post-collision particle velocities: $\mathbf{v}'_k^{(e)} = \mathbf{u}_M + \mathbf{u}'_{kk'}/2$ and $\mathbf{v}'_{k'}^{(e)} = \mathbf{u}_M - \mathbf{u}'_{kk'}/2$.

Chapter 5

Ionization, excitation and recombination

High resolution X-ray spectroscopy gives experimental access to the atomic configurations of cluster ions with K-shell vacancies. In our particle simulation only the ions and the quasi-free electrons are treated explicitly. Nevertheless we follow in detail the occupation numbers $N_j^{(M)}(t)$, $N_j^{(L23)}(t)$, $N_j^{(L1)}(t)$ and $N_j^{(K)}(t)$ of the different atomic shells for all $j = 1, \dots, N_{\text{simul}}$ argon ions.

5.1 Modeling the argon ion

Only limited data is available for the binding energies E_M , E_{L23} , E_{L1} and E_K of the $(n = 3)$, $(n = 2, l = 1)$, $(n = 2, l = 0)$ and $(n = 1)$ states of argon ions with multiple vacancies in inner and outer shells [Larkins, 1971; Lotz, 1968b; Ralchenko et al., 2005]. We therefore estimate these energies by empirical formulas (5.1) obtained by extrapolating available data for certain ionic configurations (see figs. 5.1 to 5.3). For the outer shells, we neglect the dependence on the exact configuration of the K- and L-shell and retain only a dependence on the number of electrons $N^{(M)}$ in the M-shell and $N^{(L)} = N^{(L23)} + N^{(L1)}$ in the L-shell:

$$E_M(N^{(M)}, N^{(L)}) = 13.40 - 0.94N^{(L)} - 0.71N^{(M)} \quad (5.1a)$$

$$E_{L23}(N^{(M)}, N^{(L)}) = 33.24 - 2.24N^{(L)} - 0.79N^{(M)} \quad (5.1b)$$

$$E_{L1}(N^{(M)}, N^{(L)}) = 34.49 - 2.06N^{(L)} - 0.77N^{(M)} \quad (5.1c)$$

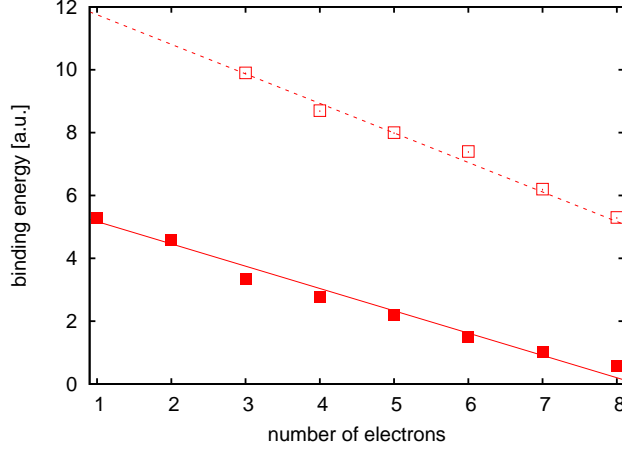


Figure 5.1: M-shell binding energies. Data for $E_M(N^{(M)}, N^{(L)} = 8)$ from Lotz [1968b] (■) and for $E_M(N^{(M)} = 1, N^{(L)})$ from Ralchenko et al. [2005] (□). Full line: eq. (5.1a) with $N^{(L)} = 8$, dashed line: eq. (5.1a) with $N^{(M)} = 1$.

The binding energy E_K of the K-shell electrons is taken to be only dependent on the charge state q of the ion:

$$E_K(q) = \begin{cases} 117.8 + 1.3q & \text{for } q \leq 8 \\ 108.6 + 2.44q & \text{for } 8 < q \leq 16. \end{cases} \quad (5.1d)$$

It has been proposed by Siedschlag and Rost [2003] that, in the case of a cluster ion, ionization may be enhanced by the proximity of the surrounding highly charged ions. The additional Coulomb potential of its neighbor lowers the Coulomb barrier of the considered ion j . We estimate the lowering of the ionization threshold due to the superposition of an adjacent screened Coulomb potential to be (see fig. 5.4):

$$\Delta W_j = -\frac{4q_j}{d_{ii}} \exp\left(-\frac{d_{ii}}{2\lambda_D}\right) \quad (5.2)$$

with $d_{ii} = (1/n^{(i)})^{1/3}$ the mean ion-ion distance and $\lambda_D = \sqrt{T/(4\pi n^{(e)})}$ the Debye screening length. In this approach we neglect any shift in energy of the bound state caused by the field of the surrounding ions.

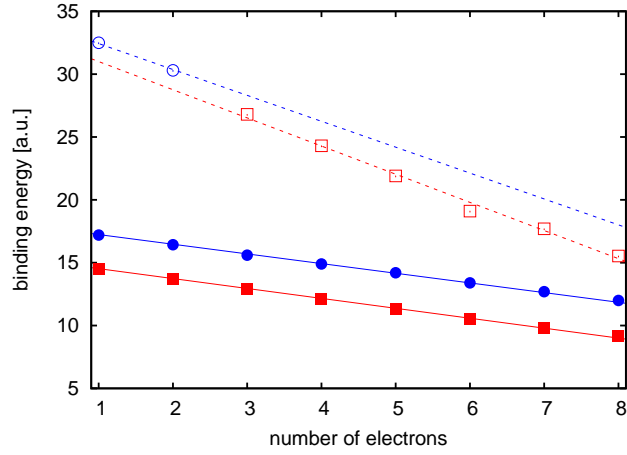


Figure 5.2: Binding energies of the L23-shell (red) and the L1-shell (blue). Data for $E_{L23}(N^{(M)}, N^{(L)} = 8)$ (■), $E_{L23}(N^{(M)} = 0, N^{(L)})$ (□), $E_{L1}(N^{(M)}, N^{(L)} = 8)$ (●) and $E_{L1}(N^{(M)} = 0, N^{(L)})$ (○) from Lotz [1968b]. Full lines: eq. (5.1b) and eq. (5.1c) with $N^{(L)} = 8$. Dashed lines: eq. (5.1b) and eq. (5.1c) with $N^{(M)} = 0$.

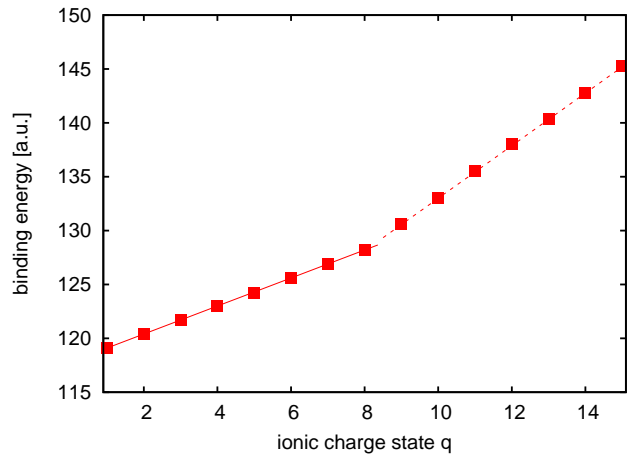


Figure 5.3: K-shell binding energy as a function of the ionic charge state. Literature data from [Lotz, 1968b] (■) and eq. (5.1d) (lines).

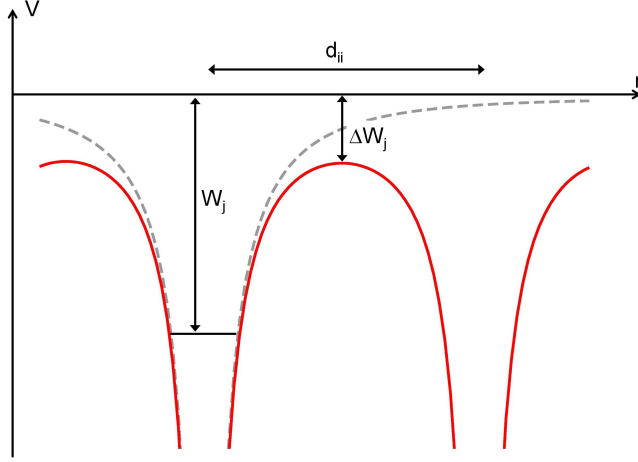


Figure 5.4: Lowering of the ionization threshold by the proximity of highly charged ions.

5.2 Field ionization

The local field $F(\mathbf{r}_j)$ at the position of ion j tilts the ionic potential and allows electrons to escape from the ion either by tunneling through the potential barrier or, if the field is strong enough, by over-barrier ionization (see fig. 5.5). The ionization energy W_j of the ion corresponds to the binding energy E_a of the outermost occupied shell a . In the case of an ionization event, an additional quasi-free electron is generated with zero initial velocity at the position of the ion, the charge state q_j of the ion is increased by one and the corresponding occupation number $N_j^{(a)}$ is reduced by one.

Over-barrier ionization takes place when the local field F at the position of the ion exceeds the threshold field [Bethe and Salpeter, 1975]:

$$F_{OBI} = \frac{W^2}{4(q+1)}. \quad (5.3)$$

If the local field is too weak for over-barrier ionization, tunnel ionization may take place. The probability for tunnel ionization per unit time from a state with ionization energy W and orbital quantum number l of an ion with charge q in a field F is taken from the ADK formula [Ammosov et al., 1986;

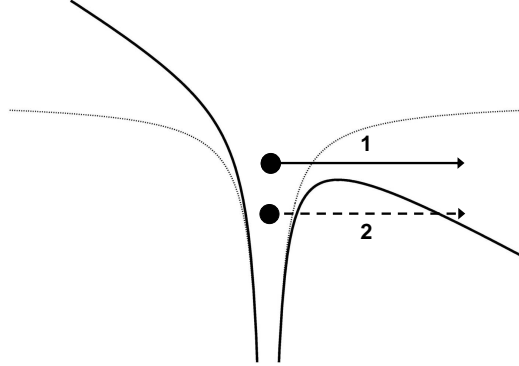


Figure 5.5: Ionic potential (dashed) and ionic potential tilted by electric field (solid). The two possible field ionization mechanisms are over-barrier ionization (1) and tunnel ionization (2).

Augst et al., 1991]:

$$\Gamma_{\text{tun}} = \sum_{m=-l}^l f(l, m) \left(\frac{6}{\pi}\right)^{1/2} \left(\frac{2e}{n^*}\right)^{2n^*} \frac{W}{2\pi n^*} \times \left(\frac{2(2W)^{3/2}}{F}\right)^{2n^* - |m| - 3/2} \exp\left(-\frac{2(2W)^{3/2}}{3F}\right) \quad (5.4)$$

with:

$$f(l, m) = \frac{(2l+1)(l+|m|)!}{2^{|m|}(|m|)!(l-|m|)!} \quad (5.5)$$

$e = 2.718\dots$ and the effective quantum number n^* :

$$n^* = \frac{q+1}{\sqrt{2W}}. \quad (5.6)$$

At every time step each ion is checked for the occurrence of tunnel ionization by drawing a random number and comparing it to $\Gamma_{\text{tun}}\Delta t$.

5.3 Electron-impact ionization

In addition to field ionization, ionization can occur by collision of an electron with an ion, provided that the energy transfer from the free electron to the bound electron is larger than its binding energy. At each time step every

electron k is paired up randomly with an ion j from the same chaining cell and the total cross section for electron-impact ionization is evaluated from the Lotz formula [Lotz, 1968a] by summing over all ionic (sub-)shells:

$$\begin{aligned}\sigma_{\text{imp}}(E_k) &= \sum_{a=K,L1,L23,M} \sigma_{\text{imp}}^{(a)}(E_k) \\ \sigma_{\text{imp}}^{(a)}(E_k) &= 2.17 N_j^{(a)} \frac{\ln(E_k/E_a)}{E_k E_a} \Theta(E_k - E_a),\end{aligned}\quad (5.7)$$

where E_k is the kinetic energy of the quasi-free electron, $E_a(N_j^{(M)}, N_j^{(L)})$ are the binding energies determined according to eqs. (5.1), and the step functions $\Theta(E_k - E_a)$ assure that the energy thresholds are exceeded.

In the event of an impact ionization, an additional quasi-free electron is placed with zero velocity at the position of the ion j , the energy E_k is reduced by the binding energy E_a and the occupation number $N_j^{(a)}$ is decreased by a unit. As a check several simulations have also been performed, where, after the collision, the remaining kinetic energy is split equally between the two outgoing electrons. No significant change of the results could be observed.

5.4 Electron-impact excitation

An accurate treatment of electron-impact excitation requires quantum mechanical data on all transitions considered. Due to the vast number of ionic states, the sparsity of spectroscopic data [Ralchenko et al., 2005] and the large number of parameters entering the empirical formulas [Sobel'man et al., 1995], we restrict ourselves to the qualitative implementation of collisional excitation. We consider only excitations involving states with $n = 1, 2, 3$ (K,L,M shells). Indeed, the dense plasma environment inside a cluster puts the existence of higher excited states with $n \geq 4$ in question. Experimental data on the collisional excitation of transitions between these low lying shells is not available for argon ions. Theoretical (and/or semi-empirical) approaches give consistent orders of magnitude for the considered cross-sections but may differ by factors 2-3 (see fig. 5.6).

The widely used empirical expression proposed by van Regemorter [1962] for the cross-section $\sigma_{\text{exc}}^{(a \rightarrow b)}(E_k)$ for the excitation of a bound electron from state a to state b by a fast free electron with kinetic energy E_k

$$\sigma_{\text{exc}}^{(a \rightarrow b)}(E_k) = \frac{2\pi^2}{\sqrt{3}} \frac{1}{E_k E_{ab}} f(a \rightarrow b) g(E_k, E_{ab}) \quad (5.8)$$

requires the knowledge of the transition energy E_{ab} , the oscillator strength $f(a \rightarrow b)$ of the considered transition, and of the Gaunt factor $g(E_k, E_{ab})$

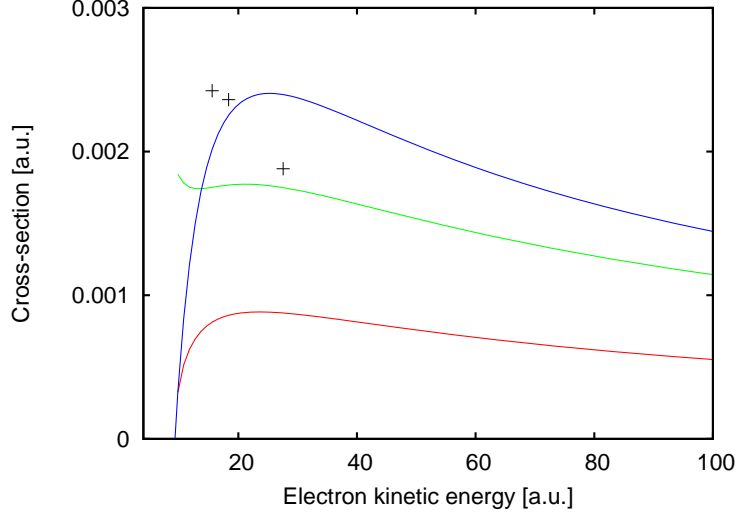


Figure 5.6: Cross-sections $\sigma_{eex}(E_k)$ for the electron-impact excitation of the transition $2p^6 \rightarrow 2p^5 3s$ in Ne-like Ar IX (Ar^{8+}) obtained with different theoretical approaches. Top to bottom: Bethe formula (5.9) (blue); values calculated by a QED approach in Ivanov et al. [1993] (crosses); van Regemorter formula (5.8) with Gaunt factor g taken from Mewe [1972] (green); empirical formula (6.1.7) in Sobel'man et al. [1995] (red). The energy of this transition is $E_{ab} = 9.3$ a.u. and the oscillator strength is $f(a \rightarrow b) = 0.18$ [Ralchenko et al., 2005].

which measures the probability for the incident electron to go from energy E_k to energy $E_k - E_{ab}$. This approach is only valid for optically allowed transitions ($\Delta l = 1$). Theoretical data on oscillator strengths for transitions in argon ions can be found in the CHIANTI database [Dere et al., 1997; Landi et al., 2006]. A typical value for $2s \rightarrow 3p$ and $2p \rightarrow 3s$ transitions appears to be $f_{L \rightarrow M} \sim 0.2$ and for $1s^2 \rightarrow 1s 2p$ transitions $f_{K \rightarrow L} \sim 0.7$. The energy dependent Gaunt factor g is obtained from experimental data or results of numerical calculations, and takes different functional forms, depending on the atomic configuration of the considered ion [Mewe, 1972]. For high electron energies $g = \sqrt{3}/(2\pi) \ln(E_k/E_{ab})$, so that eq. (5.8) takes the asymptotic form of the Bethe formula [Bethe, 1930; Mott and Massey, 1965]. As it is beyond the scope of our approach to include rigorously all excitation processes (which would require, additionally to the exact information on

energies and oscillator strengths for all considered atomic configurations, the influence of the plasma environment on these values), we restrict ourselves to an approximate implementation of collisional excitation using the asymptotic Bethe form of the cross-section for all electron energies and assuming typical oscillator strengths ($f_{L \rightarrow M} \sim 0.2$ and $f_{K \rightarrow L} \sim 0.7$):

$$\begin{aligned}\sigma_{eex}^{(L \rightarrow M)}(E_k) &= \pi f_{L \rightarrow M} \frac{\ln(E_k / (E_{L23} - E_M))}{E_k (E_{L23} - E_M)} \\ \sigma_{eex}^{(K \rightarrow L)}(E_k) &= \pi f_{K \rightarrow L} \frac{\ln(E_k / (E_K - E_{L23}))}{E_k (E_K - E_{L23})}.\end{aligned}\quad (5.9)$$

The transition is only allowed if there is at least one vacancy in the upper shell. In case an $L \rightarrow M$ excitation takes place, the incident electron's energy is reduced by $E_{L23} - E_M$, $N_j^{(L23)}$ is reduced by one, and $N_j^{(M)}$ is increased by one. $K \rightarrow L$ excitations are treated analogously.

5.5 Three-body recombination

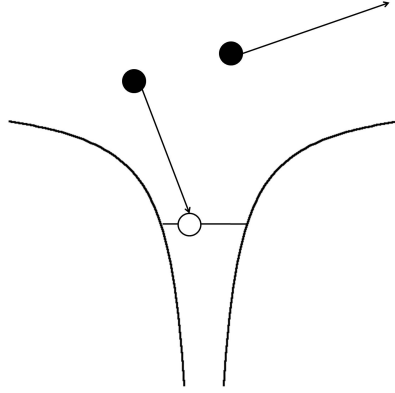


Figure 5.7: In a three-body recombination one free electrons recombines with an ion and the other free electron carries away the excess energy.

In three-body recombination the energy freed by the recombination of a free electron is carried away by a second free electron (fig. 5.7). As three particles are involved in the process, the probability for this event to occur for a given triplet (k_1, k_2, j) of two free electrons and an ion takes the following form:

$$P_{3br} = \sigma_{3br}(E_{k_1}, E_{k_2}) n^{(i)} n^{(e)} v_{k_1} v_{k_2} \Delta t, \quad (5.10)$$

where σ_{3br} is the generalized cross-section for three-body recombination (with a dimension of [area]⁴[time]).

Three-body recombination is the inverse process of electron-impact ionization. According to the principle of detailed balance [Mitcher, 1973], the rate for a microscopic process and its reverse process are equal in thermodynamical equilibrium. The cross-section σ_{3br} can thus be expressed in terms of the known cross-section for electron-impact ionization σ_{imp} . Under the assumption that σ_{3br} is only dependent on the sum of the energy of the incident electrons $\varepsilon = E_{k_1} + E_{k_2}$, the following relation has been derived by Hansen and Shlyaptseva [2004]:

$$\sigma_{3br}(\varepsilon) = 3\pi^2 \frac{g_{q-1}}{g_q} \frac{\varepsilon + E_a(N_j^{(a)})}{\varepsilon^3} \sigma_{\text{imp}} \left(\varepsilon + E_a(N_j^{(a)} + 1) \right), \quad (5.11)$$

where $E_a(N_j^{(a)})$ and $E_a(N_j^{(a)} + 1)$ stand for the binding energy of the considered shell before and after recombination. The statistical weights g_q and g_{q-1} of the ion state before and after recombination are determined by the degeneracy of the state and therefore by the occupation number: if, for example, the electron recombined to the L23-shell of ion j that was occupied by $N_j^{(L23)}$ electrons before the recombination $g_{q-1}/g_q = (6 - N_j^{(L23)})/(N_j^{(L23)} + 1)$. As (5.11) depends only on atomic parameters, it is applicable also if the plasma is not in a thermodynamical equilibrium. The main limitation of this approach is the neglect of plasma effects such as Debye shielding of the ions, which are not included in the impact ionization cross-sections.

5.6 Auger decay

We also include the possible decay of L-shell vacancies via an L-MM Auger process: the L-vacancy is filled by an M-shell electron and the excess energy is taken away by a second M-shell electron that gets ionized. The basic conditions $N_j^{(L)} < 8$, $N_j^{(M)} \geq 2$ and $2E_M \leq E_L$ have to be fulfilled for an ion to be eligible for an Auger event. The Auger rate Γ_A is known to be dependent on the number of spectator electrons in the M-shell [Chen and Crasemann, 1974]. In our simulation we use a quadratic fit of this dependence (see fig. 5.8):

$$\Gamma_A(N^{(M)}) = [0.0812(N^{(M)})^2 + 0.1768N^{(M)} - 0.631] \cdot 10^{-3} \text{ a.u.} \quad (5.12)$$

The probability for an Auger event to occur in ion j is then taken to be

$$P_A = \Delta t \left(8 - N_j^{(L)} \right) \Gamma_A(N_j^{(M)}). \quad (5.13)$$

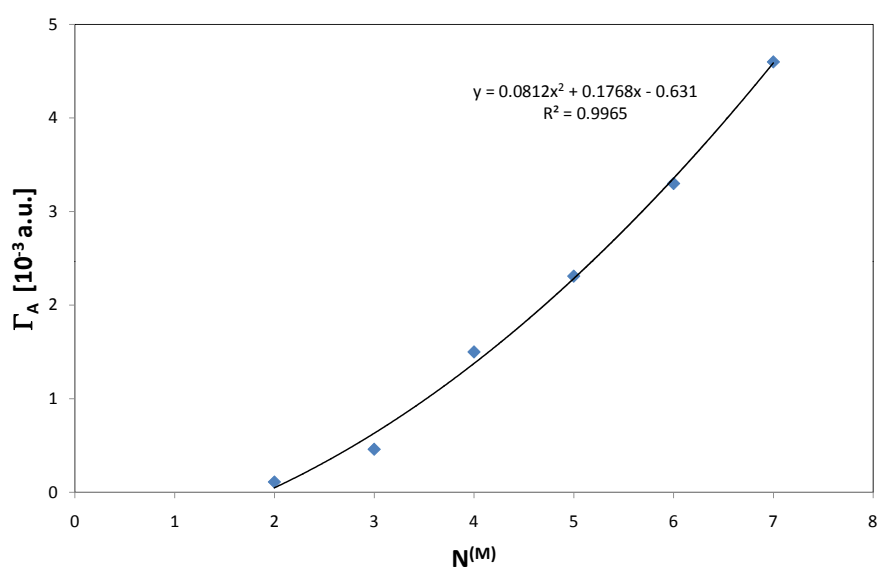


Figure 5.8: Average L-MM Auger rate for a $2p$ vacancy as a function of the number of M-shell electrons $N^{(M)}$. Theoretical calculations in Chen and Crasemann [1974] (points) and fitting formula (5.12).

Part II

Single cluster results

After discussing the details of the numerical model, we will now apply it to discuss the different aspects of the dynamics of a single cluster irradiated by a laser pulse. A special focus will be put on the dynamics of fast electrons and the production of inner-shell vacancies, which are at the origin of X-ray radiation. In a simple picture, the dynamics can be summarized as follows (fig. II.1): the atoms in the cluster are first ionized by the incident laser pulse (inner ionization) and the quasi-free electrons and ions form a cold “nanoplasma” of solid density within the initial boundaries of the cluster. Due to their vastly different mass, the dynamics of the ions and the electrons take place on different time-scales: the electrons are driven by both the laser field and the fields of the surrounding particles and move on the femtosecond time-scale of the laser period. The ions, on the other hand, are insensitive to the oscillations at the typical laser frequencies, reacting solely to the build-up of a DC-component in the field, and evolve on the time-scale of the laser pulse (100 fs to picoseconds). This leads to a stage in the beginning of the interaction, where the quasi-free electrons perform a driven collective oscillation relative to the static ionic background (fig. II.1a). Electron-impact ionization of the cluster ions produces additional quasi-free electrons, as well as inner-shell vacancies. As a fraction of the electrons leaves the cluster (outer ionization, fig. II.1b), a net charge is left behind, ion movement sets in and the cluster begins to expand (fig. II.1c) before disintegrating completely in a Coulomb explosion (fig. II.1d). The timing of the cluster explosion relative to the laser pulse is determined by both the characteristics of the cluster (size) and the laser pulse (pulse duration, laser intensity).

With the aim to disentangle the ionic and the electronic dynamics, we first present in chapters 6-8 results for systems where there is only little movement of the cluster ions during the interaction. This is true for large clusters ($N \gtrsim 10^5$ atoms) irradiated by short ($\tau \lesssim 80$ fs) laser pulses of moderate intensities ($I \lesssim 10^{16}$ Wcm $^{-2}$). As a typical example, we pick out the case of an argon cluster with $N = 2.8 \cdot 10^5$ atoms interacting with an infrared ($\lambda = 800$ nm) pulse of $I = 4.3 \cdot 10^{15}$ Wcm $^{-2}$ and $\tau = 61$ fs. The temporal and spatial characteristics of the mean field in and around the cluster will be studied in chapter 6. The relative importance of the different ionization mechanisms will be investigated in chapter 7. Chapter 8 will focus on the evolution of the electron kinetic energy distributions during the interaction and investigate in more detail the dynamics of the fast electrons. In chapter 9 we will eventually turn to longer pulses and/or smaller clusters in order to study the ionic dynamics during the cluster expansion and their influence on the electronic dynamics.

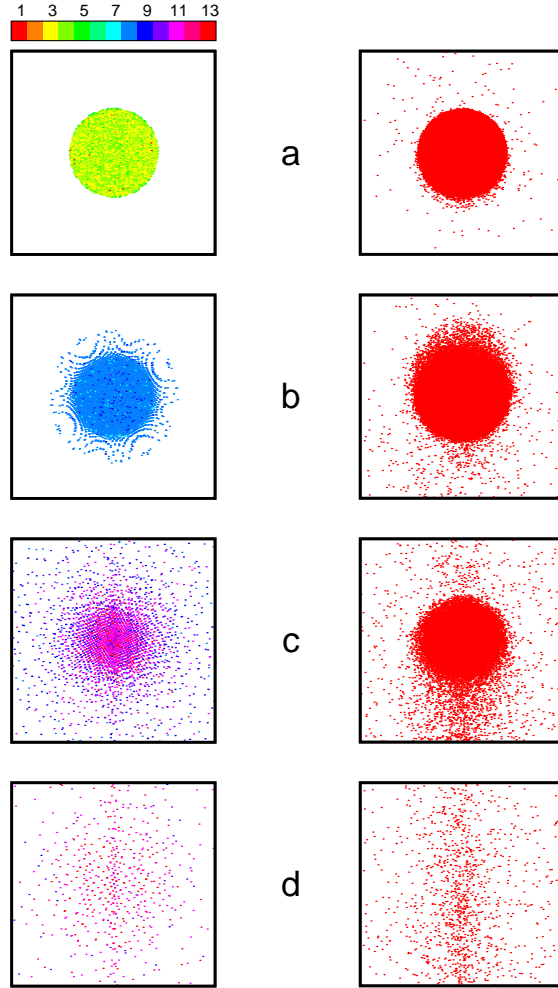


Figure II.1: Dynamics of a cluster with $N = 3.7 \cdot 10^4$ argon atoms (initial radius $R_0 = 136$ a.u.) irradiated by an infrared ($\lambda = 800$ nm) laser pulse of duration $\tau = 140$ fs and peak intensity $I = 2 \cdot 10^{16}$ Wcm $^{-2}$. The positions of ions (left) and electrons (right) in the $x - z$ plane are depicted. In the left panels, the color of the dots represents the ionic charge-state. The snapshots are taken of particles with $|y| < 15$ a.u. at $t = 51$ fs (a), 95 fs (b), 180 fs (c) and 225 fs (d).

Chapter 6

Charge distribution and mean field

6.1 Cluster polarization

The electronic dynamics start as soon as the laser field reaches the threshold for over-barrier ionization of neutral argon. The ionized electrons immediately react to both the laser field and the fields of the surrounding particles, while the ions are insensitive to the oscillating field and remain immobile. At this stage the cluster is essentially quasi-neutral, the electronic and the ionic charge compensating each other in nearly the entire cluster. The only charge imbalance can be observed at the cluster poles: the small periodic displacement of the electron cloud along the laser polarization axis results in a thin region of bare ionic charge at one cluster pole, and of excess electronic charge at the opposite pole (fig. 6.1). The situation at the poles is reversed every half laser cycle. At this stage, the cluster has a strong similarity with a polarizable sphere (fig. 6.2), the dynamical properties of which can be described analytically and can provide insight into the cluster behavior which is still helpful at later stages of the interaction. A displacement of a uniformly charged negative sphere (electrons) against a sphere of equal uniform positive charge (ions) induces a dipole moment \mathbf{p} . If the displacement is small compared to the sphere's radius, the produced electric field is given by [Purcell, 1985]:

$$\mathbf{F}_{\text{sph}}(\mathbf{r}) = \begin{cases} -\frac{\mathbf{p}}{R_{cl}^3} & \text{for } r < R_{cl} \\ -\frac{\mathbf{p}}{r^3} + 3\frac{\mathbf{p}\mathbf{r}}{r^5} & \text{for } r > R_{cl} \end{cases} \quad (6.1)$$

Inside the cluster, the field is uniform and oriented in the opposite direction of the dipole moment, whereas outside the cluster the field is that of a

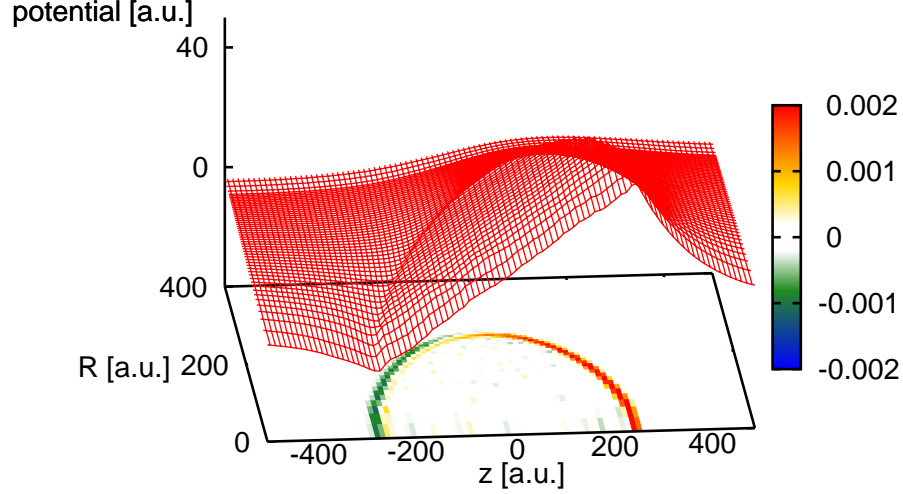


Figure 6.1: Snapshot of the charge density $\rho(R, z)$ (color coding in a.u.) and the corresponding electrostatic potential $\phi(R, z)$ (line plot) at $t = 33$ fs. ($N = 2.8 \cdot 10^5$, $\tau = 61$ fs, $I = 4.3 \cdot 10^{15}$ Wcm $^{-2}$)

central dipole \mathbf{p} . This results in a discontinuity and even a change of sign in the electric field at the cluster surface (see fig. 6.2). These characteristics of the field conform with the electrostatic potential resulting from the charge densities observed in the simulation (fig. 6.1). As the spherically distributed ions are considered immobile, the dipole moment is determined by the position of the electrons $\mathbf{p}(t) = -\sum_{k=1}^{N_e} \mathbf{r}_k^{(e)}(t)$. In a continuous-wave laser field with driving frequency ω , the dipole moment therefore obeys the following equation of motion:

$$\ddot{\mathbf{p}}(t) - \gamma \dot{\mathbf{p}}(t) + \frac{N_e}{R_{cl}^3} \mathbf{p}(t) = N_e \mathbf{F}_0 e^{i\omega t}, \quad (6.2)$$

where γ stands for the damping coefficient determined by the electron scattering events. The total effective field inside the cluster $\mathbf{F}_{\text{eff}} = \mathbf{F}_L + \mathbf{F}_{\text{sph}}$

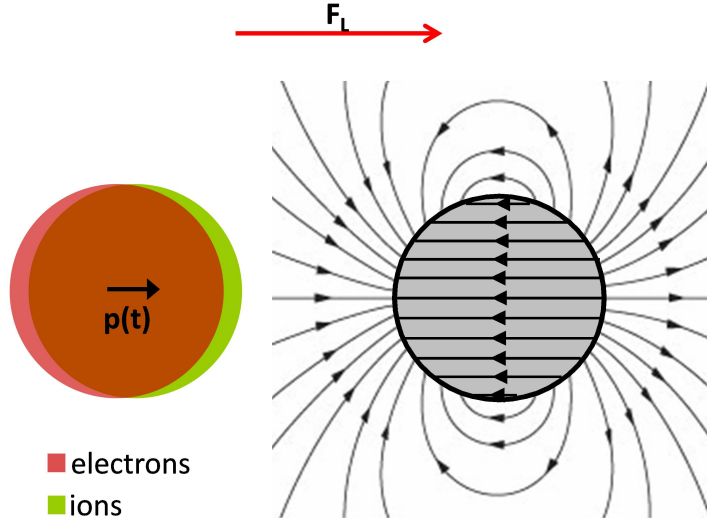


Figure 6.2: Polarized sphere: the displacement of the electrons with respect to the ions induces a dipole moment (left). The electric field of the polarized sphere screens the driving laser field inside the cluster and enhances it the cluster (right).

thus becomes:

$$\mathbf{F}_{\text{eff}} = \mathbf{F}_0 \left(1 - \frac{\omega_P^2/3}{\omega_P^2/3 - \omega^2 + i\gamma\omega} \right) e^{i\omega t} \quad \text{for } r < R_{cl}, \quad (6.3)$$

with the electronic plasma frequency $\omega_P = \sqrt{4\pi n^{(e)}}$. As the electronic density exceeds the solid density of argon one has $\omega_P^2 > 4\pi n_{\text{Ar}} \simeq 15\omega^2$, and the polarization of the cluster results in a screening of the laser field inside the cluster. However, at the cluster poles ($\mathbf{r} = (0, 0, \pm R_{cl})$) the laser field is enhanced due to the displacement of the electron cloud. By inserting the solution of (6.2) in (6.1) one gets:

$$\mathbf{F}_{\text{eff}} = \mathbf{F}_0 \left(1 + \frac{2\omega_P^2/3}{\omega_P^2/3 - \omega^2 + i\gamma\omega} \right) e^{i\omega t} \quad \text{at poles.} \quad (6.4)$$

Figure 6.3 displays the simulation result for the total electric field inside the cluster during the laser pulse. The screening of the laser field inside the cluster due to polarization is indeed very effective, reducing the laser field by a factor 5-7. The enhancement of the local electric field between $t = 90$ fs and $t = 120$ fs is due to wake fields from transiting electrons and will be discussed in detail in section 8.3.

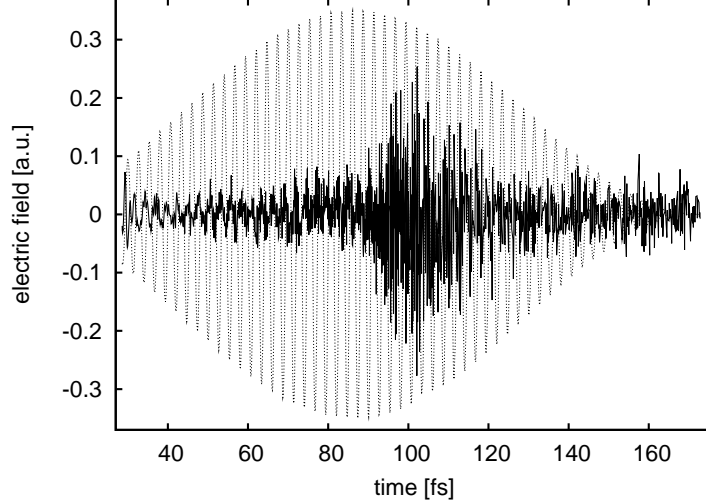


Figure 6.3: Local electric field (z-component) in the interior of the cluster at ($R = 0, z = 10.7$ a.u.). The laser field is also plotted (dotted gray line). Between $t \approx 90$ fs and $t \approx 120$ fs wake fields can be observed as discussed in section 8.3. ($N = 2.8 \cdot 10^5$, $\tau = 61$ fs, $I = 4.3 \cdot 10^{15}$ Wcm $^{-2}$)

As discussed in the introduction to this thesis, equating the ponderomotive energy U_P of the free laser field with the binding energy of the K-shell E_K fails to predict a correct laser intensity threshold for X-ray production. That the effective field inside and in vicinity of the cluster is very different from the free laser field, further underlines the inadequacy of U_P for estimating electron energies. Indeed, the energy electrons gain by oscillating in the screened field inside the cluster, must be significantly lower than U_P . At the cluster poles, however, the enhanced laser field could allow for an energy gain beyond U_P . These aspects of the electron acceleration will be discussed in detail in chapter 8.

One can further note that, within the model of the polarized sphere, there is the possibility of a resonance when $\sqrt{3}\omega = \omega_P$. This corresponds to the “nanoplasma resonance” often called upon to explain heating phenomena during laser plasma interaction [Ditmire et al., 1996]. For it to occur, the initially large electronic density has to drop during the laser pulse to the critical density $n_{cr}^{(e)} = 3\omega^2/(4\pi)$, for which the plasma frequency equals the laser frequency. The required fast cluster explosion leading to an extended

plasma of homogeneous density $n_{cr}^{(e)}$, could, however, not be achieved in the range of parameters of our studies and, so far, we did not observe a significant resonant contribution to the electron heating.

6.2 Cluster charging

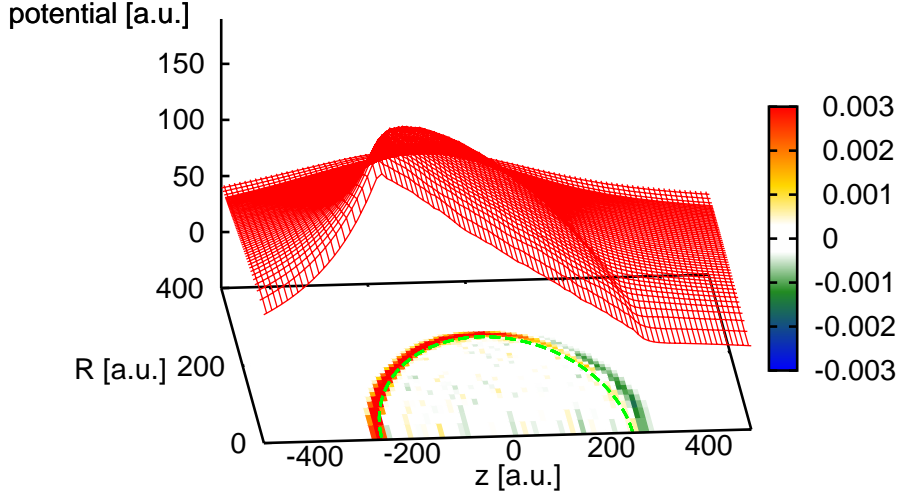


Figure 6.4: Snapshot of the charge density $\rho(R, z)$ (color coding in a.u.) and the corresponding electrostatic potential $\phi(R, z)$ (line plot) at $t = 61$ fs. ($N = 2.8 \cdot 10^5$, $\tau = 61$ fs, $I = 4.3 \cdot 10^{15}$ Wcm $^{-2}$)

As the interaction with the laser proceeds, a fraction of the electrons exits the cluster and leaves behind a net positive charge. Due to the mobility of the quasi-free electrons, the positive charge is situated at the cluster surface while the cluster interior remains quasi-neutral, just as one would expect of a charged metallic sphere. Consequently, the charging of the cluster results in a monopole component of the mean field outside the cluster which adds up to the dipole component introduced by the cluster polarization. Inside

the cluster the effective field remains unchanged. The combination of the two effects (charging of the cluster and polarization of the cluster) leads to an asymmetry of the mean field along the z -axis. At one cluster pole (right pole in fig. 6.4) part of the positive background charge is compensated by the displaced electron cloud, thus flattening the potential barrier at the cluster border. At the other pole (left pole in fig. 6.4) a sheath region with a large number of unbalanced ionic charges and a strongly enhanced electric field arises. Half a laser cycle later, the roles of the two poles are interchanged.

Chapter 7

Ionization of the cluster ions

A main influence on the cluster dynamics is the collective motion of the electrons which is at the origin of the screening of the laser field inside the cluster. The effectiveness of the screening, and thus the magnitude of the effective field available for heating the particles, is governed by the electronic density. The more quasi-free electrons are freed in the cluster, the higher the plasma frequency $\omega_P = \sqrt{4\pi n^{(e)}}$, and the more effective the screening will be. The degree of ionization of the cluster ions will thus not only be of importance for the ionic dynamics, but also strongly influence the evolution of the electronic ensemble.

When the intensity of the impinging laser pulse first reaches the threshold for over-barrier ionization of neutral argon ($F_L(t_{OBI}) \approx 0.08$ a.u.), the cluster atoms are ionized and the quasi-free electrons and ions form a cold “nanoplasma” of solid density within the initial boundaries of the cluster. For a pulse with a peak intensity of $I = 4.3 \cdot 10^{15} \text{ Wcm}^{-2}$ ($F_0 = 0.35$ a.u.) and a duration (see eq. (2.3)) of $\tau = 61$ fs, this first ionization takes place at $t_{OBI} = 28.5$ fs. Additional quasi-free electrons are efficiently produced throughout the laser pulse by successive ionization of the cluster ions (fig. 7.1). The M-shell is rapidly depleted and the mean ionic charge state reaches $\langle q \rangle \approx 9+$ by the end of the pulse.

After the first ionization event by over-barrier ionization, field ionization is efficiently suppressed as the quasi-free electrons screen the electric field inside the cluster. At the cluster poles however, the enhancement of the local electric field by cluster polarization and charging ensures a rapid field ionization of the M-shells of the local ions early on in the laser pulse (fig. 7.2). Electron impact ionization proceeds more slowly in the entire cluster, but eventually catches up with the field ionization at the surface, and approximately at the pulse maximum ($t = 86$ fs) no radial dependence of the average ionic charge state can be observed anymore.

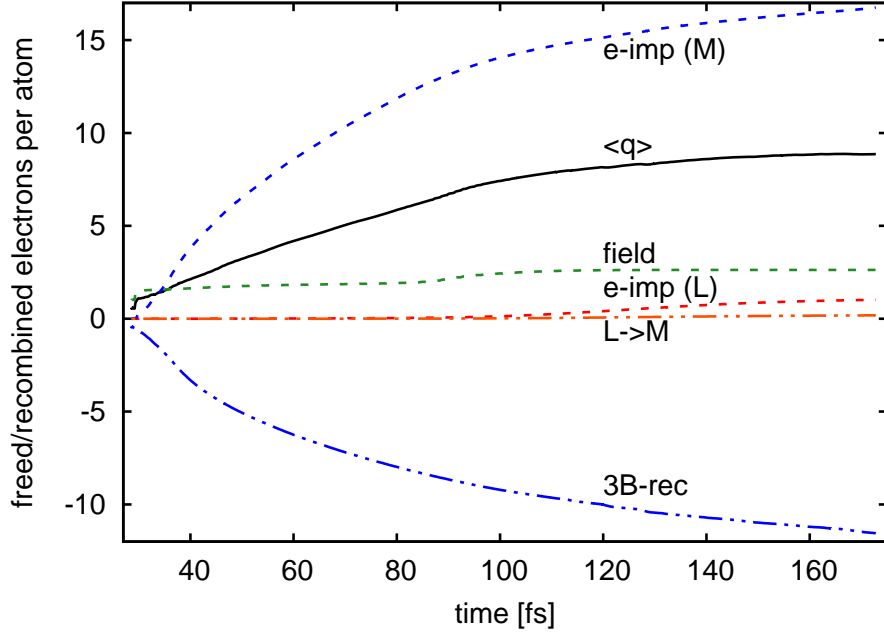


Figure 7.1: Time dependence of the mean ionic charge state $\langle q \rangle$ (black line) in a $N = 2.8 \cdot 10^5$ cluster irradiated by a pulse with $\tau = 61$ fs and $I = 4.3 \cdot 10^{15}$ Wcm $^{-2}$. The number of electrons per ion ionized or recombined by the various contributing mechanisms are also plotted (dashed lines, see text).

For the major part of the cluster, the dominant ionization mechanism throughout the laser pulse is electron-impact ionization of the M-shell (see fig. 7.1). On average, every ion experiences 17 impact events involving the M-shell during the laser pulse. This exceeds considerably the number of M-shell electrons in neutral argon ($N_M = 8$), which is made possible by the continuous repopulation of the M-shell by three-body recombination of the slow quasi-free electrons. In order to illuminate the role of this mechanism, an additional simulation where three-body recombination is turned off has been performed. The difference between the two cases is minimal: the dynamics is practically identical. Only the ionic charge state distributions (fig. 7.3) show a noticeable effect: a small fraction of weakly charged argon ions ($4 - 7+$) is present when including three-body recombination, while without recombi-

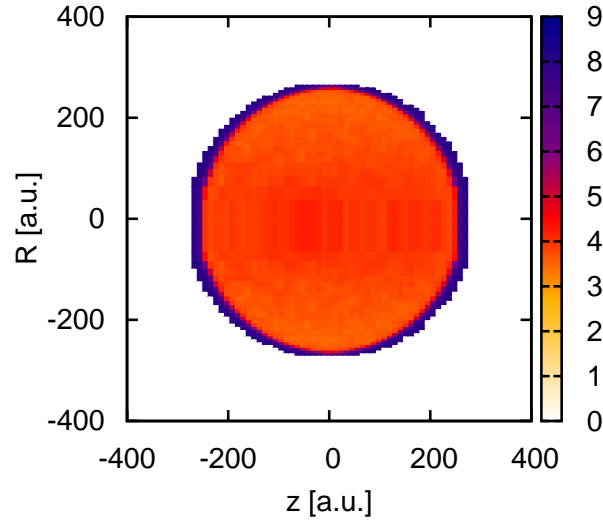


Figure 7.2: Snap-shot of the spatial distribution of ionic charge states at $t = 56$ fs. ($N = 2.8 \cdot 10^5$, $I = 4.3 \cdot 10^{15} \text{ Wcm}^{-2}$ and $\tau = 61$ fs).

nation the quasi-totality of the ions has an empty M-shell by the end of the pulse. At higher laser intensities, recombination ensures a small population of the M-shell even in highly charged ions (with depleted L-shell). This population has also been observed experimentally in the form of $K\beta$ radiation coming from $3p \rightarrow 1s$ deexcitation in Ar^{16+} [Prigent, 2004].

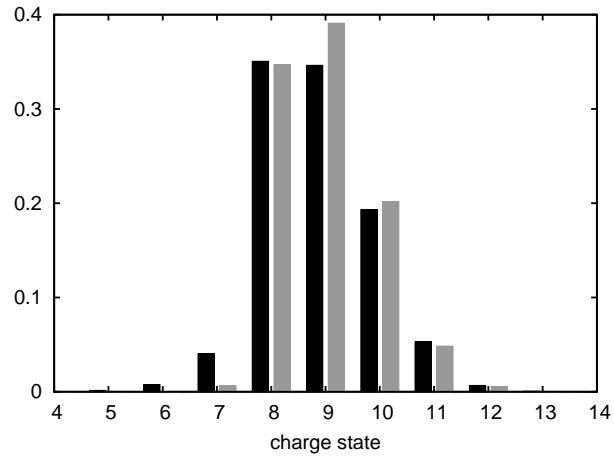


Figure 7.3: Ionic charge state distribution at the conclusion of the laser pulse. Results when three-body recombination is included (black) and when recombination is turned off (gray). ($N = 2.8 \cdot 10^5$, $I = 4.3 \cdot 10^{15} \text{ Wcm}^{-2}$ and $\tau = 61 \text{ fs}$).

Chapter 8

Electron dynamics

The electrons are the main actors in the laser-cluster interaction. Their dynamics determine self-consistently the evolution of the mean field. The electrons determine the atomic configurations of the cluster ions via impact ionization and impact excitation, and are at the origin of the inner-shell vacancies responsible for the experimentally accessible X-ray radiation. In this chapter, we first examine the kinetic electron energy distributions. We then focus on the subensemble of fast electrons and investigate the underlying heating mechanism. Finally, the influence of the fast electron dynamics on the electric fields inside the cluster is studied.

8.1 Energy distributions

The quasi-free electrons inside the cluster experience an effective electric field that is considerably weaker than the laser field. Consequently the heating of the electrons is slow and the vast majority of the electrons have kinetic energies well below the ponderomotive energy U_P of the free laser field (see fig. 8.1). The continuous production of additional slow electrons by ionization events further cools the electron ensemble. Electron-electron collisions allow for a thermalization of the electrons, and a large fraction of the ensemble is very well represented by a Maxwell-Boltzmann distribution with a time-dependent temperature $T(t)$ [Deiss and Burgdörfer, 2007]:

$$f_T(E) \propto \sqrt{\frac{E}{T^3}} \exp\left(-\frac{E}{T}\right). \quad (8.1)$$

A strong deviation from the Maxwell-Boltzmann distributions can be observed for the high-energy tail of the distribution, where the simulation results are grossly underestimated by equation (8.1). This suggests inherently

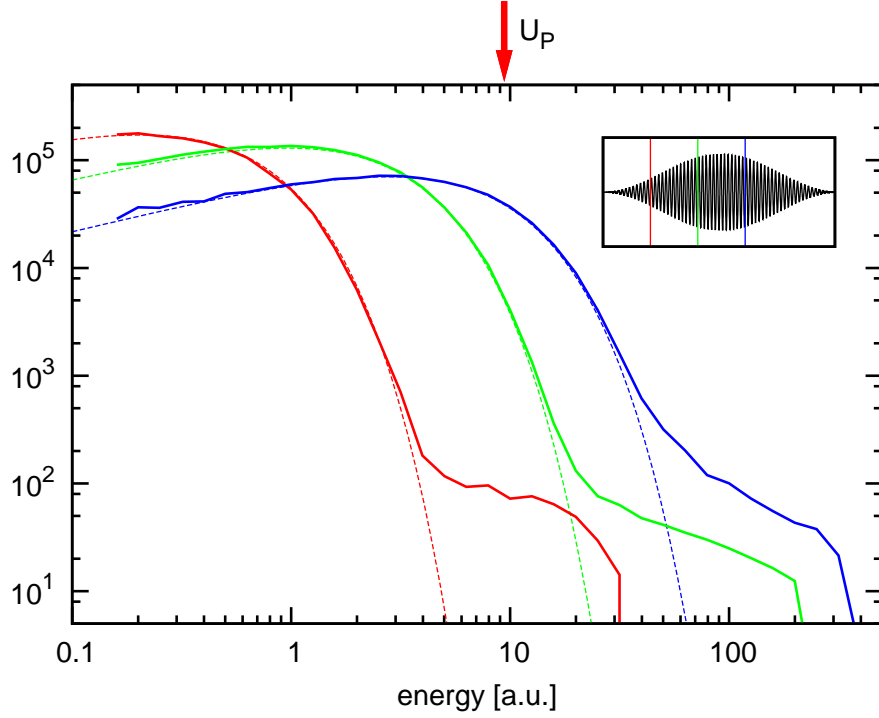


Figure 8.1: Kinetic energy distribution of the quasi-free electrons inside the cluster ($r < 0.7R_{cl}$) at different times during the laser pulse: $t_1 = 35$ fs (red), $t_2 = 69$ fs (green) and $t_3 = 104$ fs (blue). The dashed lines represent Maxwell-Boltzmann energy distributions with $T(t_1) = 0.4$ a.u. (red), $T(t_2) = 1.9$ a.u. (green) and $T(t_3) = 5.5$ a.u. (blue). The ponderomotive energy of the free laser field is $U_P \simeq 9.4$ a.u.. ($N = 2.8 \cdot 10^5$, $I = 4.3 \cdot 10^{15}$ Wcm $^{-2}$ and $\tau = 61$ fs).

different dynamics for the fast electrons, which will be discussed in detail in the next section. Due to their very small number, the ensemble of fast electrons will not have a big influence on the global evolution of the cluster. The “slow” electrons will be the ones that control, for example, the ionization of the cluster ions and the charging of the cluster (and thus the cluster expansion). Nevertheless, when it comes to X-ray spectroscopy, the subensemble of fast electrons plays the crucial role, as it controls the absolute number of emitted characteristic X-ray photons by producing the necessary K-shell vacancies by electron-impact ionization. The slow-electron ensemble, which is responsible for the outer-shell ionization of the cluster ions, leaves its fingerprint on the experiments via the ionic charge-state distributions extracted

from high-resolution X-ray spectra.

8.2 Fast-electron dynamics

In this section we will consider the highly efficient heating mechanism generating the fast electron population visible in fig. 8.1 [Deiss and Burgdörfer, 2007; Prigent et al., 2008]. We start out by searching for the subset of fast electrons within the ensemble of electrons depicted in fig. 8.2a. This snapshot is taken 6 laser cycles after the maximum of the laser pulse at $t = 105$ fs. At this stage of the interaction, part of the electrons could already leave the cluster, and the combination of charging and polarization of the cluster produces a strong asymmetry in the electric field as discussed in section 6.2 (fig. 8.2c). The shift of the high density electron cloud towards negative z values compensates the positive background charge at the left cluster pole, thus suppressing the electric field. On the right pole, the electron depletion, due to both polarization and charging, produces a sheath region with a strongly enhanced electric field. As can be seen when depicting the electron density on a logarithmic scale (fig. 8.2a), a small fraction of electrons occupies this sheath region to the right of the cluster. Examining the spatial dependence of the mean kinetic energy distribution (fig. 8.2b) identifies these electrons in the sheath region as fast electrons.

The link between the periodically building-up and collapsing sheath regions and the dynamics of the fast electrons can best be understood when examining the electronic phase space. The phase space projection (z, v_z) for a subset of electrons within $R < 50$ a.u. of the z -axis is shown in figure 8.3 for three instants during half a laser cycle. The elongated high-density strip (gray in fig. 8.3) along the horizontal axis represents the slow electrons inside the cluster, which are well represented by Maxwell-Boltzmann distributions as discussed in section 8.1. The fast electrons (blue) are heated in the sheath regions at the cluster poles (red arrows): when the sheath collapses at the pole (i. e. the electric field is suppressed due to charge compensation), a small fraction of the slow electron population can leak out of the cluster (fig. 8.3a). As soon as the sheath builds up again, these electrons are strongly accelerated back into the cluster (fig. 8.3b) and travel through the cluster as a front of fast electrons (fig. 8.3c). The situation at the poles is inverted after half a laser period (compare green and red arrows in 8.3a and 8.3c) and new electrons can get accelerated.

Similar heating mechanisms have also been discussed for laser pulses impinging on solid surfaces [Brunel, 1987] and for capacitively coupled radio-frequency discharges [O’Connell et al., 2007; Vender and Boswell, 1992]. In

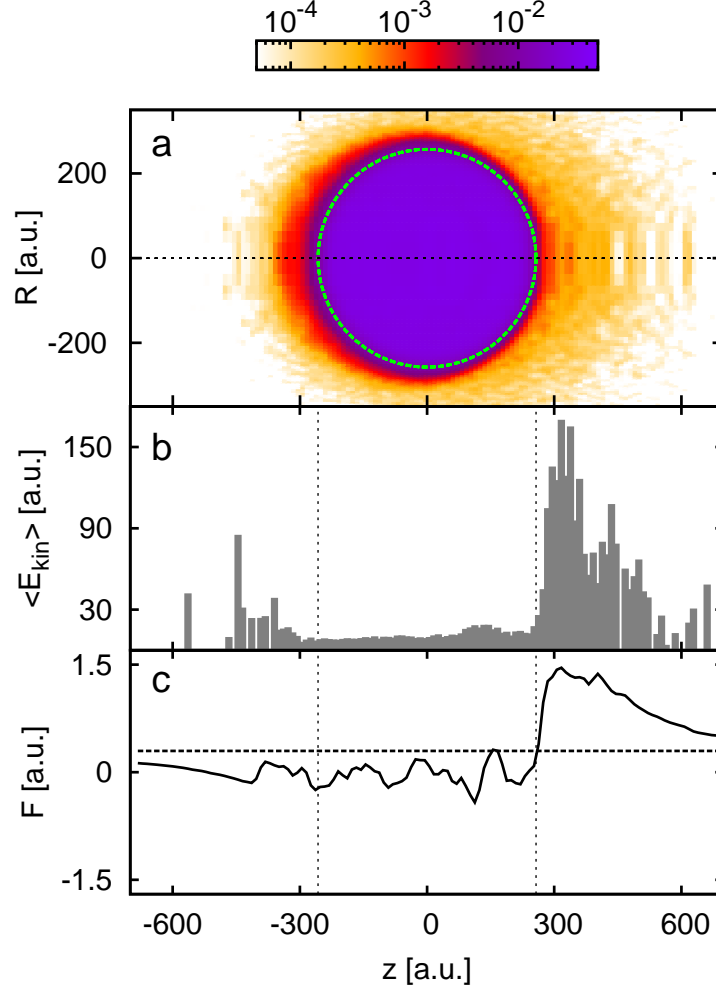


Figure 8.2: a) Spatial density distribution (in a.u.) of the quasi-free electrons on a logarithmic scale. b) Spatial dependence of the mean kinetic electron energy along the z -axis (linear scale). c) Total electric field $F_z(R = 0, z) = F_L(t) + F_z^{(mean)}(R = 0, z)$ along the z -axis (linear scale). The dashed line marks the laser field strength $F_L(t) = 0.30$ a.u.. All snapshots are taken at $t = 105$ fs. The green circle in a) and the dotted vertical lines in b) and c) represent the initial cluster boundaries. ($N = 2.8 \cdot 10^5$, $I = 4.3 \cdot 10^{15} \text{ Wcm}^{-2}$ and $\tau = 61$ fs).

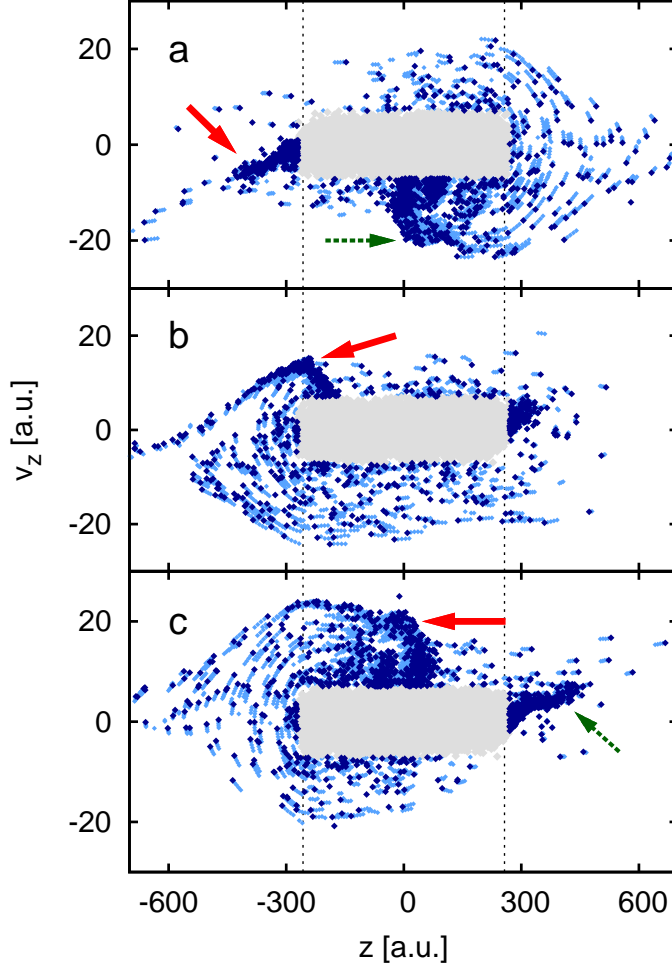


Figure 8.3: Evolution of the projected electron phase space (z, v_z) during half a laser cycle (a-c: $t = 96.8$ fs, $t = 97.6$ fs and $t = 98.2$ fs). Only electrons within $R < 50$ a.u. of the z -axis are represented. Gray: High density region of slow electrons inside the cluster. Blue: Electrons outside the cluster and fast electrons inside the cluster. The light-blue traces mark the path of the electrons over the previous 0.04 fs. The vertical lines show the original cluster borders. The red arrows point out the generation (a), acceleration (b) and transit (c) of the fast-electron ensemble. ($N = 2.8 \cdot 10^5$, $I = 4.3 \cdot 10^{15}$ Wcm $^{-2}$ and $\tau = 61$ fs).

a 2D PIC code where the cluster is represented by an infinitely long cylinder [Gupta et al., 2006; Taguchi et al., 2004], the authors suggest a resonant heating mechanism for the production of fast electrons which after traversing the cluster during half a laser cycle, reemerge at the other pole in phase with the laser. For long pulse durations, several bunches of fast electrons transiting through the cluster were observed and interpreted as higher-order resonances [Gupta et al., 2006]. However, for all cluster sizes and laser parameters we have examined, we could not observe any clear signature of such resonance effects for our spherical clusters. Indeed, the complex spatial and temporal evolution of the electric field and the broad velocity distribution of the fast electrons (fig. 8.3) make the formation of a sharp resonance rather unlikely. The present heating scenario does not invoke a resonance condition. In fact a large fraction of the fast electrons crosses the cluster several times, without, however, increasing on average their energy significantly from one passage to the next.

Additional insights into the heating mechanism and its link to the production of X-rays can be gained when examining in fig. 8.4 the maximum kinetic energy E_{\max} of electrons inside the cluster (i. e. the cut-off energy of the energy distribution in fig. 8.1). The time dependence of E_{\max} is governed by the evolution of the electrostatic potential $\phi(\mathbf{r} = 0, t)$ at the center of the cluster. The potential energy $\phi(\mathbf{r} = 0, t)$ gives the maximum kinetic energy an electron can gain in the monopole field produced by the charging of the cluster. This estimate can be improved by additionally taking into account the maximum energy $F_{\text{osc}}^2/(2\omega^2)$ electrons can get from the acceleration in the oscillating field created at the cluster poles by the laser and the cluster polarization. The maximal amplitude F_{osc} of this oscillating field is sampled on the z -axis during every laser cycle. An analytical estimate of F_{osc} would be eq. (6.4). The accuracy of this estimate is however limited as it relies on the assumption, that the cluster behaves like a polarizable sphere.

The production of X-rays sets in as soon as the fastest electrons in the cluster reach the threshold energy $E_K = 117$ a.u. necessary for producing a vacancy in the K-shell of a moderately charged argon ion ($q < 8$) by electron impact. Examining the evolution of E_{\max} for different laser intensities, we can predict according to fig. 8.4 an intensity threshold for X-ray production between $7 \cdot 10^{14} \text{ Wcm}^{-2}$ and $1.6 \cdot 10^{15} \text{ Wcm}^{-2}$. For $I = 1.6 \cdot 10^{15} \text{ Wcm}^{-2}$ the maximum energy barely exceeds E_K and K-shell vacancies are produced. For lower laser intensities ($I = 7 \cdot 10^{14} \text{ Wcm}^{-2}$), the charging of the cluster is not sufficient for the electrons to reach E_K . This is a little below the experimentally observed threshold $I_{th} = 1.9 \cdot 10^{15} \text{ Wcm}^{-2}$ (see fig. 1.2). Considering that due to the detection threshold, the experiment should slightly overestimate the intensity threshold, the agreement is very good. We can conclude

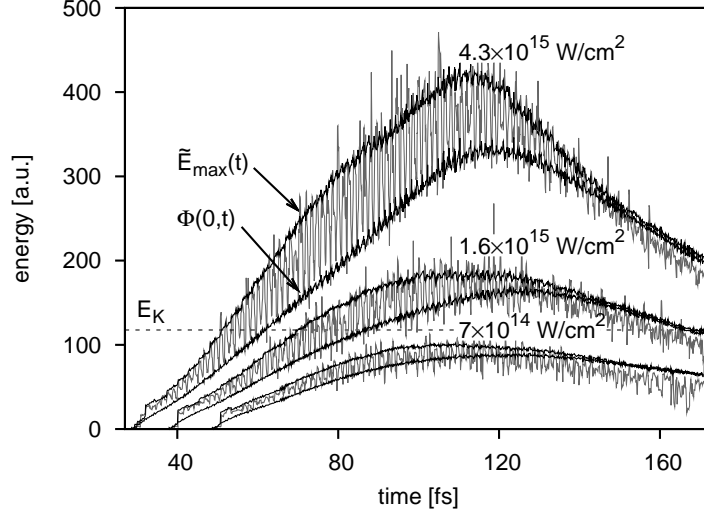


Figure 8.4: Time evolution of the maximum kinetic energy E_{\max} (gray) in the high density core of the cluster for three peak laser intensities, $I = 7 \cdot 10^{14} \text{ Wcm}^{-2}$ (lower curve), $I = 1.6 \cdot 10^{15} \text{ Wcm}^{-2}$ (center curve) and $I = 4.3 \cdot 10^{15} \text{ Wcm}^{-2}$ (upper curve). The dashed horizontal line marks the neutral argon K-shell binding energy $E_K = 117 \text{ a.u.}$. Each curve is delimited below by the electrostatic potential $\phi(\mathbf{r} = 0, t)$ at the center of the cluster and above by $\tilde{E}_{\max}(t) = \phi(\mathbf{r} = 0, t) + F_{\text{osc}}^2/(2\omega^2)$ (see text). ($N = 2.8 \cdot 10^5$ and $\tau = 61 \text{ fs}$).

that $\tilde{E}_{\max}(t) = \Phi(\mathbf{r} = 0, t) + F_{\text{osc}}^2/(2\omega^2) = E_K$ predicts reliably the threshold for the production of K-shell vacancies and, in turn, K X-ray emission.

8.3 Wake fields

The phase space projection (fig. 8.3) also provides an explanation for the perturbation of the electric field inside the cluster observed between $t \approx 90 \text{ fs}$ and $t \approx 120 \text{ fs}$ in fig. 6.3: the transiting front of fast electrons (red arrow in fig. 8.3c) disturbs the colder background plasma in the cluster and a wake field oscillating at the local plasma frequency is formed behind the electron front. The details of the wake field can be studied in fig. 8.5, where both the temporal and spatial dependence of the z -component of the electric field

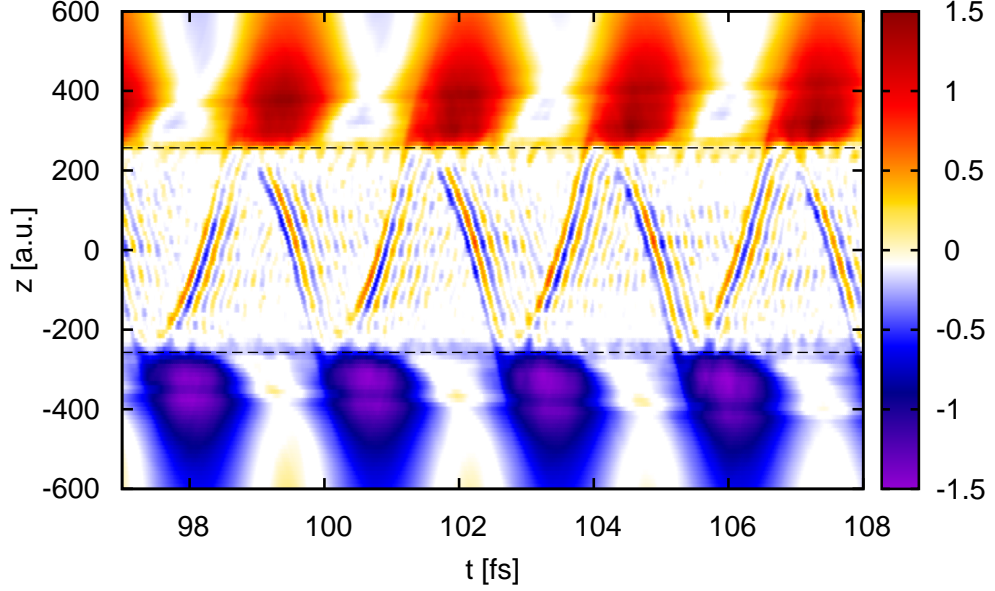


Figure 8.5: Total electric field in a.u. along the z -axis $F_z(R = 0, z, t) = F_L(t) + F_z^{(\text{mean})}(R = 0, z, t)$. The dashed black line marks the initial cluster boundaries. ($N = 2.8 \cdot 10^5$, $I = 4.3 \cdot 10^{15} \text{Wcm}^{-2}$ and $\tau = 61 \text{fs}$).

are depicted: a vertical cut through the plot gives the instantaneous electric field profile along the z -axis (as in fig. 8.2c), while a horizontal cut displays the time-dependence of the local field (as in fig. 6.3). A time interval corresponding to 4 laser cycles is shown. Outside the initial cluster boundaries ($z > 257 \text{ a.u.}$ and $z < -257 \text{ a.u.}$), the periodic building-up and collapsing of the sheath regions can be observed. The regions close to the initial cluster radius ($257 \text{ a.u.} \lesssim |z| \lesssim 400 \text{ a.u.}$) are marked by small field irregularities caused by the low-density ionic background from the slowly expanding cluster. In these regions the highly charged sheaths build-up every half cycle as the electron cloud is pushed toward the opposite cluster pole. The excess positive charge is at the origin of the strong electric field accelerating electrons toward the cluster. As the electron cloud oscillates back, the sheath collapses half a cycle later and the field amplitude goes nearly to zero. Inside the cluster,

the field is very weak due to the screening of the laser field by the cluster polarization. The wake field can therefore manifest itself as a very clear zig-zag structure bouncing between the cluster boundaries. Each laser half cycle, the front of fast electrons originates at the pole where the electric field is strong and then transits the cluster. At a given point along the z -axis inside the cluster, the short presence of excess negative charge, created by the passage of the fast electrons, disturbs the local quasi-neutrality of the plasma. This induces an oscillation of the local charge density (and thus of the local electric field) with the plasma frequency $\omega_P = \sqrt{4\pi n^{(e)}}$ [Mitcher, 1973]. These oscillations in the temporal domain can be clearly seen in fig. 8.5. During the time $2\pi/\omega_P$ the local density needs to perform a full oscillation, the fast electron front has traveled the distance λ_P further along the z -axis according to its velocity $v_z^{(fe)}$. $\lambda_P = 2\pi v_z^{(fe)}/\omega_P$ corresponds therefore to the wavelength of the spatial oscillations of the wake field, trailing behind the electron front.

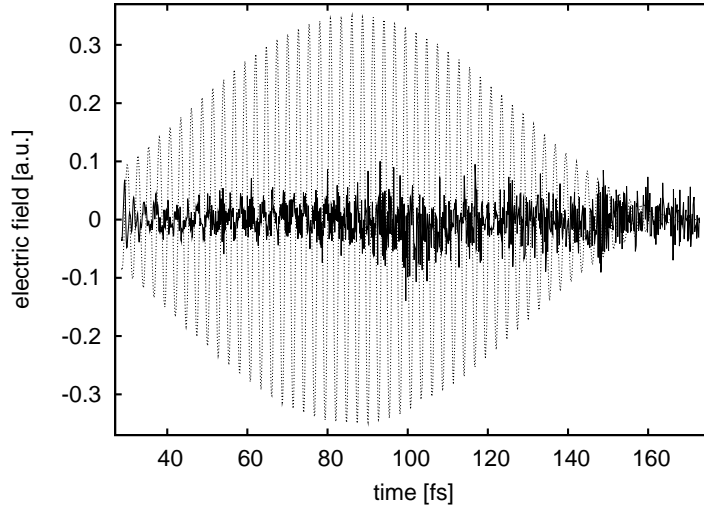


Figure 8.6: Local electric field (z -component) in the interior of the cluster at ($R = 0, z = 10.7$ a.u.). The charge density contribution of fast electrons with $|v_z| > 10$ a.u. was neglected. In comparison with fig. 6.3, the wake fields are strongly suppressed. The laser field is also plotted (dotted gray line). ($N = 2.8 \cdot 10^5$, $\tau = 61$ fs, $I = 4.3 \cdot 10^{15}$ Wcm $^{-2}$)

In order to check, whether the fast electrons are truly at the origin of the observed field fluctuations, we performed an additional simulation, in

which fast electrons with $|v_z| > 10$ a.u. are not taken into account when evaluating the charge density distribution. As this restriction affects only a very small fraction of the electron ensemble, the global charge neutrality is not strongly affected. In this simulation, the appearance of wake fields is efficiently suppressed (compare figs. 8.6 and 6.3). Nevertheless, the mean ionic charge state, electron energy distributions etc. are very similar to the case with the wake field present. Also the X-ray yield is only 10% lower than in the case with wake fields. We can therefore conclude that, at least in the present parameter regime, the wake fields are not of importance for the dynamics of the laser-cluster interaction.

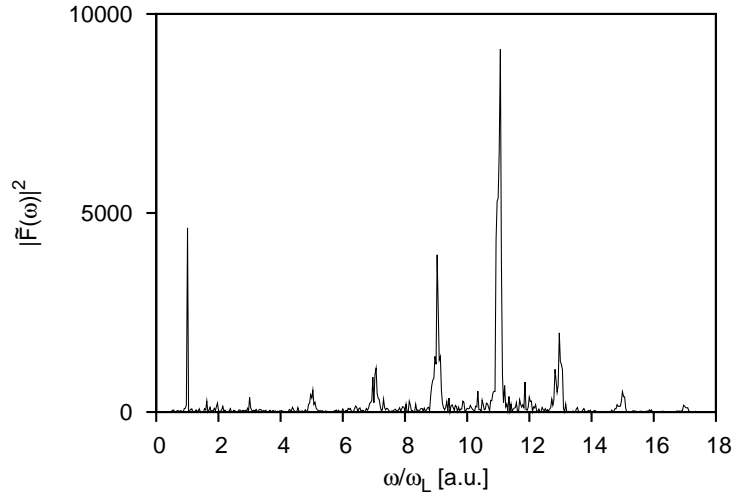


Figure 8.7: Fourier spectrum of the local electric field (z -component) at the cluster center. ($N = 2.8 \cdot 10^5$, $\tau = 61$ fs, $I = 4.3 \cdot 10^{15}$ Wcm $^{-2}$)

The time dependence of the electric field inside the cluster (fig. 6.3) suggests the presence of high frequency components. For a closer study, we calculate the Fourier spectrum $|\tilde{F}(\omega)|^2$ of the z -component of the electric field at the cluster center with:

$$\tilde{F}(\omega) = \int_0^{2\tau} F_z(\mathbf{r} = 0, t) e^{-i\omega t} dt. \quad (8.2)$$

The spectrum displays peaks at the laser frequency $\omega_L = 0.057$ a.u. as well as at its odd harmonics up to $17\omega_L$ (fig. 8.7). The height of the peaks increases

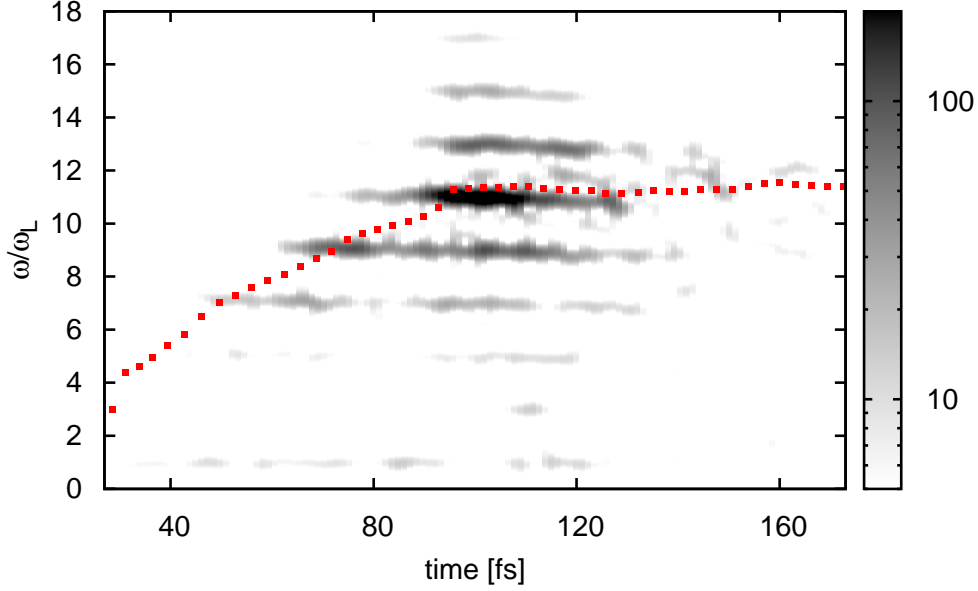


Figure 8.8: Time-frequency analysis of the local electric field (z -component) at the cluster center. Note the logarithmic gray scale of $|\tilde{F}(\omega, t)|^2$. The time-dependent local plasma frequency $\omega_P(\mathbf{r} = 0, t)$ is marked by the red dots. ($N = 2.8 \cdot 10^5$, $\tau = 61$ fs, $I = 4.3 \cdot 10^{15}$ Wcm $^{-2}$)

strongly up to the 11th harmonic, after which the harmonics appear to be more and more suppressed until the 17th harmonic which is barely visible. In order to illuminate the origin of these harmonic contributions, we perform a time-frequency analysis of the electric field by multiplying the electric field by a Gaussian window function of length $\Delta T = 2.4$ fs and making several Fourier transforms as the window moves along the time axis:

$$\tilde{F}(\omega, t) = \int_0^{2\tau} F_z(\mathbf{r} = 0, t') e^{-\frac{(t-t')^2}{\Delta T^2}} e^{-i\omega t'} dt'. \quad (8.3)$$

The analysis reveals that the odd harmonics appear consecutively during the laser pulse (fig. 8.8). Up to $n = 11$, the appearance of the n -th harmonic coincides well with the condition $\omega_P = n\omega_L$. The local plasma frequency $\omega_P(t) = \sqrt{4\pi n^{(e)}(\mathbf{r} = 0, t)}$ increases as more and more electrons are produced

by ionization inside the cluster, fulfilling consecutively the condition up to $n = 11$. As ionization saturates, the plasma frequency stabilizes at $\omega_P(t) \approx 11\omega_L$ and the 11th harmonic is strongly enhanced. During the time where the wake fields are strongest (between $t \approx 90$ fs and $t \approx 120$ fs), the higher harmonics 13 to 17 appear, suggesting strongly nonlinear dynamics. When making the same frequency analysis for the field with the suppressed wake fields (fig. 8.6), the 9th and the 11th harmonics appear in a similar way, albeit with lower intensity, while the high harmonics with $n > 11$ are not visible. Fomichev et al. described the appearance of odd harmonics in the field inside small ($N \sim 1000$) clusters as “nonlinear excitations of the dipole surface plasmon” and linked them to the evolution of the Mie frequency $\omega_{\text{Mie}} = \omega_P/\sqrt{3}$ [Fomichev et al., 2005]. As we observe in our much larger clusters a clear link to the plasma frequency $\omega_P = \sqrt{4\pi n^{(e)}}$ as opposed to ω_{Mie} , we interpret the harmonics up to $n = 11$ as the excitation of local plasma fluctuations by the laser field (not linked to a surface plasmon), and attribute the highest harmonics ($n > 11$) to the perturbation by the wake fields.

Chapter 9

Cluster disintegration

As a final aspect of the dynamics of a single cluster in a laser field, we study in this chapter the ionic dynamics and their influence on electron heating and K-shell vacancy production.

9.1 Ion dynamics

The cluster expansion is driven by the monopole field, that builds up as more and more quasi-free electrons leave the cluster. As the inside of the cluster is shielded by the electrons, the expansion proceeds starting with the ions on the cluster surface, resulting in a radially declining and spherically symmetric ion density profile. This can be observed in fig. 9.1 for the case of a cluster with $N = 3.7 \cdot 10^4$ atoms irradiated by a pulse with $\tau = 140$ fs and $I = 4.3 \cdot 10^{15} \text{ Wcm}^{-2}$. The kinetic energy of the ions is highest at the outer expansion front where it reaches ~ 130 keV at the end of the pulse, and drops when approaching the cluster center (fig. 9.2). A slight asymmetry can be observed for the fastest ions: the maximum kinetic energy of the ions emitted in laser polarization direction is approximately 10 to 20% higher than the maximum energy reached by ions travelling perpendicular to the polarization axis (fig. 9.3). This is a direct result of the enhancement of the electric field at the cluster poles and has also been observed experimentally [Kumarappan et al., 2001a].

A full quantitative comparison of our simulation results with ion spectroscopy experiments would require us to follow the ions till they reach the apparatus which corresponds to times of flight of the order of microseconds. This post-processing of the ion trajectories would need to include the contribution of clusters from the whole focal volume [Islam et al., 2006] and the interaction of their emitted ions, as well as the cooling of the plasma envi-

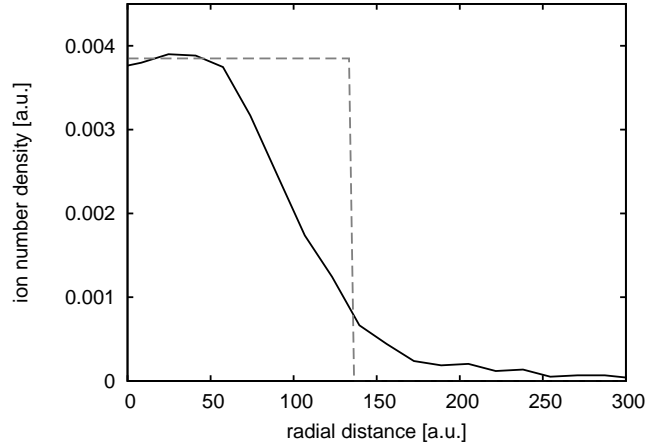


Figure 9.1: Radial dependence of the ion number density $n^{(i)}(r)$ at $t = 186$ fs (full line). The dashed line marks the initial density distribution at $t = 0$ fs. ($N = 3.7 \cdot 10^4$, $I = 4.3 \cdot 10^{15} \text{ Wcm}^{-2}$ and $\tau = 140$ fs).

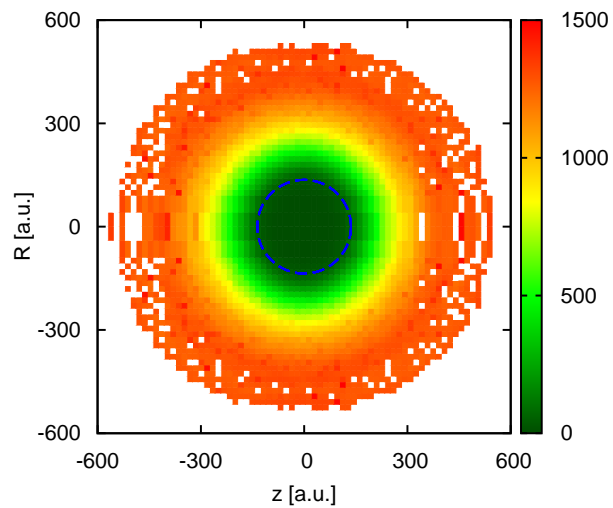


Figure 9.2: Spatial dependence of the mean ion kinetic energy (in a.u.). The snapshots was taken at $t = 186$ fs. The dashed circle marks the initial cluster boundaries. ($N = 3.7 \cdot 10^4$, $I = 4.3 \cdot 10^{15} \text{ Wcm}^{-2}$ and $\tau = 140$ fs).

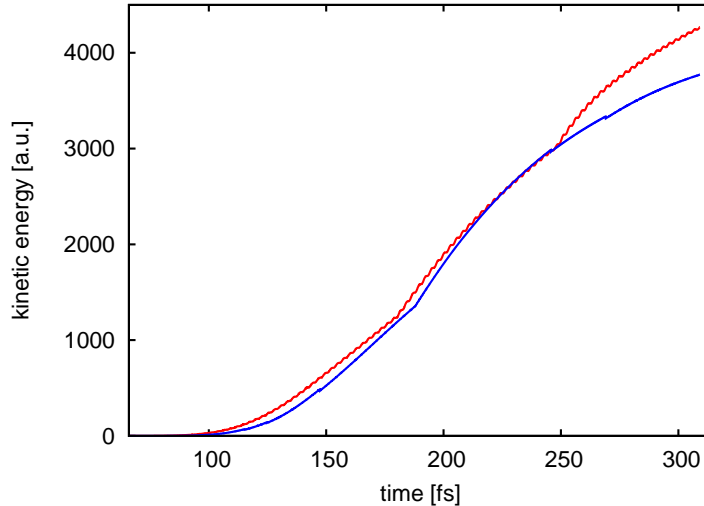


Figure 9.3: Kinetic energy of the fastest ion moving parallel (red) and of the fastest ion moving perpendicular (blue) to the laser polarization axis ($N = 3.7 \cdot 10^4$, $I = 4.3 \cdot 10^{15} \text{ Wcm}^{-2}$ and $\tau = 140 \text{ fs}$).

ronment after the end of the laser pulse and possible recombination events with free electrons. As this is beyond the scope of our simulation, we can not make comparisons with experimentally measured ion energy spectra. We nevertheless note that our maximum ion energy at the end of the laser pulse of approximately 5000 a.u. (or 130 keV) is very close to the experimentally measured cut-off of the energy distribution that lies between 10^5 and $2 \cdot 10^5 \text{ eV}$ [Kumarappan et al., 2001a].

9.2 Dynamics inside an expanded cluster

For a better understanding of the influence of the cluster expansion on the electron dynamics, we follow more closely over a few laser cycles the ion density, electron density and electric fields of an expanded cluster (fig. 9.4). A relatively small cluster with $N = 3.7 \cdot 10^4$ atoms is irradiated by a pulse with $\tau = 140 \text{ fs}$ and a relatively weak intensity $I = 1 \cdot 10^{15} \text{ Wcm}^{-2}$ close to the threshold for X-ray production. The snapshots are taken shortly after the pulse maximum. At this point, while the ion density drops towards the clus-

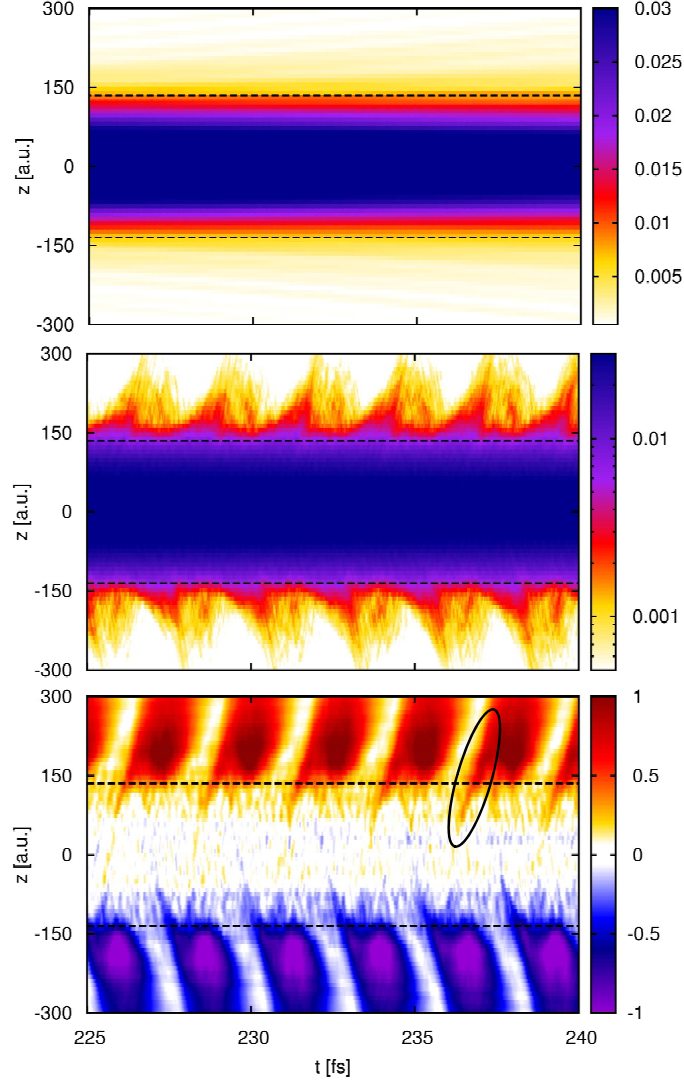


Figure 9.4: Top (linear scale): Time dependence of the ionic charge density along the z -axis. Center (logarithmic scale): Time dependence of the electron density along the z -axis $n^{(e)}(R = 0, z, t)$. Bottom (linear scale): Time dependence of the total electric field along the z -axis $F_z(R = 0, z, t) = F_L(t) + F_z^{(mean)}(R = 0, z, t)$. The circle points to one of the perturbations of the field by the fast electrons.

All color coding in a.u.. The dashed black lines mark the initial cluster boundaries. ($N = 3.7 \cdot 10^4$, $I = 1 \cdot 10^{15} \text{ Wcm}^{-2}$ and $\tau = 140 \text{ fs}$).

ter surface, the inner regions of the cluster still have the initial solid density. This density profile also manifests itself in the electron density profile, which closely follows the ionic density, and ensures local quasi-neutrality throughout most of the cluster. The quasi-neutrality breaks down periodically in the outer regions of the expanding cluster due to the driving of the electron ensemble by the laser field. This gives rise to the strong sheath fields responsible for effective electron heating as discussed in section 8.2. The sheath regions are localized close to the initial cluster radius (see fig. 9.4). Within the cluster, the laser field is again strongly screened.

Due to the weaker laser intensity, the wake fields produced by the fast electrons transiting the cluster are not as clearly visible at the center of the cluster as in figure 8.5. However, as the front of fast electrons passes over the density gradient, its perturbation of the electronic charge becomes more and more significant compared to the local electronic density. This explains the strong fields moving toward and across the cluster boundary (fig. 9.4). During the further evolution of the laser pulse, the effect of this enhanced wake field is twofold, affecting both the cluster expansion and the production of fast electrons. First, the strong wake helps the further acceleration of the ions in the region of the density gradient by enhancing periodically the field in a region of otherwise screened electric fields. Secondly, the outgoing fast electrons also strongly perturb the field in the region of the collapsed sheath, leading to an early appearance of the strong fields, even before the sheath rebuilds due to the oscillation of the cloud of slow electrons toward the opposite pole. Normally (i. e. in the absence of such field perturbations), the acceleration of electrons at the cluster border affects only the few electrons which stay behind as the electron cloud shifts away and the sheath builds up (see the phase space picture fig. 8.3). However, in the situation depicted in figures 9.4, the collapsed sheath is still populated by a large number of slow electrons at the time of arrival of the fast electrons. An enhanced number of electrons can thus be accelerated back into the cluster by the early build-up of strong fields due to the fast electron front.

9.3 Influence on the K-shell vacancy production

With the addition of the cluster explosion as the final ingredient to the cluster dynamics, we are now able to make predictions on the dependence of the K-shell vacancy production on laser parameters such as intensity and pulse duration.

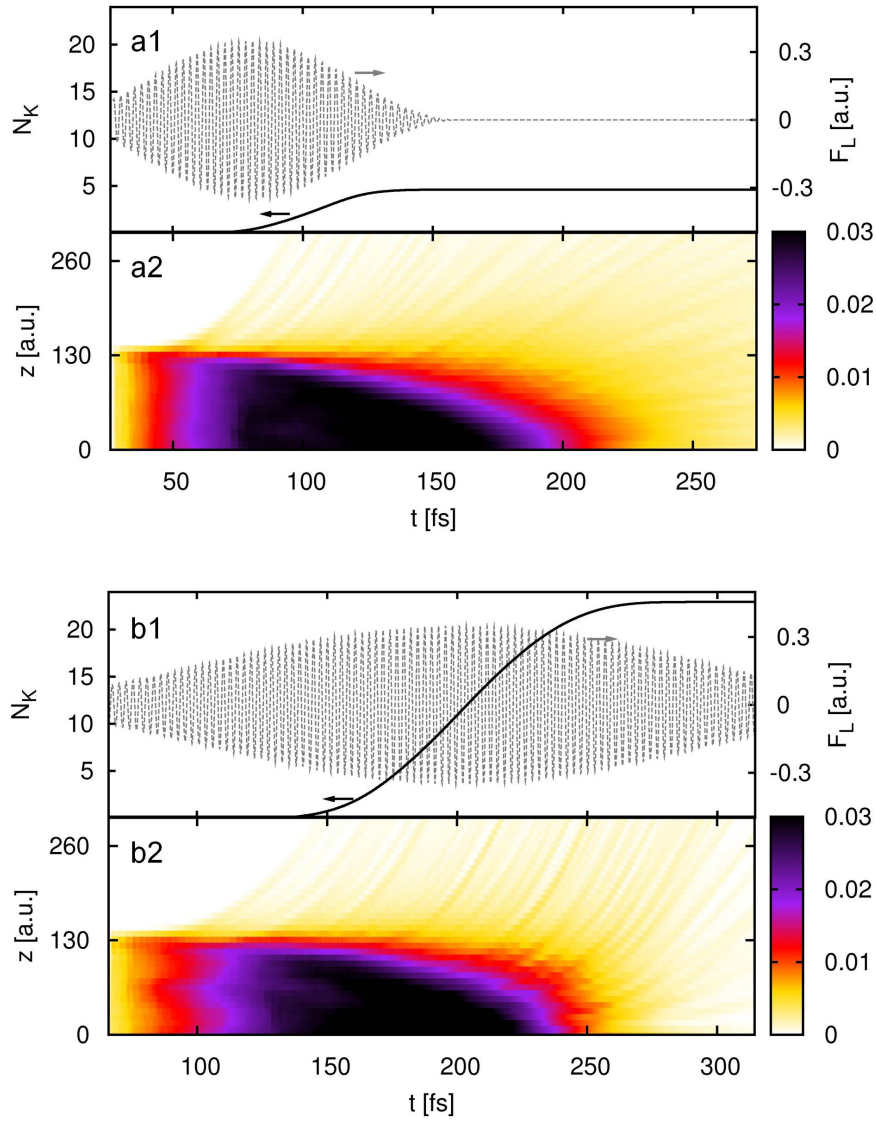


Figure 9.5: (1) Time dependence of the number N_K of K-shell vacancies (full line, left axis) and of the laser field F_L (dashed line, right axis). (2) Time dependence of the ionic charge density along the positive z -axis (in a.u.). Laser pulse duration of (a) $\tau = 56$ fs, and (b) $\tau = 140$ fs. ($N = 3.7 \cdot 10^4$ and $I = 4.3 \cdot 10^{15} \text{ Wcm}^{-2}$ for both plots).

We start out by comparing the evolution of a cluster with $N = 3.7 \cdot 10^4$ atoms irradiated by pulses with peak intensity $I = 4.3 \cdot 10^{15} \text{ Wcm}^{-2}$ and two different pulse durations $\tau = 56 \text{ fs}$ and $\tau = 140 \text{ fs}$. The evolution of the ionic charge density is very similar for both pulse lengths (fig. 9.5): after the first over-barrier ionization event ($t_{\text{OBI}} = 26 \text{ fs}$ for $\tau = 56 \text{ fs}$ and $t_{\text{OBI}} = 66 \text{ fs}$ for $\tau = 140 \text{ fs}$), the charge density quickly rises throughout the cluster due to electron-impact ionization. The cluster soon dissolves starting from the surface. The time needed until complete disintegration of the cluster is approximately 200 fs after the first ionization events, and is nearly identical for both pulse lengths (see fig. 9.5). As discussed in section 8.2, K-shell vacancies are created as soon as the cluster is charged enough to allow for the heating of electrons beyond E_K in the monopole field of the cluster. The ignition of K-shell vacancy production is thus related to the beginning of the cluster expansion which is also driven by the cluster charging. During the cluster expansion, K-shell vacancies are produced with a nearly identical rate for both pulse lengths. In the case of the shorter pulse, the K-shell production slows and finally stops as the end of the pulse nears and the laser is not strong enough anymore to effectively drive the electrons. At the end of the 56 fs pulse, the cluster explosion is not yet completed. For longer pulses, however, more time is available for the vacancy production, and vacancies are created until the cluster completely disintegrates, shortly after the pulse maximum. In this case, the K-shell vacancy production is quenched due to the lack of ionic collision partners for the fast electrons. It should be emphasized that the production of inner-shell vacancies is unrelated to any nanoplasma resonances (see section 6.1). The critical electron density for a nanoplasma resonance $n_{cr}^{(e)} = 3\omega^2/(4\pi) \simeq 0.0008 \text{ a.u.}$ is only reached towards the very end of the cluster explosion when the ionic density is by far too low for efficient K-shell vacancy production by electron-ion collisions.

These observations allow to make predictions about the influence of both pulse duration and laser intensity on the X-ray yield. At fixed laser intensity (fig. 9.6), the timing of the cluster explosion with respect to the pulse profile comes into play: for short pulses, the pulse is over before the cluster completely disintegrated, thus stopping the vacancy production prematurely. By increasing the pulse duration one allocates more time for the cluster charging and more and more vacancies are produced. Eventually the cluster disintegrates during the laser pulse and becomes thus the limiting factor. At this point the number of produced vacancies saturates. Finally, when going to very long pulses, the number of vacancies drops slightly as the cluster disintegrates before the laser pulse maximum is reached, thus experiencing weaker laser fields.

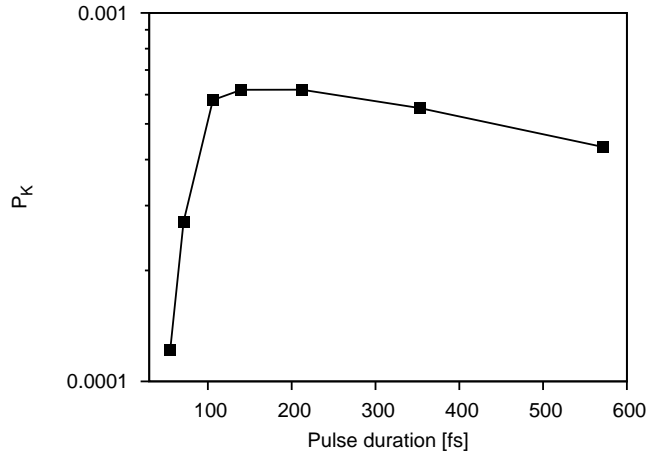


Figure 9.6: Pulse duration dependence of the number of K-shell vacancies produced per cluster atom in a cluster with $N = 3.7 \cdot 10^4$ atoms at fixed peak pulse intensity $I = 4.3 \cdot 10^{15} \text{ Wcm}^{-2}$.

A very similar trend can be observed at fixed laser pulse duration, when varying the laser intensity (fig. 9.7): close to threshold, the laser is just strong enough to allow for sufficient charging of the cluster to create a few electrons with $E > E_K$. As the laser intensity is increased, the vacancy production sets in earlier in the pulse and the yield increases until the fields are strong enough to cause a complete disintegration of the cluster during the laser pulse, at which point the number of K-shell vacancies saturates. At very high intensities, the yield decreases slightly, as the cluster explodes before the peak intensities are reached.

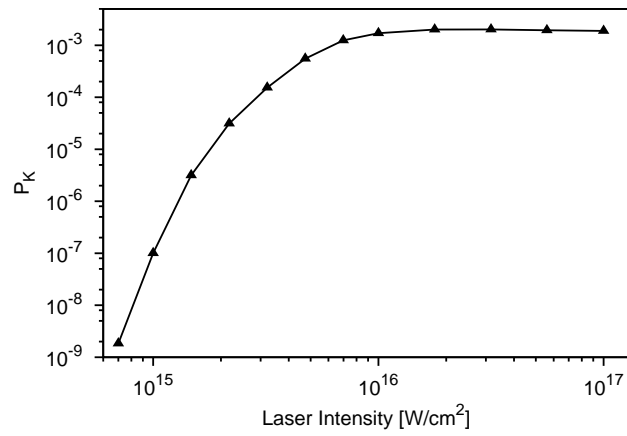


Figure 9.7: Intensity dependence of the number of K-shell vacancies produced per cluster atom in a cluster with $N = 2.8 \cdot 10^5$ atoms at fixed pulse duration $\tau = 61$ fs.

Part III

Comparison with X-ray
spectroscopy

Chapter 10

Description of the experiments

We give here a brief overview of those experimental characteristics which are of importance in the discussion of the results presented in this thesis. Details on the experimental set up and on the methods used to control the different parameters acting in the laser-cluster dynamics can be found in Prigent [2004] and Lamour et al. [2007] and references therein.

The experiments have been performed on the LUCA facility (French acronym for Ultra Short Tunable Laser) at Saclay, where the laser field is generated with a Ti:sapphire laser system delivering pulses of duration down to $\tau = 50$ fs at full width half maximum (FWHM), centered at $\lambda = 800$ nm with a repetition rate of 20 Hz. The laser beam diameter is approximately 50 mm before focusing, and the maximum pulse energy available in the interaction zone is 50 mJ. The laser light is focused by a 480 mm focal lens leading to a beam waist, i.e. a full width at $1/e^2$ in intensity, of $2w_0 = 311$ μm (corresponding to a Rayleigh distance $z_R = 0.95$ mm), and maximum peak intensities $I_{\text{peak}} \sim 10^{17}$ Wcm^{-2} . The I_{peak} values are determined by imaging the focal point on a CCD camera and from systematic measurements of the effective energy contributing to the peak intensity and of the laser pulse duration. The duration is accessed by second-order autocorrelation techniques that take into account the spatio-temporal aberrations induced by the lens (a maximum broadening of 18% is found at 50 fs while it drops down to less than 1% for a 200 fs pulse). Control of the laser parameters leads to an accuracy better than $\pm 20\%$ on I_{peak} values ranging from 10^{14} to 10^{17} Wcm^{-2} .

The clusters are produced by condensation of argon gas flowing at high pressure through a conical nozzle [Hagena and Obert, 1972]. The mean atomic density n_{mean} is proportional to the backing pressure P_0 , and a mean cluster-size scaling roughly with $\langle N \rangle \propto P_0^{1.8}$ is found [Prigent, 2004]. The average number of atoms per cluster $\langle N \rangle$ is obtained combining the Hagena semi - empirical laws [Buck and Krohne, 1996; Hagena, 1992] and a com-

pilation of recent experimental results [Schutte and Buck, 2002] in the size range studied here i.e. from 10^4 to 10^6 atoms per cluster. In the present experimental conditions, the mean atomic density is of the order of 10^{17} cm^{-3} and consequently the distance between clusters is $\sim 0.7 \mu\text{m}$. While the mean cluster size and the mean atomic density are relatively well known, further properties of the cluster jet can only be estimated from experimental studies with similar nozzles [Dorchies et al., 2003] supported by gas flow simulations [Boldarev et al., 2006]. Especially the fraction η of atoms condensating into clusters depends strongly on the thermodynamical and geometrical characteristics of the cluster jet and is not well known. Simulation results by Boldarev et al. [2006] reveal that clustering is typically not very efficient with $\eta \lesssim 0.5$ for all studied conditions. Moreover no clear parameter dependencies could be found and the clustering fractions are widely scattered in the range $0 < \eta < 0.4$. Another uncertainty is the cluster size distribution. Time of flight experiments with small krypton and xenon clusters ($\langle N \rangle \sim 5000$) [Schutte and Buck, 2002] are the only source of information presently available and suggest log-normal size distributions:

$$f(N) = \frac{1}{\sqrt{2\pi}\sigma N} \exp\left(-\frac{(\ln N - \mu)^2}{2\sigma^2}\right) \quad (10.1)$$

with $\mu = \ln\langle N \rangle - \sigma^2/2$ and $\sigma \sim 0.35$.

The nozzle is mounted on a solenoid pulsed valve, with an opening duration of $500 \mu\text{s}$, operated at a repetition rate from 20 Hz to 1 Hz and synchronized to the laser source. The spatial and temporal overlap between the laser light and the cluster jet is carefully checked and optimized [Lamour et al., 2007] ensuring reproducible experimental conditions “shot-by-shot”, i.e. a well-defined cluster bunch interacting with every single laser shot. By spatial X-ray optimization measurements, one can estimate the cluster beam FWHM to be of the order of several mm with a rather flat cluster density profile in agreement with simulations by Boldarev et al. [2001, 2006] and measurements by Dorchies et al. [2003].

The emitted X-rays are analyzed by two semiconductor detectors and a crystal spectrometer (fig. 10.1). Taking full advantage of the “shot-by-shot” regime, X-rays are recorded in coincidence with the laser pulse which reduces dramatically the background contribution by around 4 orders of magnitude. A description of these spectrometers and of the determination of the absolute X-ray yields is given in Rozet et al. [2001] and Prigent [2004]. Briefly, one of the semiconductor detectors is used in the pile-up mode, while the other one records single-photon spectra in order to evaluate the energy of emitted photons. This method makes it possible to track the variation of absolute X-ray yields over more than 5 orders of magnitude with uncertainties ranging

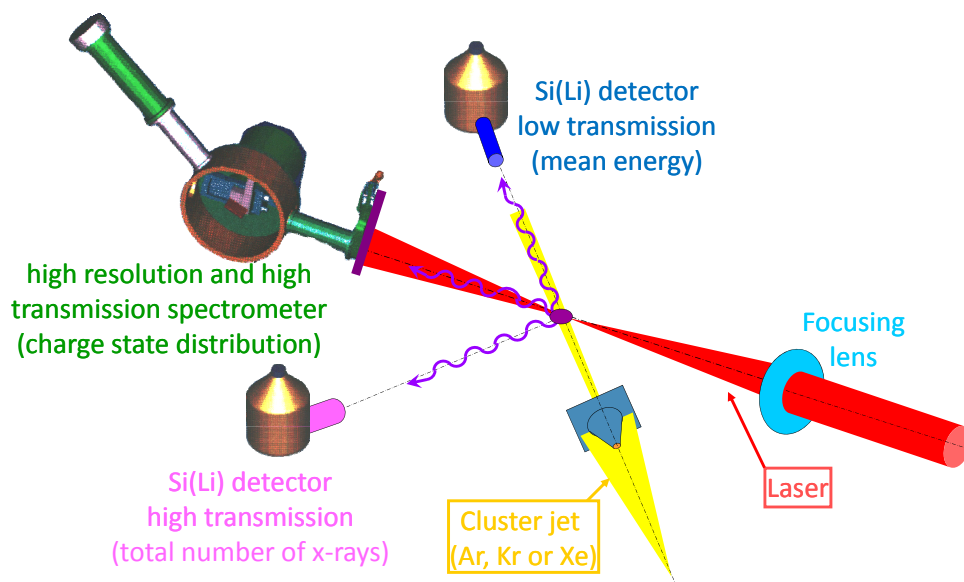


Figure 10.1: Schematic of the experimental setup [Prigent, 2004].

from 15 to 30%. State-resolved measurements are performed using a high-resolution high-transmission Bragg crystal spectrometer, equipped with a flat mosaic graphite crystal (HOPG) and a large home-made position sensitive detector working in the photon counting mode. A typical efficiency of $2 \cdot 10^{-6}$ and a resolving power of 2000 allow determining the charge state distribution of the ions emitting X-rays (i.e. ions with inner-shell vacancies). In the case of argon clusters, the changes in intensity of the characteristic K X-rays (namely $2p \rightarrow 1s$ and $3p \rightarrow 1s$ deexcitations) can be followed as a function of individual parameters (pulse duration, laser intensity, cluster size...).

Chapter 11

Extracting X-ray yields from the simulation

11.1 From inner-shell vacancies to X-rays

The X-ray yield per cluster N_X is determined by keeping track of the K-shell vacancies produced in the cluster ions by electron-impact ionization during the interaction of the laser with the cluster. For every ion with a K-shell vacancy, the appropriate fluorescence yield is determined according to its charge state at the end of the laser pulse. Figure 11.1 shows the charge state dependence of the mean fluorescence yield $\langle\omega_K\rangle^{q+}$ weighted over all electronic configurations up to the $2p$ state (i. e. all $1s2s^n2p^m$ configurations [Zou et al., 1995]).

11.2 Absolute X-ray yield

In experiments on laser-cluster interactions, the laser does not interact with a single cluster, but with a cloud of clusters. As the mean distance between the clusters is of the order of micrometers, we may neglect any interaction between the individual clusters. Furthermore, the low mean atomic density in the cluster jet prevents any propagation effects of the laser beam. One has, however, to account for the spatial intensity profile of the laser beam. For a beam propagating in z direction, the spatial intensity distribution in proximity of the focal point $(R, z) = (0, 0)$ is in good approximation given by:

$$I(R, z) = I_0 \left(\frac{w_0}{w(z)} \right)^2 \exp \left(-\frac{2R^2}{w^2(z)} \right), \quad (11.1)$$

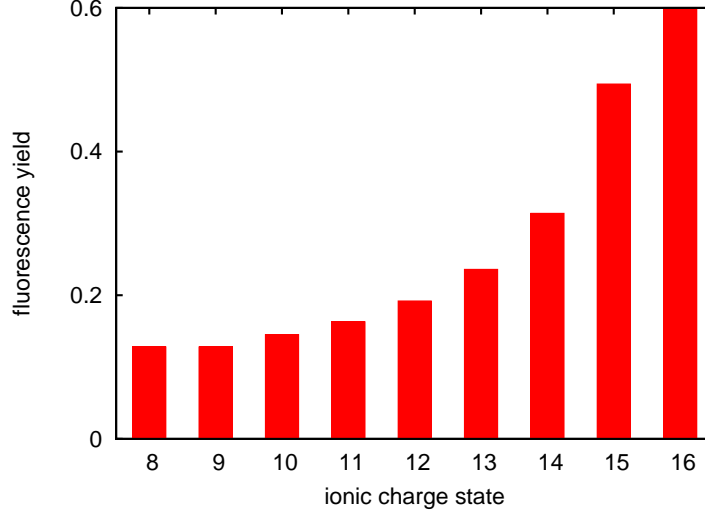


Figure 11.1: Mean fluorescence yield $\langle\omega_K\rangle^{q+}$ for different ionic charge states of argon.

where $w_0 \approx 15 \mu\text{m}$ is half the beamwaist (see fig. 11.2) and

$$w(z) = w_0 \sqrt{1 + \left(\frac{z}{z_R}\right)^2} \quad (11.2)$$

with $z_R = \pi w_0^2 / \lambda$ the Rayleigh length. The volume $V_{\text{foc}}(I, I_0)$ where the laser intensities lie between I and I_0 is given by [Posthumus, 2001]:

$$V_{\text{foc}}(I, I_0) = \frac{(\pi w_0^2)^2}{\lambda} \left\{ \frac{2}{9} \left(\frac{I_0}{I} - 1\right)^{3/2} + \frac{4}{3} \left(\frac{I_0}{I} - 1\right)^{1/2} - \frac{4}{3} \arctan \sqrt{\frac{I_0}{I} - 1} \right\} \quad (11.3)$$

As the clusters experience different laser intensities depending on their position in the experimental volume, the simulations of the single cluster have to be performed for a range of intensities I from the threshold of K-vacancy production I_{th} to the maximum intensity I_0 . This gives the intensity dependence of the X-ray emission probability per cluster atom $P_X(I) = N_X(I)/N$. We then assume within the volume $V_{\text{foc}}(I_1, I_0) - V_{\text{foc}}(I_2, I_0)$ a constant average peak intensity $I = \sqrt{I_1 I_2}$ and get the contribution of this slice of the

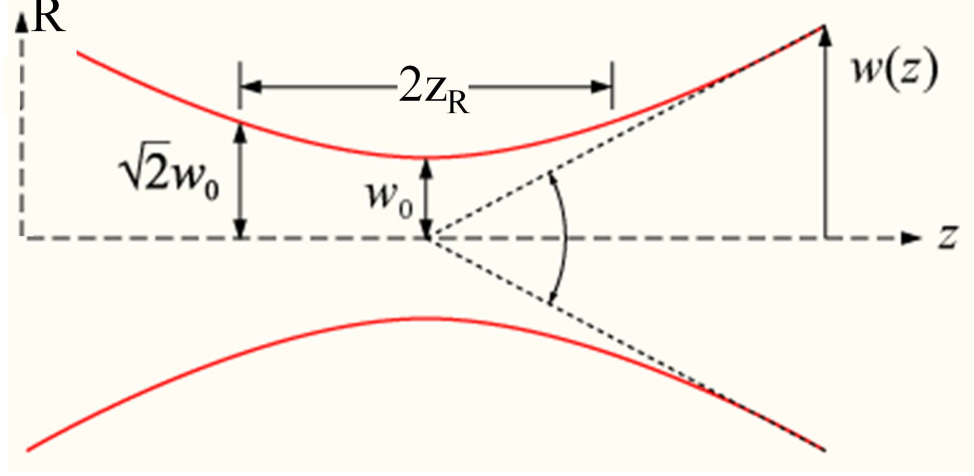


Figure 11.2: Geometry of a Gaussian beam close to focus.

interaction volume to the absolute X-ray yield:

$$Y_X(I_1, I_2) = P_X(I) n_{\text{mean}} \eta (V_{\text{foc}}(I_1, I_0) - V_{\text{foc}}(I_2, I_0)), \quad (11.4)$$

where n_{mean} is the mean atomic density of the cluster jet and η is the clustering fraction. Summing over all slices then gives the total absolute X-ray yield $Y_X(I_0)$. As the experimental η is essentially not known, it can be viewed and used as a multiplicative fit parameter between simulation and experiment.

In the subsequent chapters, we will compare our simulation results to experimental X-ray data and shed some light on the observed dependencies of the X-ray yield on parameters like laser intensity, pulse duration or cluster size.

Chapter 12

Dependence of the X-ray production on the laser intensity

12.1 Absolute X-ray yields

The absolute X-ray yields obtained in the simulation of clusters with $N = 2.8 \cdot 10^5$ atoms are compared to experimental results in figure 12.1. The yields are based on the intensity dependence of the number of K-shell vacancies produced in single clusters presented in figure 9.7. Assuming a clustering ratio of $\eta = 0.05$ gives the best fit of simulation and experimental data. The behavior of the experimental yield is well reproduced over 5 orders of magnitude by the simulation.

The presented experimental yield shows a typical intensity dependence observed throughout all studied parameter settings: a rapid onset of the X-ray yield above threshold, followed by a slower increase accurately described by a $I^{3/2}$ law. This behavior at high intensities can best be understood by introducing the effective focal volume $V_{\text{eff.foc.}}(I) = V_{\text{foc.}}(I_{th}, I)$. According to equation (11.3) this is the total volume in which the intensity threshold for X-ray production is exceeded when the peak intensity of the laser pulse is I . The effective focal volume is a measure for the number of clusters participating in the X-ray emission. For high peak intensities ($I \gg I_{th}$), $V_{\text{eff.foc.}}$ scales as $I^{3/2}$. As the X-ray yield per cluster saturates at high intensities due to cluster explosion (see fig. 9.7), the total yield then follows the intensity dependence of the effective focal volume.

The X-ray yields obtained with different settings of the cluster source (fig. 12.2) display the same qualitative behavior. However, the clustering

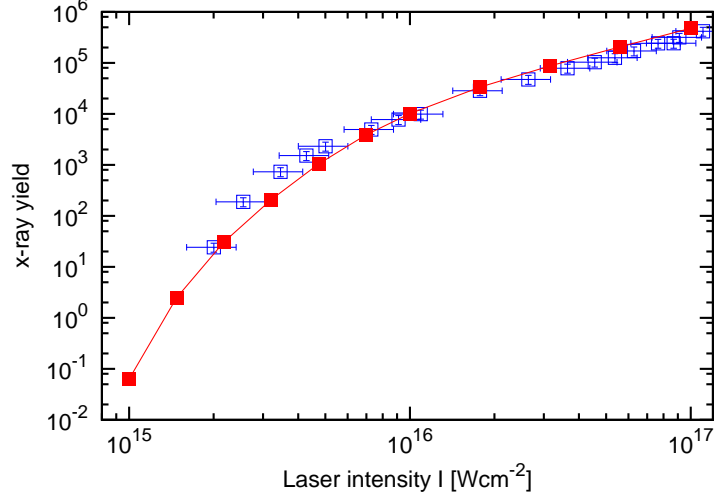


Figure 12.1: Intensity dependence of the absolute X-ray yield for $\lambda = 800$ nm, $\tau = 61$ fs and $N = 2.8 \cdot 10^5$ argon atoms per cluster. Simulation results (full symbols) and experimental data (open symbols) are compared assuming a clustering ratio of $\eta = 0.05$.

ratio extracted from the fit of the simulation data is now $\eta = 0.13$, nearly a factor 3 higher than in figure 12.1. A more efficient clustering seems indeed plausible as for these settings of the cluster source, the mean atomic density of the cluster gas $n_{\text{mean}} \sim 1.6 \cdot 10^{18}$ atoms/cm $^{-3}$ is a thousand times higher.

Very few other theoretical treatments of the laser-cluster interaction have made explicit predictions (qualitative or quantitative) for the X-ray emission. An exception is the “modified nanoplasma model” by Micheau et al. [2008] which compares results from the solution of coupled plasma equations to the X-ray experiments of Dorchies et al. [2005]. As this model describes the electrons as a Maxwellian ensemble with a unique temperature and relies on the occurrence of a nanoplasma resonance for reaching keV electron energies, it fails to predict any X-ray emission for pulses too short or too weak for the critical density to be reached during the interaction. Indeed, no X-ray production was observed from an argon cluster with $N = 4.7 \cdot 10^6$ atoms irradiated by a pulse with $\tau = 100$ fs and $I = 8 \cdot 10^{16}$ Wcm $^{-2}$ [Micheau et al., 2008].

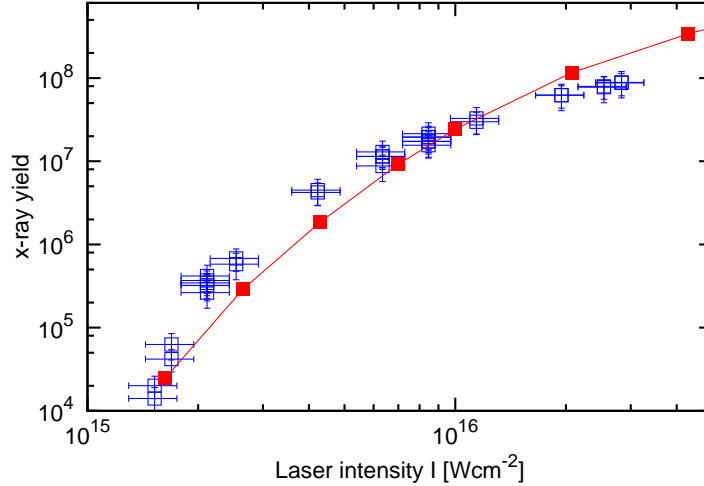


Figure 12.2: Intensity dependence of the absolute X-ray yield for $\lambda = 800$ nm, $\tau = 61$ fs and $N = 5.1 \cdot 10^5$ argon atoms per cluster. Simulation results (full symbols) and experimental data (open symbols) are compared assuming a clustering ratio of $\eta = 0.13$.

12.2 Charge state distributions

With the crystal spectrometer the energy resolution of the various $K\alpha$ lines is possible. One can thus identify the ionic charge states of the emitting cluster ions ranging from 12+ to 16+. Two typical spectra recorded by the crystal spectrometer for different laser intensities are displayed in figures 12.3b and 12.3c. The relative intensity of the different $K\alpha$ lines gives information on the L- (and M-) shell filling of the emitting argon ions and allows the evaluation of a mean X-ray energy which is related to a mean ion charge state (fig. 12.3a). A saturation of the charge state distributions towards the spectrum 12.3c has been found for laser intensities that exceed 3-4 times the threshold intensity, corresponding to a constant mean X-ray energy of 3096.6 ± 1.6 eV. In contrast, close to the threshold at $I = 2.1 \cdot 10^{15}$ Wcm $^{-2}$, even if the mean energy of the high resolution spectrum is only by 16 eV lower (3083 ± 2 eV), the charge state distribution is strongly modified (see spectrum 12.3b) as a consequence of a progressive extinction of the highest charge states.

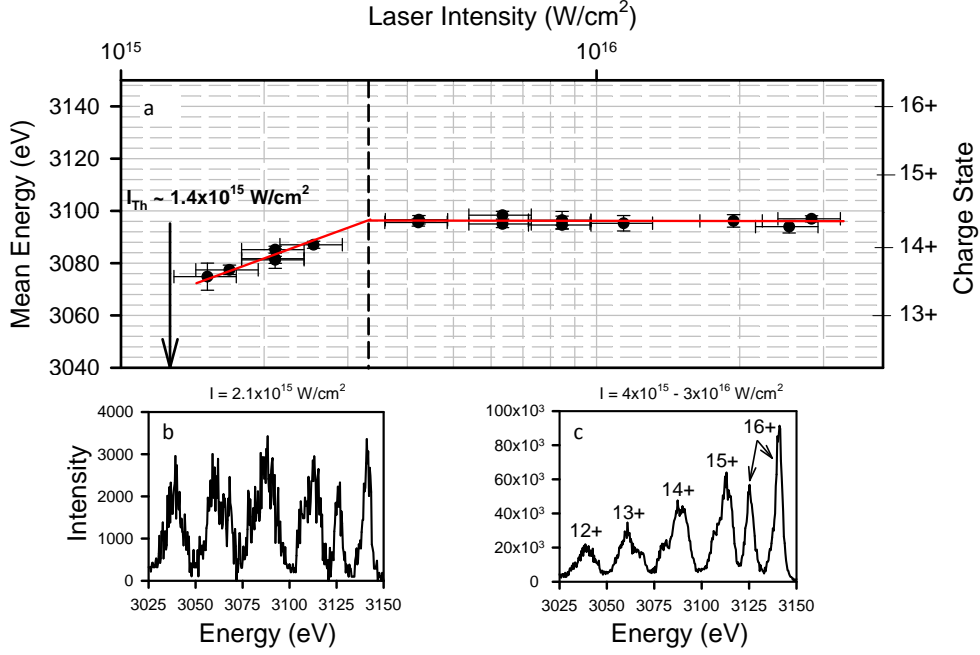


Figure 12.3: a) Laser intensity dependence of the mean energy of the $K\alpha$ transitions. Experimental spectra obtained at b) $2.1 \cdot 10^{15} \text{ Wcm}^{-2}$ and c) in the saturation regime (this spectrum was obtained by adding spectra from $4 \cdot 10^{15}$ to $3 \cdot 10^{16} \text{ Wcm}^{-2}$ for better statistics). ($\tau = 61 \text{ fs}$ and $N = 5.1 \cdot 10^5$)

For a comparison with the simulation, the charge state distributions of ions with a K-shell vacancy can be extracted from the high resolution spectra by taking into account, for each charge state, the corresponding mean fluorescence yield $\langle \omega_K \rangle^{q+}$ (fig. 11.1). The result is compared with the theoretical charge state distribution averaged over the spatial intensity profile of the laser beam (see fig. 12.4). Only cluster ions with a K-shell vacancy contribute to this distribution. The high ionic charge states and the distribution width are rather well reproduced for the high intensity regime ($I > 10^{16} \text{ Wcm}^{-2}$). The experimental and theoretical results differ nevertheless by two charge states. For lower laser intensities near the threshold, our simulation systematically underestimates the experimental mean charge state by more than 3 units, i. e. it fails to efficiently deplete the L-shell (fig. 12.5).

The origin of the discrepancies with the experimental results is not yet well understood. The main problem appears to be the lack of an efficient

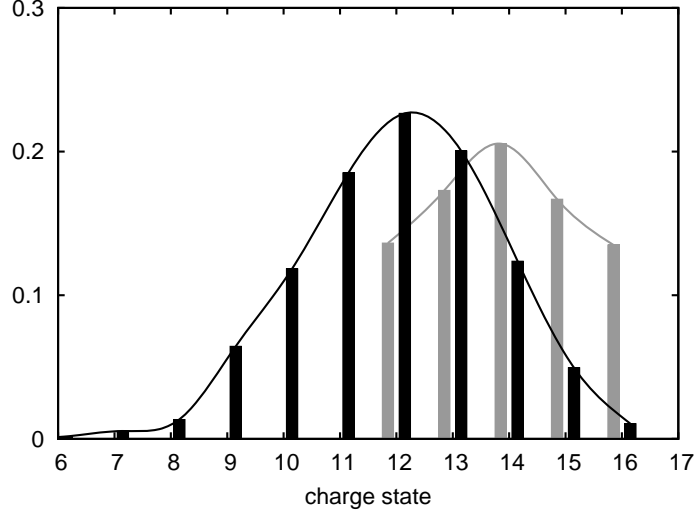


Figure 12.4: Comparison of experimental (gray) and theoretical (black) charge state distributions obtained in the high intensity regime. ($I = 6 \cdot 10^{16} \text{ Wcm}^{-2}$, $\tau = 61 \text{ fs}$ and $N = 5.1 \cdot 10^5$)

ionization mechanism for the L-shell at low laser intensities. This also affects the quality of the prediction for high intensities, as the charge state distributions are obtained by averaging over all intensities starting from the threshold. Indeed, the maximum of the distribution for a single cluster at $I = 6 \cdot 10^{16} \text{ Wcm}^{-2}$ lies at Ar^{13+} , much closer to the experimental results than the averaged results.

Other simulation methods have also failed to reproduce the experimentally observed efficient depletion of the L-shell. 3D-MPIC simulations, for example, predict charge state distributions centered around 7+ for argon clusters with $N = 40000$ atoms irradiated by intensities of $I = 3 \cdot 10^{15} \text{ Wcm}^{-2}$ [Krishnamurthy et al., 2006]. For large clusters ($N = 1.6 \cdot 10^6$) irradiated by very short ($\tau = 20 \text{ fs}$) and very intense ($I = 2.7 \cdot 10^{17} \text{ Wcm}^{-2}$) pulses, the PIC code by Fukuda et al. [2006] predicts a charge state distribution with a maximum at Ar^{9+} and a 10 times smaller fraction of Ar^{16+} produced only by field ionization in the sheath regions at the cluster poles.

A further possible source of error are the fluorescence yields and energy shifts used in the extraction of the charge state distributions from the experimental energy spectra, which rely on assumptions on the atomic configura-

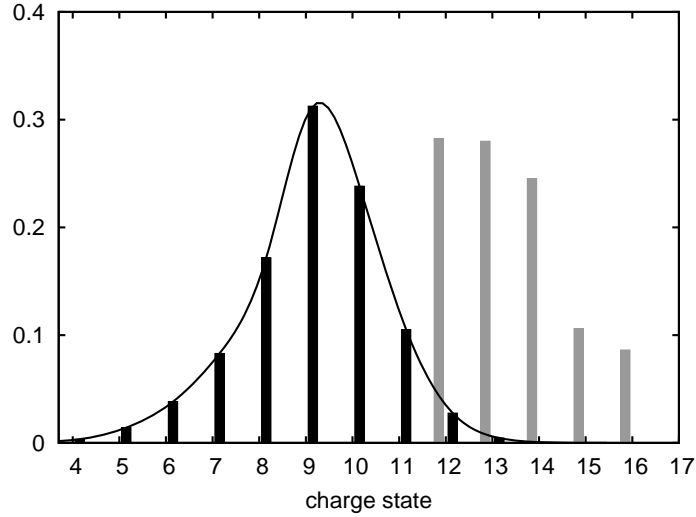


Figure 12.5: Comparison of experimental (gray) and theoretical (black) charge state distributions obtained at low intensities. ($I = 4.3 \cdot 10^{15} \text{ Wcm}^{-2}$, $\tau = 61 \text{ fs}$ and $N = 5.1 \cdot 10^5$)

tions. Especially efficient recombination to the M-shell in the dense cluster environment could lead to inaccuracies. For example, the energy of the $K\alpha$ transition in Ar^{14+} ($1s2s^22p$) is $E_K = 3080 \text{ eV}$. If recombination is efficient and 3 electrons recombine to the M-shell of that atom ($1s2s^22p3s^23p$), E_K is shifted to $E_K = 3067 \text{ eV}$ [Bhalla, 1973]. The emitted X-ray would then be counted as emitted from an Ar^{13+} (see spectra 12.3b-c), even though the ionic charge state is $q = 11$. In order to check the interpretation of the experimental spectra, a thorough analysis of the ionic configurations extracted from the simulation and a more accurate implementation of recombination are needed.

Chapter 13

Influence of the pulse duration

13.1 Absolute X-ray yields

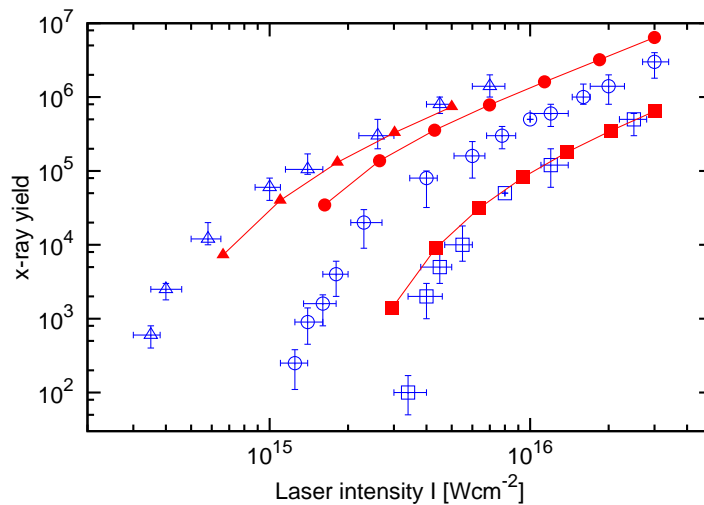


Figure 13.1: Intensity dependence of the absolute X-ray yield from argon clusters ($\langle N \rangle = 3.7 \times 10^4$ atoms) irradiated by laser pulses with durations of 56 fs (squares), 140 fs (circles) and 570 fs (triangles). Simulation results (full symbols) and experimental data (open symbols) are compared assuming a clustering ratio of $\eta = 4\%$ (due to a different cluster size and gas density, η is different from fig. 12.1 or fig. 12.2).

Since K-shell vacancy production sets in as soon as the cluster is sufficiently charged to allow electrons to be heated beyond $E_K = 3.2 \text{ keV}$, one can expect a lowering of the threshold for X-ray production when more time is allocated for cluster charging by increasing the pulse duration. This decrease of the intensity threshold can be clearly observed both experimentally and theoretically (fig. 13.1). In the experiments, the threshold drops from $I_{th} = 2.9 \cdot 10^{15} \text{ Wcm}^{-2}$ for a pulse duration of $\tau = 56 \text{ fs}$ to $I_{th} = 2.8 \cdot 10^{14} \text{ Wcm}^{-2}$ for $\tau = 570 \text{ fs}$. The latter corresponds to a threshold reduction by a factor 10 and is close to the intensity $I_{OBI}[\text{Ar}] = 2.2 \cdot 10^{14} \text{ Wcm}^{-2}$ necessary to produce the first quasi-free electrons by over-barrier ionization of the argon atom. The simulation results correspond well with the experiments for the shortest and the longest pulses. The yields at $\tau = 140 \text{ fs}$ are however strongly overestimated by the simulation. This is due to the fact that the simulation predicts a significantly lower intensity threshold for X-ray production at that pulse length. The wrong position of the threshold leads to an increased X-ray yield for all laser peak intensities as, due to the larger effective focal volume, more clusters partake in the X-ray emission.

A possible explanation for the bad fit between experiment and simulations at intermediate pulse durations may be errors in the speed of the ion expansion velocities which could cause increasingly inaccurate estimates for the electron acceleration and K-shell vacancy production for long pulse durations. The present simulation technique can not resolve the interaction potential between electrons and ions on a length scale smaller than the cell size which is of the order of 0.5 nm (or 10 a.u.). While this limitation does not affect collisional interactions which are accounted for by the stochastic event-by-event sampling, it influences the mean ion-electron and thus mean ion-ion interaction responsible for cluster expansion. The shielding of forces acting on an ion surrounded by (slow) quasi-free electrons is therefore not fully included in our simulation.

13.2 Effect of ion shielding

Up to now we ignored the possible shielding of the ions and propagated the ions in the mean field according to their bare ionic charge $q_j(t)$. In order to estimate the size of possible errors made by this approach and the effect on K-vacancy production, we compare in the following this fully unshielded case to the opposite limiting case of full shielding. For this case we assume that all surrounding electrons contribute to the shielding of an ion. We propagate the ion in the mean field according to an effective ionic charge which is the bare ionic charge reduced by the local number of quasi-free electrons per ion

(in atomic units):

$$q_j^{(\text{eff})}(t) = q_j(t) - \frac{n^{(e)}(\mathbf{r}_j^{(i)}, t)}{n^{(i)}(\mathbf{r}_j^{(i)}, t)}. \quad (13.1)$$

In the shielded case, the ion-ion repulsion is underestimated and the Coulomb explosion is delayed. In the unshielded case, the cluster expansion is likely to be overestimated.

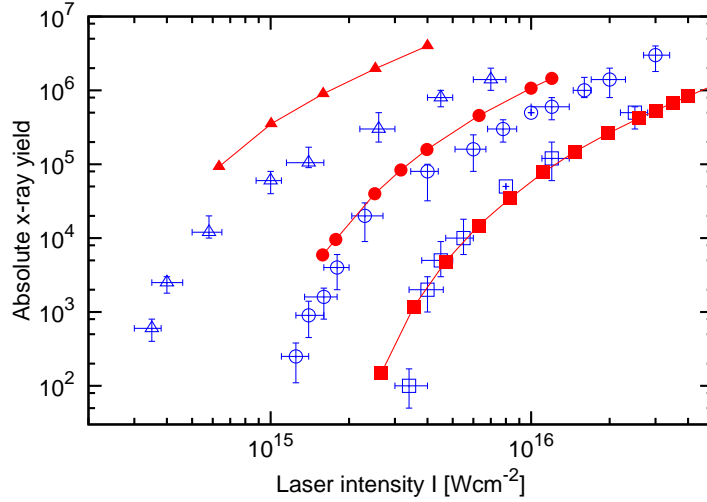


Figure 13.2: Intensity dependence of the absolute X-ray yield from argon clusters ($\langle N \rangle = 3.7 \times 10^4$ atoms) irradiated by laser pulses with durations of 56 fs (squares), 140 fs (circles) and 570 fs (triangles). A clustering ratio of 4% is assumed. The simulation results were obtained with shielded ion dynamics.

Figure 13.2 displays the absolute X-ray yield obtained with the shielded ion dynamics and can directly be compared to the data obtained without shielding (fig. 13.1). For relatively short pulses ($\tau = 56$ fs) during which only the onset of expansion occurs, the evolution of the K-shell ionization probability per atom is not very sensitive to the assumptions about the effective shielding. For the very long pulse of $\tau = 570$ fs the shielded results lie considerably above the unshielded ones and the experiment. The slowed ion dynamics and delayed cluster explosion provide too much time for electron heating and K-vacancy production. For intermediate pulses ($\tau = 140$ fs),

the decision whether the shielded or unshielded model gives better results is more involved. For low laser intensities, inclusion of shielding leads to higher threshold intensities I_{th} , closer to the experiment than without shielding. As the expansion of the cluster is delayed compared to the unshielded case, the sheath regions at the cluster poles develop later in the pulse, providing less time for efficient electron heating. For higher laser intensities, however, the slower ion dynamics lead to an ongoing heating and the K-vacancy production per cluster is not effectively quenched by cluster disintegration. The simulation with shielding consequently deviates from the experimental results, overestimating more and more the observed X-ray yield when increasing the intensity. In this regime, the saturation of the vacancy production as predicted by the unshielded model would provide better results. This conforms with the intuitive picture that in strong laser fields the more energetic (“hotter”) electrons are less influenced by the ionic potentials and shield the ions less efficiently, justifying the unshielded model. For weaker laser intensities, i. e. close to the threshold, stronger electron-ion correlation persists, which would favor a shielded model.

This situation suggests the need for a shielding description that takes the kinetic energy of the free electrons in the cell into account. One approach would be a Debye-Hückel type model [Debye and Hückel, 1923; Morawetz, 2000], where the effective ionic charge is assumed to be of the form:

$$q_j^{(\text{eff})} = q_j \exp\left(-\frac{q_j}{T\lambda_D}\right), \quad (13.2)$$

with q_j the bare ionic charge, T the local electron temperature and λ_D the local Debye length. The subsequent reduction of the electric force can be seen as the effect of the deformed screening cloud surrounding the ion. We included the effective charge (13.2) in the simulation by estimating in every mesh cell the temperature from the mean electron energy as $T = 2/3\langle E \rangle$. For intensities near the threshold, typical values are $T \lesssim 5$ a.u. and $\lambda_D \sim 3$ a.u.. The results were however very close to the unshielded case, the yields for $\tau = 140$ fs being only 20% lower than the unshielded case and still a factor 3 above the experiment. The correct description of shielding thus remains an open question.

13.3 Charge state distributions

The influence of the expansion dynamics not only manifests in the X-ray production controlled by the fast electron population, but also in the evolution of the ionic charge state distributions (ionization of M- and L-shell), which

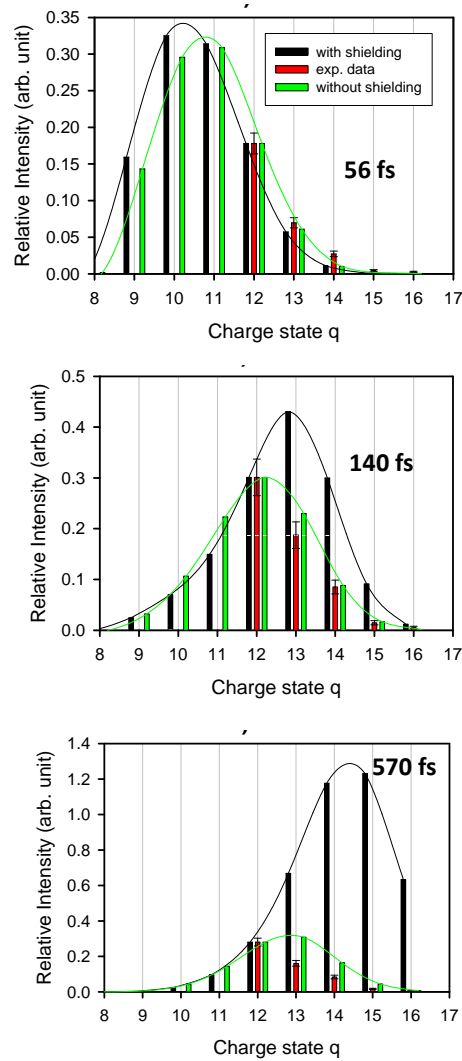


Figure 13.3: Comparison between experimental and theoretical charge state distributions for different pulse durations in clusters with $N = 3.7 \cdot 10^4$ atoms. Top: $\tau = 56$ fs, $I = 4 \cdot 10^{16} \text{ Wcm}^{-2}$. Center: $\tau = 140$ fs, $I = 1.6 \cdot 10^{16} \text{ Wcm}^{-2}$. Bottom: $\tau = 570$ fs, $I = 4 \cdot 10^{15} \text{ Wcm}^{-2}$. Black bars: simulation with shielding, green bars: simulation without shielding (full lines to guide the eye), red bars: experimental data. All data are normalized to the lowest experimentally observed charge state (12+).

are governed by the global electron population. The experimental charge-state distributions have been measured in the saturation region of high laser intensities for three different laser pulse durations (fig. 13.3). In comparison to fig. 12.4, the charge state distributions are centered at lower charges for these considerably smaller clusters with nearly ten times less atoms. The theoretical charge-state distributions are obtained by averaging the results from single clusters over the effective focal volume (i. e. from I_{th} to I). The experimental distributions are best reproduced by the simulation neglecting the ionic shielding, which reproduces well the slight shift towards higher charge states as the pulses grow longer. With shielding included, however, the resulting charge states for the longest pulses are far too high, which reflects the ongoing heating due to the slower explosion of the cluster. This again points to the validity of the unshielded model at high laser intensities.

13.4 Evolution of the X-ray yield at constant laser energy

Since the K X-ray emission is influenced by both the laser peak intensity I and the pulse duration τ , systematic investigations of the dependence on τ require the simultaneous control of the intensity. One possibility is to keep the laser energy, $E \propto (I \cdot \tau)$, constant at values such that the intensity threshold $I_{th}(\tau)$ is exceeded for all studied pulse durations.

Experimentally, an optimal laser pulse duration for the X-ray emission has been observed for large argon clusters with N between $5.1 \cdot 10^5$ and $1.8 \cdot 10^6$ atoms irradiated by laser pulses of constant energy $E = 20$ mJ (fig. 13.4). After a clear increase by more than a factor 2 between 50 and 140 fs, the X-ray yield decreases from 140 to 800 fs. The presence of an optimal pulse duration and its dependence on the cluster size has often been used as an indication for the appearance of a nanoplasma resonance [Ditmire et al., 1996; Micheau et al., 2008]. However, in the size range studied here, one does not observe any significant shift of the optimum pulse duration when varying the cluster size, which suggests another origin of the observed pulse length dependence. The nanoplasma model in Micheau et al. [2008] predicts furthermore a much longer optimal pulse duration of approximately 400 fs for very similar parameters ($N = 4.7 \cdot 10^6$ and a laser energy corresponding to 30 mJ in the experimental setup of fig. 13.4).

Due to the spatial laser intensity profile, the X-rays are produced by an ensemble of clusters subjected to laser intensities from $I_{th}(\tau)$ to $I(\tau)$. As discussed in the previous sections, our simulation does not incorporate ion

13.4. EVOLUTION OF THE X-RAY YIELD AT CONSTANT LASER ENERGY 85

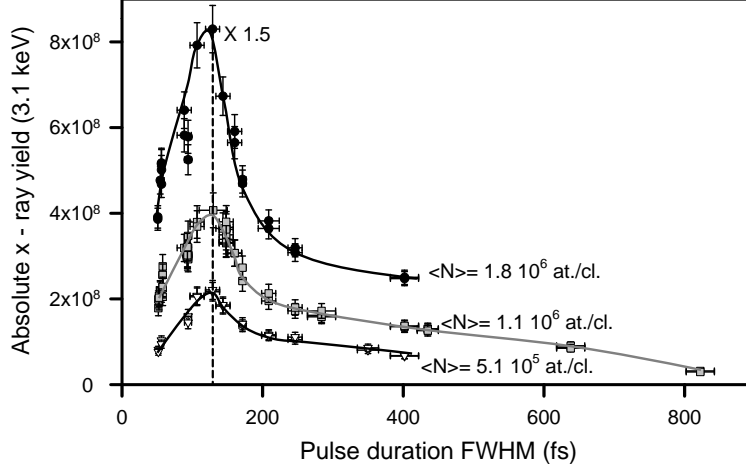


Figure 13.4: Evolution of the measured absolute X-ray yield with the pulse duration at a constant energy per pulse of $E = 20$ mJ for different cluster sizes N . Bottom to top: $5.1 \cdot 10^5$, $1.1 \cdot 10^6$ and $1.8 \cdot 10^6$ atoms per cluster. For the sake of clarity, experimental data for $N = 1.8 \cdot 10^6$ are multiplied by 1.5 (lines to guide the eye).

shielding correctly, which results in inaccuracies when going to long pulse durations. We can nevertheless make qualitative predictions for the dependence of the total X-ray yield $Y_X(\tau)$ on the laser pulse duration by using results from both the model with shielding and the model without shielding. The model without ion shielding predicts too low intensity thresholds and therefore largely overestimates the number of emitting clusters for long pulse durations. More accurate results for the intensity threshold $I_{th}(\tau)$, which we define as the intensity for which only one K-shell vacancy is produced in the cluster ($P_K(I_{th}) = 1/N$), are expected from the model with full ion shielding. This model, however, does not reproduce the saturation of the vacancy production in a single cluster due to cluster disintegration at high laser intensities. We therefore employ the model without shielding to predict the number $P_K(I(\tau))$ of K-shell vacancies produced per cluster atom in a single cluster at the high intensities in the laser focus.

P_K is found to grow with increasing pulse lengths before saturating due to cluster disintegration (fig. 13.5a). The effective focal volume $V_{\text{eff.foc.}}(I_{th}(\tau), I(\tau))$, on the other hand, shrinks with increasing pulse lengths (fig. 13.5b). We now

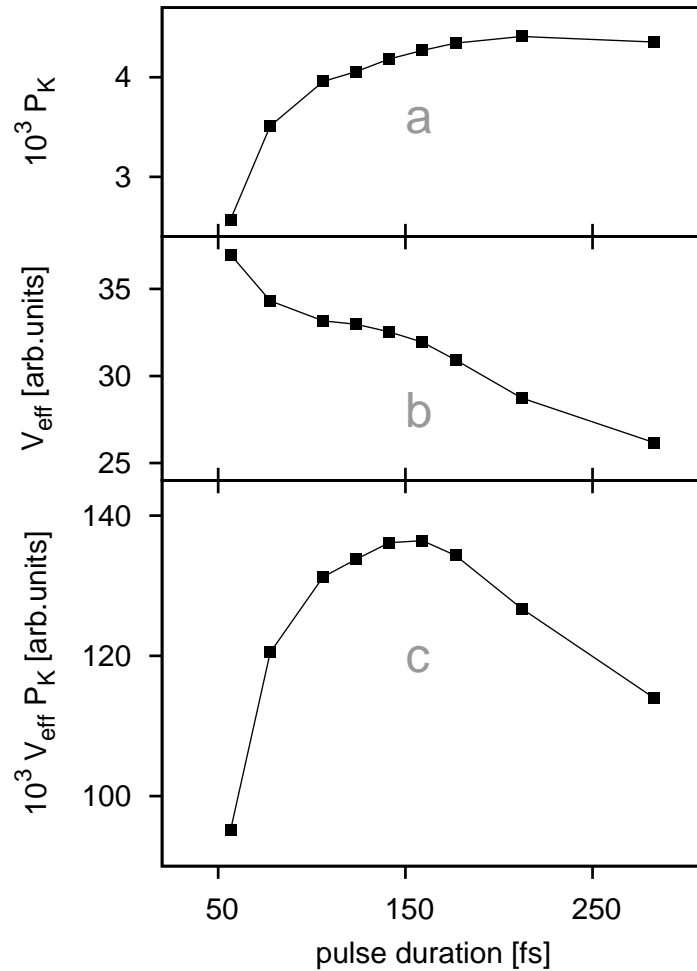


Figure 13.5: Simulation of the τ dependence of X-ray yields $Y_X(\tau)$ at fixed total laser energy $E = 20$ mJ for argon clusters with $N = 5.1 \cdot 10^5$ atoms. a) number of K-shell vacancies per cluster atom calculated without shielding, b) effective focal volume deduced from the threshold intensities calculated with shielding, and c) estimate of the total X-ray yield Y_X by taking the product of a) and b).

estimate the total X-ray yield as the product $P_K(\tau) \cdot V_{\text{eff.foc.}}(\tau)$, neglecting the intensity dependence at constant τ of the X-ray production probability. In the evolution of $P_K(\tau) \cdot V_{\text{eff.foc.}}(\tau)$ the increase of the vacancy production per cluster counteracts the decrease of the number of participating clusters. As a result of this competition, the total X-ray yield goes through a maximum at the optimal laser pulse duration $\tau_{\text{max}} \sim 140$ fs (fig. 13.5c). This result is very close to the optimal pulse duration of ~ 140 fs observed experimentally.

The key to this theoretical prediction of the optimal pulse duration is the combination of the two extreme shielding models, applying one at low laser intensities and the other at high intensities. When sticking to a single model and calculating the yields for increasing pulse durations, one fails to reproduce the experimentally observed maximum. In the case of full shielding, the slow cluster disintegration leads to an ongoing increase of the X-ray yield till far beyond $\tau \sim 300$ fs. Without any shielding, the total yield increases first very steeply until $\tau \sim 100$ fs because of the fast drop of the intensity threshold, and then saturates, showing no pronounced maximum. Again, a more complete treatment of the ion shielding would be needed for a quantitative prediction of the evolution of the X-ray yield with the pulse duration. Nevertheless, we can conclude, that under the present conditions, no resonance effect is needed to explain the appearance of an optimum pulse duration and that the competition between the number of emitting clusters and the number of emitted X-rays per cluster seems to be the appropriate explanation for the observed pulse length dependence.

13.5 Evolution of the X-ray yield at constant laser intensity

An alternative approach to quantifying the X-ray yield as a function of the pulse duration is keeping the laser peak intensity constant, which implies increasing pulse energies for longer pulses. After an initial strong increase by more than one order of magnitude in the X-ray yield between 55 fs and 140 fs (fig. 13.6), one experimentally observes a slow saturation for longer pulse durations. These results can again be understood when considering that the X-ray yield $Y_X(\tau)$ is governed by both the effective focal volume and the probability for K-shell vacancy production in a single cluster. P_K at constant laser intensity increases with increasing pulse durations, saturating for long pulses due to cluster disintegration (see fig. 9.6). As I_{peak} is fixed, $V_{\text{eff.foc.}}(\tau)$ is governed by $I_{\text{th}}(\tau)$ alone. The drop in the threshold intensity for longer pulses (see fig. 13.1) results in an increasing $V_{\text{eff.foc.}}(\tau)$. For very long pulses

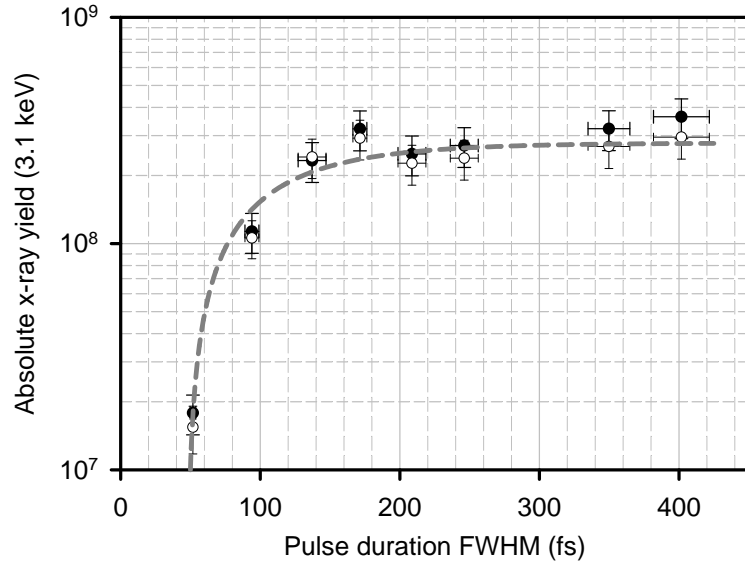


Figure 13.6: Evolution of the absolute X-ray yield with the pulse duration at a constant laser intensity of $I = 8 \cdot 10^{15} \text{ Wcm}^{-2}$ for a cluster size $N = 1.1 \cdot 10^6$ (full circle: data from the high resolution crystal spectrometer, open circle: data from semi - conductor detector, dashed line to guide the eye).

the intensity threshold reaches its minimum value close to 10^{14} Wcm^{-2} and $V_{\text{eff.foc.}}(\tau)$ no longer changes. At constant laser peak intensity both $V_{\text{eff.foc.}}(\tau)$ and $P_K(\tau)$ initially increase and then saturate when going to longer pulse durations. Therefore, the absolute X-ray yield, given by the product $P_K \cdot V_{\text{eff.foc.}}$, displays the same trend.

Chapter 14

Influence of the cluster size

After examining in the last chapters the influence on the X-ray production of laser pulse parameters such as intensity and pulse duration, we now turn to the influence of the cluster size on the X-ray yields. From the experimental point of view, the cluster size is controlled by the backing pressure P_0 with which the argon gas is pushed through the nozzle. The mean cluster size is predicted to scale like $\langle N \rangle \propto P_0^{1.8}$ [Prigent, 2004]. At the same time the mean atomic density of the cluster jet is directly proportional to P_0 . When calculating absolute X-ray yields from single cluster results, one therefore has to take into account the correlation between the cluster size N and the density of clusters in the experimental volume. The density of clusters scales approximately like $N^{-0.45}$. We found no experimental or theoretical predictions for the influence of the backing pressure P_0 on the clustering efficiency η . Intuitively, one could suspect that, at constant temperature of the nozzle, a higher gas density in the cluster jet would favor clustering and thus increase η .

The intensity dependence of the absolute X-ray yields for different cluster sizes ranging from $N = 6.7 \cdot 10^3$ to $N = 5.1 \cdot 10^5$ reveals a decrease of the intensity threshold for X-ray production with increasing cluster size (fig. 14.1). This is consistent with the reasoning of section 8.2 which linked the threshold for K-shell vacancy production to the charging of the cluster via the electric potential at the center of the cluster $\phi(\mathbf{r} = 0, t) \approx E_K$. One can assume that the potential is linked to the cluster charge $Q(t)$ as $\phi(\mathbf{r} = 0) \sim Q/R_{cl}$. The cluster charge is determined by the number of electrons leaving the cluster and should therefore increase with increasing cluster surface ($Q \sim R_{cl}^2$). $\phi(\mathbf{r} = 0, t)$, and thus the maximum electron energy, therefore scale approximately as R_{cl} (see fig. 14.2). This indeed implies a decrease of the threshold for K-vacancy production with increasing cluster size. In order to deduce from these relationships a scaling law for the threshold intensity, one needs

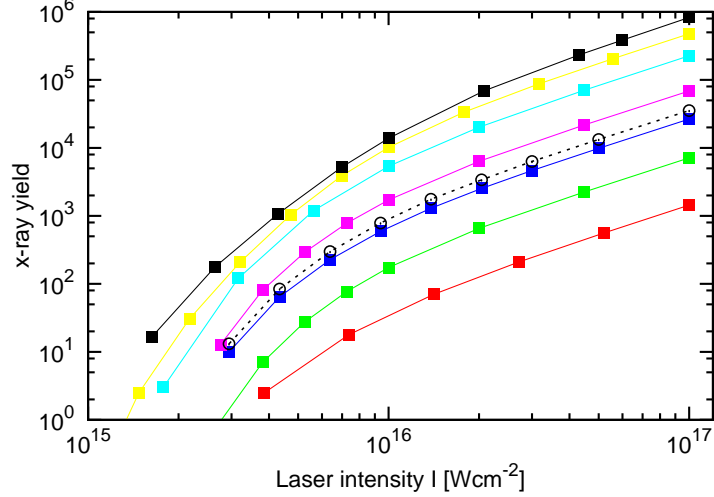


Figure 14.1: Full lines and squares: intensity dependence of the absolute X-ray yield for different cluster sizes. From bottom to top: $N = 6.7 \cdot 10^3$, $N = 1.6 \cdot 10^4$, $N = 3.7 \cdot 10^4$, $N = 7.4 \cdot 10^4$, $N = 1.7 \cdot 10^5$, $N = 2.8 \cdot 10^5$ and $N = 5.1 \cdot 10^5$. The cluster density varies according to $N^{-0.45}$ (see text). Dashed line and circles: absolute X-ray yield from clusters with a size distribution $f(N)$ with $\langle N \rangle = 3.7 \cdot 10^4$. A constant clustering ratio of $\eta = 0.05$ was assumed for all sizes. ($\tau = 56$ fs).

to know how the maximum value of the maximum kinetic energy scales both with cluster size and laser intensity. Unfortunately, it is already apparent in figure 14.2, that the maximum value of $\phi(\mathbf{r} = 0, t)$ does not follow reliably the R_{cl} scaling. This is due to the fact, that the decrease of $\phi(\mathbf{r} = 0, t)$ in the second half of the time evolution is linked to the cluster expansion, that counteracts the increase in $Q(t)$. We were not able to determine a simple scaling relation between the position of the maximum and the cluster size or laser intensity. We can therefore make only the qualitative statement, that the threshold intensity decreases with an increasing cluster size, but no quantitative prediction on the scaling.

The present simulation results also allow to investigate the possible influence of the distribution of cluster sizes inside the jet on the absolute X-ray yield. Assuming the log-normal size distribution (10.1) with $\langle N \rangle = 3.7 \cdot 10^4$, one obtains yields approximately 30% higher than the yields generated only

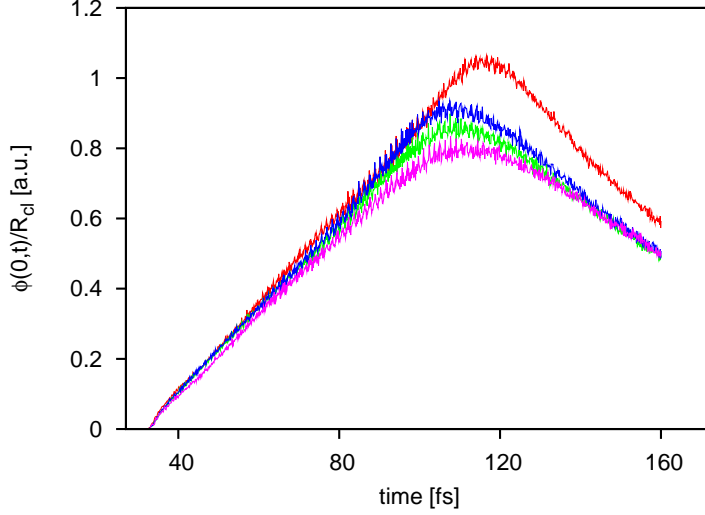


Figure 14.2: Time dependence of $\phi(\mathbf{r} = 0, t)/R_{cl}$ for clusters of different sizes irradiated by a pulse with $I = 2 \cdot 10^{15} \text{ Wcm}^{-2}$ and $\tau = 56 \text{ fs}$. The cluster sizes are $N = 3.7 \cdot 10^4$ (red), $N = 6 \cdot 10^4$ (blue), $N = 7.4 \cdot 10^4$ (green) and $N = 1.1 \cdot 10^5$ (magenta).

from clusters with $N = 3.7 \cdot 10^4$ (see dashed line and circles in fig. 14.1). As this effect is not very strong (especially compared with uncertainties in the clustering ratio η), and information on size distributions in cluster jets is extremely sparse, all other simulation data in this thesis were generated assuming a single size N for all clusters in the interaction region.

The cluster size also influences the ionization of the M- and L-shells of the cluster ions. The ionic charge state distributions in figure 14.3 are taken of ions with K-shell vacancies and evaluated by averaging over the entire effective focal volume for a peak laser intensity of $I = 1 \cdot 10^{17} \text{ Wcm}^{-2}$. A clear shift to higher charge states is observed when enlarging the cluster. The effective electric field inside the cluster, and thus the mean electron energy, is in good approximation only dependent on the electron density inside the cluster, and not directly influenced by the cluster size (see eq. (6.3)). The additional ionization of the cluster ions in a larger cluster is therefore to be traced to the longer life time of the cluster before disintegration. The shift to higher charge states for larger cluster has also been observed experimentally by high resolution X-ray spectroscopy [Lamour et al., 2007; Prigent, 2004].

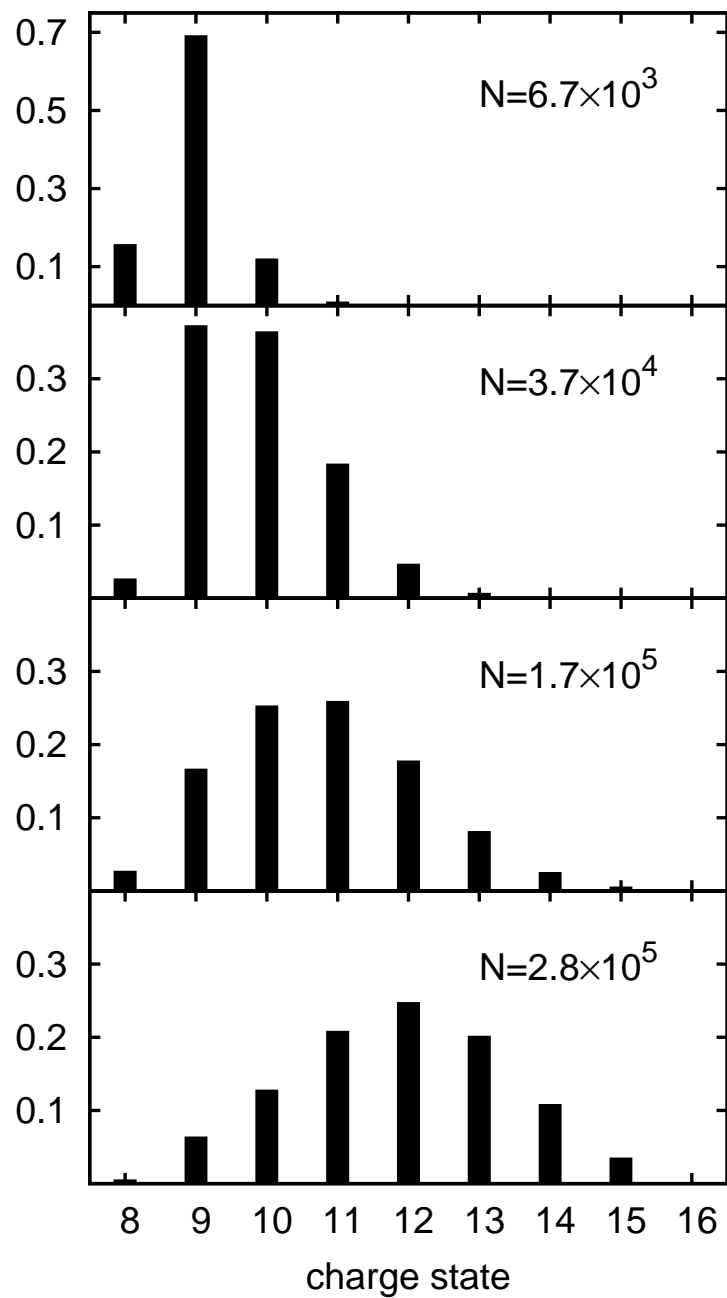


Figure 14.3: Simulated ionic charge state distribution for different cluster sizes. ($I = 1 \cdot 10^{17} \text{ Wcm}^{-2}$, $\tau = 56 \text{ fs}$).

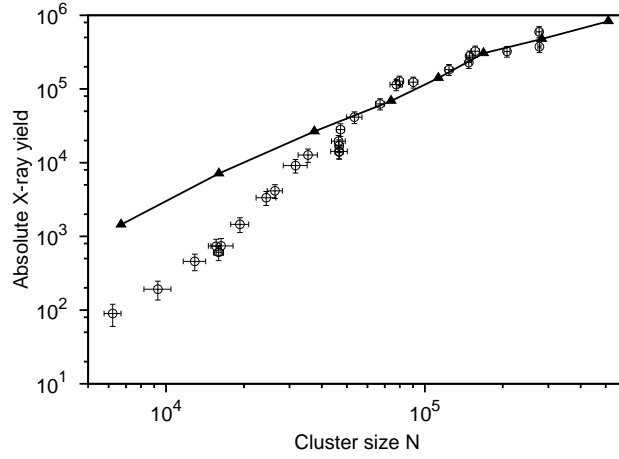


Figure 14.4: Cluster size dependence of the absolute X-ray yield. Simulation results (triangles) and experimental data (circles with error bars) are compared. A size-independent clustering ratio of $\eta = 0.05$ was assumed for the simulation data. ($I = 1 \cdot 10^{17} \text{ Wcm}^{-2}$, $\tau = 56 \text{ fs}$).

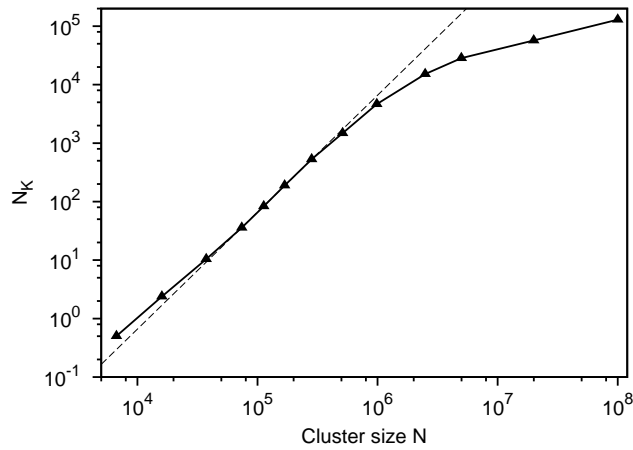


Figure 14.5: Cluster size dependence of the total number of K-shell vacancies produced in a single cluster. The dashed line marks a quadratic size dependence (or a scaling with R^6). ($I = 1 \cdot 10^{17} \text{ Wcm}^{-2}$, $\tau = 56 \text{ fs}$).

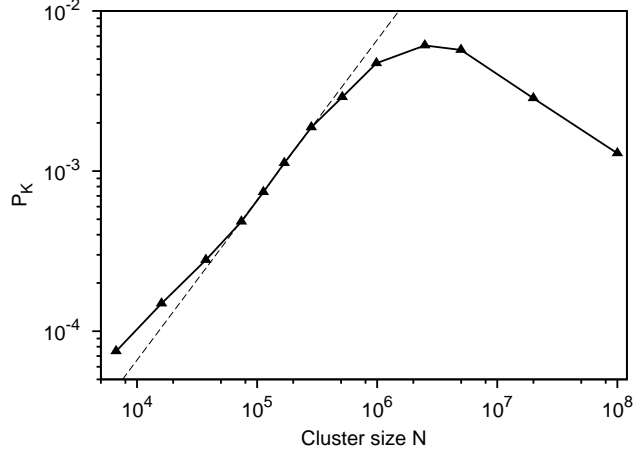


Figure 14.6: Cluster size dependence of the number of K-shell vacancies produced per atom in a single cluster. The dashed line marks a linear size dependence (or a scaling with R^3). ($I = 1 \cdot 10^{17} \text{ Wcm}^{-2}$, $\tau = 56 \text{ fs}$).

Experiments on the cluster size dependence of the X-ray yield were performed at a laser intensity of $I = 10^{17} \text{ Wcm}^{-2}$ (fig. 14.4). The comparison with the yields extracted from the simulation reveal a strong discrepancy for small clusters. This could hint at a dependence of the clustering ratio η on the backing pressure P_0 used in the experiments to control the cluster size. In figures 14.1 and 14.4 we assumed the constant clustering ratio of $\eta = 0.05$, that we used in fig. 12.1 for a fit of the absolute yield from clusters with $N = 2.8 \cdot 10^5$ to experimental results. The strong overestimate of the experimental results by the simulation for small clusters would point to less efficient clustering (smaller η) for lower mean atomic densities. In principle this comparison of experimental and theoretical could be used to extract the dependence $\eta(P_0)$. However, the relation would only be applicable for this particular experimental setup. Changing, for example, the position of the laser focus within the cluster jet could already result in a different η for the same backing pressure, as the local properties of the flowing gas may be different. For a physical insight into the clustering efficiency, a detailed study of the gas flow dynamics therefore seems necessary.

We conclude the investigation of the cluster size dependency with the examination of the number N_K of K-shell vacancies produced per atom in a single cluster irradiated by a pulse with $I = 10^{17} \text{ Wcm}^{-2}$ (fig. 14.5). Over two

orders of magnitude in the cluster size corresponding to the sizes used in the X-ray spectroscopy experiments, N_K scales approximately as N^2 (or as R_{cl}^6), which implies that the number of K-shell vacancies produced per atom P_K increases linearly with N (see fig. 14.6). The size dependence of the number of produced K-shell vacancies is mainly controlled by the number of electrons heated in the sheath regions at the cluster poles. As the electrons to be heated drift out of the cluster during the collapse of the sheath, their total number is expected to scale like R_{cl}^2 . The cluster cross-section scales also as R_{cl}^2 . The scaling $N_K \propto R_{cl}^4$ is indeed observed early on during the laser pulse as the clusters are not yet significantly expanded. The transition from R_{cl}^4 to the R_{cl}^6 dependency of the final number of produced vacancies is not completely clear. Several factors are expected to contribute, such as the lifetime of the cluster (which is found to scale approximately as $\sqrt{R_{cl}}$) or the slightly stronger monopole and dipole fields in the sheath regions of larger clusters. For very large clusters ($N \gtrsim 10^6$) our simulation predicts a slow saturation of the total number of X-rays produced per cluster (fig. 14.5). This implies the existence of an optimal cluster size around $N \simeq 2 \cdot 10^6$ where the number P_K of vacancies per cluster atom is maximized (fig. 14.6). This observation is in contradiction with results from the nanoplasma model which predict a clear maximum in the *total* number of X-rays produced in a single cluster at a size of $N \simeq 7 \cdot 10^6$ [Micheau et al., 2008]. This maximum is caused by the fact that large clusters do not expand fast enough to reach the critical density and thus the nanoplasma resonance during the laser pulse. Our observation of a saturation, rather than a maximum in N_K is yet another indicator that the X-ray production is not dominantly driven by a nanoplasma resonance, as we still observe vacancy production for clusters so large they practically don't expand during the laser pulse.

Chapter 15

Conclusion and Outlook

The aim of this thesis was to elucidate the mechanisms at play during the interaction of intense femtosecond laser pulses with large rare-gas clusters. Particular emphasis was put on the understanding of the fast electron dynamics which are driving the experimentally accessible X-ray emission.

We have developed a Classical Trajectory Monte Carlo simulation with a mean field approach. At each time step, the electric field is evaluated from the charge distribution by solving the Poisson equation on a mesh. Elastic electron-ion scattering, electron-electron scattering, electron-impact ionization and excitation, as well as three-body recombination and Auger decay are included via stochastic events.

The simple picture of a polarizable sphere remains a good first approach to understand the screening of the laser field inside the cluster and the enhancement of the field at the cluster poles due to the periodic displacement of the high density electron cloud. In addition to this dipole contribution to the mean field, the charging of the cluster gives rise to a monopole term. Their combination produces a strong asymmetry in the field: at one cluster pole a highly charged sheath region forms where the laser field is strongly enhanced. At the opposite pole the displaced electron cloud compensates the ionic background and the total field is very small. During the subsequent laser half-cycle, the sheath collapses at the one cluster pole and builds up at the opposite one, thus inverting the situation at the poles.

The efficient shielding of the laser field inside the cluster causes the vast majority of the cluster electrons to have kinetic energies well below the ponderomotive energy of the laser. However, the high energy tail of the kinetic energy distribution deviates strongly from the overall Maxwellian distribution, and reveals the presence of a subensemble of very fast electrons with specific dynamics [Deiss and Burgdörfer, 2007]. The sheath regions at the cluster poles are the key to understanding the heating mechanism behind

the high energy electrons. A small fraction of the slow electrons can leave the cluster at the pole with the collapsed sheath. These electrons are then strongly accelerated back into the cluster as the sheath builds up again during the subsequent laser half-cycle. The maximum kinetic energy an electron can gain by this mechanism is mainly controlled by the charging of the cluster [Prigent et al., 2008]. As the accelerated electrons transit the cluster at high velocity, wake fields oscillating at plasma frequency inside the cluster can be clearly observed in the simulation.

As some electrons reach keV energies, inner-shell vacancies are created by electron-impact ionization of the cluster ions. The decay of these vacancies is at the origin of X-ray photons, which are accessible in X-ray spectroscopy experiments. X-rays are produced as soon as the laser pulse is either strong or its duration long enough for a sufficient charging of the cluster to allow the electron energies to reach the binding energy of the inner-shells. This dependence of the X-ray production on intensity and pulse duration explains the experimentally observed intensity threshold for X-ray production, which is lowered when the pulse duration is increased.

The timing of the cluster disintegration relative to the laser pulse determines the dependence of the number of vacancies produced in one cluster on the pulse intensity or duration. For short and/or weak pulses, the pulse is over and the X-ray production stops before the disintegration of the cluster. Increasing the intensity or the duration of the pulse allocates more time for the electron heating and leads to a strong increase in the number of produced inner-shell vacancies. For longer and/or more intense pulses, the cluster disintegrates before the end of the laser pulse which limits the vacancy production. At this point the X-ray production in the single cluster saturates, and eventually even slightly decreases as the disintegration occurs before the field maximum.

By averaging over the spatial intensity distribution of the laser pulse, we extract total X-ray yields from our simulations, which can be quantitatively compared to the experimental results. The only fit parameter we use is the unknown clustering efficiency of the cluster source. For short laser pulses ($\tau \simeq 60$ fs) the measured intensity dependence of the X-ray yields is very well reproduced by our simulation. For longer pulses ($\tau \gtrsim 100$ fs) our model fails to reproduce the exact position of the intensity threshold for X-ray production. This seems to be linked to the inaccurate treatment of the shielding of the ions by the surrounding slow electrons, which affects the predicted duration of the cluster disintegration [Prigent et al., 2008].

Nevertheless, the trend of the intensity dependence of the X-ray yield is well reproduced for all pulse durations. It appears that it is controlled by two factors: the number of emitting clusters and the number of X-rays emit-

ted per cluster. The number of emitting clusters is linked to the “effective focal volume”, which corresponds to the volume in which the laser intensity exceeds the intensity threshold for X-ray production. This seems to be the dominating factor for the absolute X-ray production: both the experimental and the theoretical X-ray yields follow closely the intensity dependence of the effective focal volume. The exact intensity dependence of the number of X-rays emitted per cluster above the threshold is therefore of minor importance and only differences in the saturation value for different parameters are noticeable.

This insight allows us to make qualitative predictions for the evolution of the X-ray yield with the pulse duration. At constant pulse energy, we find that the competition between the growing number of produced X-rays per cluster and the decreasing number of emitting clusters leads to an optimal pulse duration where the X-ray emission is maximized. The predicted optimal duration is in very good agreement with the experiments and we thus rule out any resonance effect as the cause of this maximum in the present parameter range [Prigent et al., 2008].

In opposition to the nanoplasma resonance theory, we did not find an optimum cluster size for which the X-ray production per cluster is maximized. The comparison with experimental data on the cluster size dependence of the total X-ray yield reveals the need for further experimental and theoretical investigation of the clustering efficiency of the cluster sources and its parameter dependencies.

Not only the total X-ray yield, but also the charge state distributions of the ions with an inner-shell vacancy can be accessed both experimentally and theoretically. Our simulation shows that ionization of the cluster ions is mainly due to electron-impact ionization. Electron-impact excitation from the L-shell to the M-shell further helps ionization. At high laser intensities, our model reproduces the experimentally observed high ionic charge states. However, the L-shell depletion at low laser intensities is strongly underestimated by our simulations. Here a further quest for efficient ionization mechanisms, and an examination of the experimental spectra taking into account the excited states formed by recombination are needed.

The influence of the laser polarization on the X-ray emission could not be addressed in this work and remains open for further research. As we make use of the axial symmetry of the electric fields, our simulation is limited to linearly polarized laser light. We can nevertheless expect the heating of the electrons at the cluster surface in sheath regions with an enhanced laser field to be also effective for circular polarization. Indeed, experiments show that, for the same pulse energy, the absolute X-ray yields are only 20% smaller for circular polarization than for linear polarization [Prigent, 2004].

This confirms that electron heating is still efficient. The slight decrease in yield could be explained by the $\sqrt{2}$ times smaller laser field strength for circular polarization. Furthermore, high resolution experiments reveal that the smaller yield is related to a reduction of the emission from charge states 12+ to 14+, while the emission from Ar^{15+} and Ar^{16+} ions is nearly identical for both polarizations. This influence of the laser polarization on the charge state distribution of the emitting ions remains an open question.

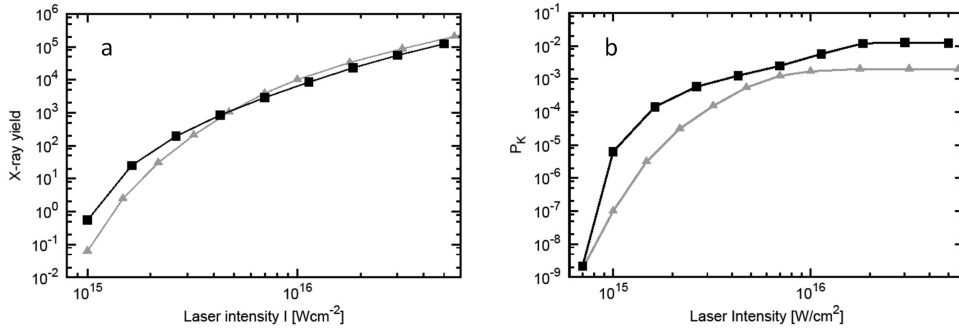


Figure 15.1: a) Intensity dependence of the absolute X-ray yield. A clustering ratio of $\eta = 0.05$ was assumed. b) Intensity dependence of the number of K-shell vacancies produced per cluster atom. The simulations have been performed with laser pulses of wavelength $\lambda = 400$ nm (black) and $\lambda = 800$ nm (gray). ($\tau = 61$ fs, $N = 2.8 \cdot 10^5$).

Open questions also remain concerning the wavelength dependence of the X-ray yield. The X-ray spectroscopy experiments with laser pulses of wavelength 400 nm could only be performed with pulse durations longer than $\tau \simeq 150$ fs, as the $\lambda = 400$ nm pulses are obtained by frequency doubling of an infrared pulse. The passage through the nonlinear crystal strongly affects the pulse shape, which becomes non-Gaussian and elongated depending on the pulse energy [Prigent, 2004]. As for these long pulse durations, the inaccurate treatment of the ion shielding already greatly affected our simulation results for 800 nm pulses, we restricted ourselves to preliminary studies of 400 nm pulses with a duration of $\tau = 60$ fs. For this duration, we found very similar total X-ray yields for pulses of wavelength $\lambda = 400$ nm and $\lambda = 800$ nm (fig. 15.1a). When calculating the total X-ray yield for 400 nm we took into account the reduced beamwaist and Rayleigh length (eq.11.3) of the laser beam. The smaller focal volume masks the more efficient X-ray emission per cluster at 400 nm, which becomes apparent when examining the number of

inner-shell vacancies P_K produced per cluster atom (fig. 15.1b). Changing the laser frequency affects the oscillatory movement of the electrons, and for a pulse with a wavelength of 400 nm, the ponderomotive energy $U_P = F^2/4\omega^2$ is lowered by a factor 4 (for the same peak field strength). At the same time, however, the screening of the laser field by the polarization of the cluster is less effective (see eq. (6.3)), which leads to a 2 to 4 times higher effective field inside the cluster. The mean kinetic energy of the electrons inside the cluster is consequently higher for 400 nm than for 800 nm. The enhanced field at the cluster poles (eq. 6.4) is much less sensitive to the variation of the laser frequency and is only 10-15% higher. These facts help understanding why the inner-shell vacancy production sets in at a similar threshold intensity for 800 nm and for 400 nm, but is more effective for the higher frequency, with an up to twenty times higher P_K at low intensities. At high laser intensities ($I \gtrsim 1.5 \cdot 10^{16} \text{ Wcm}^{-2}$) a surge in the number of produced vacancies can be observed for 400 nm just before P_K saturates (fig. 15.1b). This enhancement of the electron heating, that is accompanied by a very rapid cluster disintegration, disappears when the wake fields created by the fast electron fronts transiting the cluster is artificially suppressed in the simulation. A further investigation of these effects may reveal dynamics that were not apparent in the $\lambda = 800 \text{ nm}$ regime on which we focused in this thesis. Systematic studies with varying laser wavelengths and polarizations could shed further light on the interplay of the wake fields with the global electron dynamics.

Appendix

Appendix A

Time propagation

The equation of motion (2.1) of each particle is propagated with the velocity Verlet algorithm. The difference to the Verlet algorithm [Verlet, 1967] is that the velocity is also evaluated. The propagation from t to $(t + \Delta t)$ for particle j is done in the following way (for electrons $q_j = -1$ and $M_j = 1$):

$$\mathbf{a}_j(t) = \frac{q_j}{M_j} (\mathbf{F}_{\text{mean}}(\mathbf{r}_j(t)) + \mathbf{F}_L(t)) \quad (\text{A.1a})$$

$$\mathbf{v}_j(t) = \mathbf{v}_j(t - \frac{\Delta t}{2}) + \mathbf{a}_j(t) \frac{\Delta t}{2} \quad (\text{A.1b})$$

$$\text{scattering events: } \mathbf{v}_j(t) \rightarrow \mathbf{v}'_j(t) \quad (\text{A.1c})$$

$$\mathbf{r}_j(t + \Delta t) = \mathbf{r}_j(t) + \mathbf{v}'_j(t) \Delta t + \mathbf{a}_j(t) \frac{\Delta t^2}{2} \quad (\text{A.1d})$$

$$\mathbf{v}_j(t + \frac{\Delta t}{2}) = \mathbf{v}'_j(t) + \mathbf{a}_j(t) \frac{\Delta t}{2} \quad (\text{A.1e})$$

With this method, the error in the position of the particle is only of the order of Δt^4 . Eq. (A.1c) symbolizes the transformation of the velocity by the stochastic scattering events which are considered to act instantaneously. After going through these steps for all particles the new mean field \mathbf{F}_{mean} is evaluated from the spatial distribution $\{\mathbf{r}^{(i)}(t + \Delta t), \mathbf{r}^{(e)}(t + \Delta t)\}$ of all simulated particles by solving the Poisson equation as described in chapter 3.

Appendix B

The chaining mesh

For the stochastic treatment of the scattering events as described in chapters 4 and 5, particle pairs (electron-electron, ion-ion or electron-ion) have to be formed. We form these pairs randomly from particles in spatial proximity in order to get a good sampling of the local particle distribution functions. The straightforward way of choosing a partner by going through all simulated particles and checking the distance to the considered particle would be computationally way too costly, as this procedure has to be performed at every time step for every particle which would lead to a quadratic scaling with the total number of particles. We therefore introduce a chaining mesh [Hockney and Eastwood, 1988] additionally to the 2D charge-potential mesh used for the computation of the mean field. The chaining mesh is a 3D cubic grid which discretizes the simulation volume into cubic cells of side length a_{near} . For a given particle, the partner particle is chosen randomly from the same cell. When going to larger clusters (with same particle density) the computational cost of the pairing now increases only linearly with the number of particles. A typical value is $a_{\text{near}} = 20$ a.u. which provides approximately 32 ions per cell inside the cluster (given the typical atomic density $n_{\text{Ar}} = 3.9 \times 10^{-3}$ a.u. and a representation fraction of $\alpha_{\text{rep}} = 1$) and should exceed the Debye screening length inside the cluster.

The efficient access to the particles in a given chaining cell is provided by two linked lists [Hockney and Eastwood, 1988] which associate the cell indices (c_x, c_y, c_z) with the particle indices k (for electrons) or j (for ions). Each linked list makes use of two integer arrays: the head-of-chain table $\text{EHOC}(c_x, c_y, c_z)$ or $\text{IHOC}(c_x, c_y, c_z)$, and the particle link array $\text{ELL}(k)$ or $\text{ILL}(j)$. Let us illustrate the method for the linked list of the ions (see fig. B.1). For a given cell (c_x, c_y, c_z) the entry $\text{IHOC}(c_x, c_y, c_z) = j_1$ gives the index j_1 of the first ion in the cell. The entry $\text{ILL}(j_1) = j_2$ links to the index j_2 of the next ion in the same cell. By reading recursively the values of ILL ,

one sweeps through all particles of cell (c_x, c_y, c_z) . The last particle j_n in the cell links to the value zero ($\text{ILL}(j_n) = 0$) and thus signals that all particles in the cell have been located. The linked lists need to be updated for both electrons and ions at every time step. This is done in the following way (for ions, and identically for electrons):

- Initialize both IHOC and ILL to 0.
- Cycle through all ions $j = 1, \dots, N_{\text{simul}}$ and:
 - Determine the corresponding chaining cell $(c_x, c_y, c_z) = \text{int}(\frac{x_j}{a_{\text{near}}}, \frac{y_j}{a_{\text{near}}}, \frac{z_j}{a_{\text{near}}})$.
 - Set $\text{ILL}(j) = \text{IHOC}(c_x, c_y, c_z)$.
 - Set $\text{IHOC}(c_x, c_y, c_z) = j$.

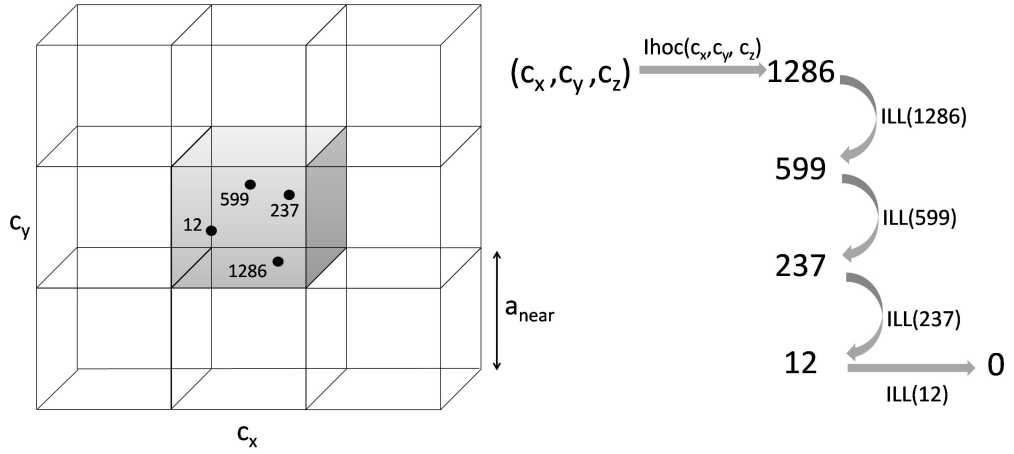


Figure B.1: Stepping through the four ions ($j_1 = 1286$, $j_2 = 599$, $j_3 = 237$ and $j_4 = 12$) located in cell (c_x, c_y, c_z) with help of the arrays IHOC and ILL.

Appendix C

Calculating the mean field

C.1 Cloud-in-Cell charge assignment

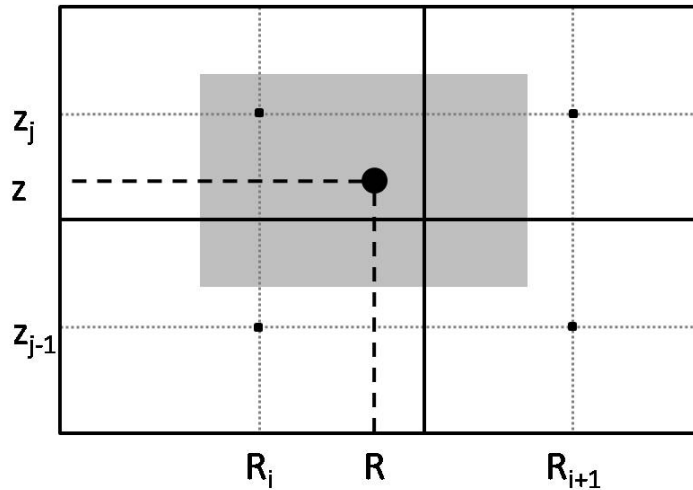


Figure C.1: The particle at the position (R, z) is spread over the volume of a cell (gray), and its overlap with the four cells $(i, j), (i_{next}, j), (i, j_{next})$ and (i_{next}, j_{next}) determines the fraction of the charge assigned to each cell.

For the evaluation of the discrete charge density $\rho_{i,j}$ a particle is not treated as a point particle, but as a homogeneous charge distribution over a given volume centered on the particle's position. By choosing the volume to be equal to the volume $V_{cell} = V_{i,j}$ of the discretization cell, the charge of the test particle is spread over four neighboring cells (fig. C.1). The fraction of the particle charge q_k assigned to each cell depends on the position of the

particle k relative to the cell centers:

$$\begin{aligned}
\rho_{i,j}^{(k)} &= \frac{q_k}{V_{cell}} \pi |R^2 - R_{i_{next}}^2| |z - z_{j_{next}}| \\
\rho_{i_{next},j}^{(k)} &= \frac{q_k}{V_{cell}} \pi |R^2 - R_i^2| |z - z_{j_{next}}| \\
\rho_{i,j_{next}}^{(k)} &= \frac{q_k}{V_{cell}} \pi |R^2 - R_{i_{next}}^2| |z - z_j| \\
\rho_{i_{next},j_{next}}^{(k)} &= \frac{q_k}{V_{cell}} \pi |R^2 - R_i^2| |z - z_j|
\end{aligned} \tag{C.1}$$

Depending on the position of the particle within the cell (i, j) , i_{next} is equal to $i - 1$ or $i + 1$ and $j_{next} = j - 1$ or $j + 1$. The total charge distribution is obtained by repeating this procedure for all test particles (electrons and ions).

After calculating the mean field by solving the Poisson equation, its contribution to the force acting on particle k located at (R, z) is obtained by interpolating the discrete mean field using the same algorithm (C.1) as for charge assignment:

$$\begin{aligned}
\mathbf{K}_k^{(\text{mean})} &= \frac{q_k}{V_{cell}} \pi |R^2 - R_{i_{next}}^2| |z - z_{j_{next}}| \mathbf{F}_{\text{mean}}(R_{i_{next}}, z_{j_{next}}) \\
&+ \frac{q_k}{V_{cell}} \pi |R^2 - R_i^2| |z - z_{j_{next}}| \mathbf{F}_{\text{mean}}(R_i, z_{j_{next}}) \\
&+ \frac{q_k}{V_{cell}} \pi |R^2 - R_{i_{next}}^2| |z - z_j| \mathbf{F}_{\text{mean}}(R_{i_{next}}, z_j) \\
&+ \frac{q_k}{V_{cell}} \pi |R^2 - R_i^2| |z - z_j| \mathbf{F}_{\text{mean}}(R_i, z_j).
\end{aligned} \tag{C.2}$$

C.2 Cyclic reduction

After reducing the system of 511 equations corresponding to the discretized Poisson equation as described in chapter 3.2, one gets at level r of reduction:

$$\phi_{(j-2^r)} + \mathbf{A}^{(r)} \phi_{(j)} + \phi_{(j+2^r)} = \mathbf{d}_{(j)}^{(r)} \tag{C.3}$$

with

$$\mathbf{A}^{(r)} = 2\mathbf{E} - (\mathbf{A}^{(r-1)})^2 \tag{C.4}$$

and

$$\mathbf{d}_{(j)}^{(r)} = \mathbf{d}_{(j-2^r)}^{(r-1)} - \mathbf{A}^{(r-1)} \mathbf{d}_{(j)}^{(r-1)} + \mathbf{d}_{(j+2^r)}^{(r-1)}. \tag{C.5}$$

C.2.1 Solving equations of type $\mathbf{A}^{(r)}\mathbf{v} = \mathbf{y}$

One can show [Cohen, 1994] that the matrix $\mathbf{A}^{(r)}$ can be expressed as product of factors depending on the tridiagonal matrix $\mathbf{A}^{(0)} = \mathbf{A}$ only ¹:

$$\mathbf{A}^{(r)} = 2\mathbf{E} - (\mathbf{A}^{(r-1)})^2 = -\prod_{k=1}^{2^r} \left(\mathbf{A} + 2 \cos \theta_k^{(r)} \mathbf{E} \right) \quad (\text{C.6})$$

with

$$\theta_k^{(r)} = \frac{2k-1}{2^{r+1}}\pi. \quad (\text{C.7})$$

This factorization allows to solve equations of type $\mathbf{A}^{(r)}\mathbf{v} = -\prod_{k=1}^{2^r} \mathbf{A}_k^{(r)}\mathbf{v} = \mathbf{y}$ by successive solution of 2^r tridiagonal systems:

$$\begin{aligned} \mathbf{A}_1^{(r)}\mathbf{v}^{(1)} &= -\mathbf{y} \quad \rightarrow \mathbf{v}^{(1)} \\ \mathbf{A}_2^{(r)}\mathbf{v}^{(2)} &= \mathbf{v}^{(1)} \quad \rightarrow \mathbf{v}^{(2)} \\ &\vdots \\ \mathbf{A}_{2^r}^{(r)}\mathbf{v} &= \mathbf{v}^{(2^r-1)} \quad \rightarrow \mathbf{v} \end{aligned} \quad (\text{C.8})$$

The tridiagonal systems have the following form (for $i = 0, \dots, 255$):

$$b_i v_{i-1}^{(k)} + (c_i - 2 + 2 \cos \theta_k^{(r)}) v_i^{(k)} + a_i v_{i+1}^{(k)} = v_i^{(k-1)}. \quad (\text{C.9})$$

Such systems are efficiently solved with the Thomas algorithm [Hockney and Eastwood, 1988] that involves two loops, one for forward elimination:

$$\begin{aligned} w_0 &= \frac{a_0}{c_0 - 2 + 2 \cos \theta_k^{(r)}} \\ g_0 &= \frac{v_0^{(k-1)}}{c_0 - 2 + 2 \cos \theta_k^{(r)}} \\ w_i &= \frac{a_i}{c_i - 2 + 2 \cos \theta_k^{(r)} - b_i w_{i-1}} \quad i = 1, \dots, 254 \\ g_i &= \frac{v_i^{(k-1)} - b_i g_{i-1}}{c_i - 2 + 2 \cos \theta_k^{(r)} - b_i w_{i-1}} \quad i = 1, \dots, 255 \end{aligned} \quad (\text{C.10})$$

and one for back substitution:

$$\begin{aligned} v_{255}^{(k)} &= g_{255} \\ v_i^{(k)} &= g_i - w_i v_{i+1}^{(k)} \quad i = 254, \dots, 0 \end{aligned} \quad (\text{C.11})$$

¹The corresponding formula (6-91b) in Hockney and Eastwood [1988] appears to be in error.

C.2.2 Buneman scheme

The evaluation of $\mathbf{d}_{(j)}^{(r+1)} = \mathbf{d}_{(j-2^r)}^{(r)} - \mathbf{A}^{(r)}\mathbf{d}_{(j)}^{(r)} + \mathbf{d}_{(j+2^r)}^{(r)}$ gets unstable after several reductions, as the matrix $\mathbf{A}^{(r)}$ is ill-conditioned for large r [Cohen, 1994]. This is solved by reorganizing the evaluation of $\mathbf{d}_{(j)}^{(r+1)}$ according to the Buneman scheme. At level r of reduction one gets:

$$\phi_{(j-2^r)} + \mathbf{A}^{(r)}\phi_{(j)} + \phi_{(j+2^r)} = \mathbf{d}_{(j)}^{(r)} = \mathbf{A}^{(r)}\mathbf{p}_{(j)}^{(r)} + \mathbf{q}_{(j)}^{(r)} \quad (\text{C.12})$$

with:

$$\begin{aligned} \mathbf{p}_{(j)}^{(0)} &= 0 \\ \mathbf{q}_{(j)}^{(0)} &= \mathbf{d}_{(j)} \\ \mathbf{p}_{(j)}^{(r+1)} &= \mathbf{p}_{(j)}^{(r)} + (\mathbf{A}^{(r)})^{-1}(\mathbf{q}_{(j)}^{(r)} - \mathbf{p}_{(j-2^r)}^{(r)} - \mathbf{p}_{(j+2^r)}^{(r)}) \\ \mathbf{q}_{(j)}^{(r+1)} &= \mathbf{q}_{(j-2^r)}^{(r)} + \mathbf{q}_{(j+2^r)}^{(r)} - 2\mathbf{p}_{(j)}^{(r+1)} \end{aligned} \quad (\text{C.13})$$

$\mathbf{p}_{(j)}^{(r+1)}$ is computed by solving $(\mathbf{A}^{(r)})\mathbf{v} = \mathbf{q}_{(j)}^{(r)} - \mathbf{p}_{(j-2^r)}^{(r)} - \mathbf{p}_{(j+2^r)}^{(r)}$ with the Thomas algorithm, and then setting $\mathbf{p}_{(j)}^{(r+1)} = \mathbf{p}_{(j)}^{(r)} + \mathbf{v}$.

C.2.3 Summary

Solving the Poisson equation can be summarized in the following steps:

- fix the boundary conditions (3.12),
- initialize $\mathbf{p}_{(j)}^{(0)}$ and $\mathbf{q}_{(j)}^{(0)}$,
- make the $r = 1, \dots, 8$ reduction steps: evaluate $\mathbf{p}_{(j)}^{(r)}$ and $\mathbf{q}_{(j)}^{(r)}$ at $j = -256 + 2^r, -256 + 2 \cdot 2^r, \dots, 256 - 2^r$.
- Make the 9 backsubstitution steps by solving (C.12) for $\mathbf{v} = \phi_{(j)} - \mathbf{p}_{(j)}^{(r)}$ with the Thomas algorithm.
- At $r = 0$ you have obtained all $\phi_{i,j}$.

Acknowledgments

I would like to thank everyone who helped me complete this thesis by giving me scientific and personal support in the last years. I start with expressing my gratitude to my thesis supervisor Joachim Burgdörfer, for providing me with guidance, great opportunities, and an ever-open ear. For a great collaboration and inspiring discussions, I am deeply indebted to Christophe Prigent, Emily Lamour, Jean-Pierre Rozet and Dominique Vernhet. I also owe very special thanks to Emily and Dominique for their exceptional hospitality during my stays in Paris. I had the great opportunity to participate in the International Max Planck Research School on Advanced Photon Science and would like to extend thanks to Matthias Kling, Tobias Schätz and Maria Wild for their commitment to the program. I was very fortunate to work within such an inspiring and fun group at the Institute for Theoretical Physics - thank you all! Last but not least, deep thanks go to my family and friends for their everlasting support, encouragement, and necessary distraction.

Bibliography

- AMMOSOV, M. V., DELONE, N. B., AND KRAINOV, V. P. 1986. Tunnel ionization of complex atoms and of atomic ions in an alternating electromagnetic field. *Sov. Phys. JETP* 64:1191–1194.
- AUGST, S., MEYERHOFER, D. D., STRICKLAND, D., AND CHIN, S. L. 1991. Laser ionization of noble gases by Coulomb-barrier suppression. *J. Opt. Soc. Am. B* 8:858.
- BETHE, H. 1930. Zur Theorie des Durchgangs schneller Korpuskularstrahlen durch Materie. *Annalen der Physik* 397:325–400.
- BETHE, H. AND SALPETER, E. 1975. Quantum Mechanics of One- and Two-Electron Atoms. Springer, Berlin.
- BHALLA, C. P. 1973. K-shell Auger rates, transition energies, and fluorescence yields of variously ionized states of argon. *Phys. Rev. A* 8:2877–2882.
- BOLDAREV, A. S., GASILOV, V. A., BLASCO, F., STENZ, C., DORCHIES, F., SALIN, F., FAENOV, A. Y., PIKUZ, T. A., MAGUNOV, A. I., AND SKOBELEV, I. Y. 2001. Modeling cluster jets as targets for high-power ultrashort laser pulses. *JETP Letters* 73:514–518.
- BOLDAREV, A. S., GASILOV, V. A., FAENOV, A. Y., FUKUDA, Y., AND YAMAKAWA, K. 2006. Gas-cluster targets for femtosecond laser interaction: Modeling and optimization. *Review of Scientific Instruments* 77:083112.
- BRUNEL, F. 1987. Not-so-resonant, resonant absorption. *Phys. Rev. Lett.* 59:52–55.
- BUCK, U. AND KROHNE, R. 1996. Cluster size determination from diffractive He atom scattering. *The Journal of Chemical Physics* 105:5408–5415.
- BURGDÖRFER, J. AND GIBBONS, J. 1990. Electron transport in the presence of a Coulomb field. *Phys. Rev. A* 42:1206–1221.

- BURGDÖRFER, J., REINHOLD, C. O., STERNBERG, J., AND WANG, J. 1995. Semiclassical theory of elastic electron-atom scattering. *Phys. Rev. A* 51:1248–1252.
- CHEN, M. H. AND CRASEMANN, B. 1974. Multiplet effects on the $L_{2,3}$ fluorescence yield of multiply ionized Ar. *Phys. Rev. A* 10:2232–2239.
- COHEN, S. 1994. Cyclic reduction. citeseer.ist.psu.edu/cohen94cyclic.html.
- DEBYE, P. AND HÜCKEL, E. 1923. Das Grenzgesetz für die elektrische Leitfähigkeit. *Phys. Z.* 24:305–317.
- DEISS, C. 2005. Laser-cluster interaction - production of hot electrons by short laser pulses. Master's thesis, Vienna University of Technology. available online at <http://www.ub.tuwien.ac.at/dipl/2005/AC04492699.pdf>.
- DEISS, C. AND BURGDÖRFER, J. 2007. Simulation of the dynamics of laser-cluster interaction. *Journal of Physics: Conference Series* 88:012036 (8pp).
- DEISS, C., ROHRINGER, N., AND BURGDÖRFER, J. 2005. Cluster-laser interaction: fast production of hot electrons by short laser pulses. *Nucl. Instr. and Meth. in Phys. Res. B* 235:210 – 215. The Physics of Highly Charged Ions.
- DEISS, C., ROHRINGER, N., AND BURGDÖRFER, J. 2006a. Interaction of ultra-short laser pulses with clusters: short-time dynamics of a nanoplasma. *AIP Conf. Proc.* 876:143–153.
- DEISS, C., ROHRINGER, N., BURGDÖRFER, J., LAMOUR, E., PRIGENT, C., ROZET, J.-P., AND VERNHET, D. 2006b. Laser-cluster interaction: X-ray production by short laser pulses. *Phys. Rev. Lett.* 96:013203.
- DEISS, C., ROHRINGER, N., BURGDÖRFER, J., LAMOUR, E., PRIGENT, C., ROZET, J.-P., AND VERNHET, D. 2006c. X-ray generation by laser-cluster interaction. *J. Phys. IV France* 138:55.
- DERE, K. P., LANDI, E., MASON, H. E., MONSIGNORI FOSSI, B. C., AND YOUNG, P. R. 1997. CHIANTI - an atomic database for emission lines. *Astronomy & Astrophysics Supplement Series* 125:149–173.

- DITMIRE, T., DONNELLY, T., RUBENCHIK, A. M., FALCONE, R. W., AND PERRY, M. D. 1996. Interaction of intense laser pulses with atomic clusters. *Phys. Rev. A* 53:3379–3402.
- DITMIRE, T., TISCH, J. W. G., SPRINGATE, E., MASON, M. B., HAY, N., SMITH, R. A., MARANGOS, J., AND HUTCHINSON, M. H. R. 1997. High-energy ions produced in explosions of superheated atomic clusters. *Nature* 386:54–56.
- DOBOSZ, S., LEZIUS, M., SCHMIDT, M., MEYNADIER, P., PERDRIX, M., NORMAND, D., ROZET, J.-P., AND VERNHET, D. 1997. Absolute keV photon yields from ultrashort laser-field-induced hot nanoplasmas. *Phys. Rev. A* 56:R2526–R2529.
- DORCHIES, F., BLASCO, F., CAILLAUD, T., STEVEFELT, J., STENZ, C., BOLDAREV, A. S., AND GASILOV, V. A. 2003. Spatial distribution of cluster size and density in supersonic jets as targets for intense laser pulses. *Phys. Rev. A* 68:023201.
- DORCHIES, F., CAILLAUD, T., BLASCO, F., BONTÉ, C., JOUIN, H., MICHEAU, S., PONS, B., AND STEVEFELT, J. 2005. Investigation of laser-irradiated ar cluster dynamics from K-shell x-ray emission measurements. *Physical Review E (Statistical, Nonlinear, and Soft Matter Physics)* 71:066410.
- FENNEL, T., DÖPPNER, T., PASSIG, J., SCHAAL, C., TIGGESBÄUMKER, J., AND MEIWES-BROER, K.-H. 2007a. Plasmon-enhanced electron acceleration in intense laser metal-cluster interactions. *Physical Review Letters* 98:143401.
- FENNEL, T., RAMUNNO, L., AND BRABEC, T. 2007b. Highly charged ions from laser-cluster interactions: Local-field-enhanced impact ionization and frustrated electron-ion recombination. *Physical Review Letters* 99:233401.
- FOMICHEV, S. V., ZARETSKY, D. F., BAUER, D., AND BECKER, W. 2005. Classical molecular-dynamics simulations of laser-irradiated clusters: Nonlinear electron dynamics and resonance-enhanced low-order harmonic generation. *Physical Review A (Atomic, Molecular, and Optical Physics)* 71:013201.
- FUKUDA, Y., AKAHANE, Y., AOYAMA, M., INOUE, N., UEDA, H., NAKAI, Y., TSUJI, K., YAMAKAWA, K., HIRONAKA, Y., KISHIMURA, H., MORISHITA, H., ICHI KONDO, K., AND NAKAMURA, K. G. 2004.

- Relativistic laser plasma from micron-sized argon clusters as a debris-free x-ray source for pulse x-ray diffraction. *Applied Physics Letters* 85:5099–5101.
- FUKUDA, Y., FAENOV, A. Y., PIKUZ, T., KANDO, M., KOTAKI, H., DAITO, I., MA, J., CHEN, L. M., HOMMA, T., KAWASE, K., KAMESHIMA, T., KAWACHI, T., DAIDO, H., KIMURA, T., TAJIMA, T., KATO, Y., AND BULANOV, S. V. 2008. Soft x-ray source for nanostructure imaging using femtosecond-laser-irradiated clusters. *Applied Physics Letters* 92:121110.
- FUKUDA, Y., KISHIMOTO, Y., MASAKI, T., AND YAMAKAWA, K. 2006. Structure and dynamics of cluster plasmas created by ultrashort intense laser fields. *Phys. Rev. A* 73:031201.
- GEORGESCU, I., SAALMANN, U., AND ROST, J. M. 2007. Clusters under strong VUV pulses: A quantum-classical hybrid description incorporating plasma effects. *Physical Review A (Atomic, Molecular, and Optical Physics)* 76:043203.
- GRAY, D. E. 1963. American institute of physics handbook. AIP, New York.
- GUPTA, A., ANTONSEN, T. M., TAGUCHI, T., AND PALASTRO, J. 2006. Effect of pulse duration on resonant heating of laser-irradiated argon and deuterium clusters. *Physical Review E (Statistical, Nonlinear, and Soft Matter Physics)* 74:046408.
- HAGENA, O. F. 1992. Cluster ion sources (invited). *Rev. Sci. Instrum.* 63:2374–2379.
- HAGENA, O. F. AND OBERT, W. 1972. Cluster formation in expanding supersonic jets: Effect of pressure, temperature, nozzle size, and test gas. *The Journal of Chemical Physics* 56:1793–1802.
- HANSEN, S. B. AND SHLYAPTSEVA, A. S. 2004. Effects of the electron energy distribution function on modeled X-ray spectra. *Phys. Rev. E* 70:036402.
- HOCKNEY, R. W. AND EASTWOOD, J. W. 1988. Computer simulation using particles. Institute of Physics Publishing, Bristol and Philadelphia.
- ISLAM, M. R., SAALMANN, U., AND ROST, J. M. 2006. Kinetic energy of ions after Coulomb explosion of clusters induced by an intense laser pulse. *Phys. Rev. A* 73:041201.

- IVANOV, L. N., IVANOVA, E. P., AND KNIGHT, L. V. 1993. Energy approach to consistent QED theory for calculation of electron-collision strengths: Ne-like ions. *Phys. Rev. A* 48:4365–4378.
- JUNGREUTHMAYER, C., GEISLER, M., ZANGHELLINI, J., AND BRABEC, T. 2004. Microscopic analysis of large-cluster explosion in intense laser fields. *Phys. Rev. Lett.* 92:133401.
- KOLWAS, K. 1996. Size dependent index of refraction and absorption of a spherical metal cluster. *Z. Phys. D* 38:233–240.
- KRAINOV, V. P. AND SMIRNOV, M. B. 2002. Cluster beams in the super-intense femtosecond laser pulse. *Phys. Rep.* 370:237–331.
- KRISHNAMURTHY, M., JHA, J., MATHUR, D., JUNGREUTHMAYER, C., RAMUNNO, L., ZANGHELLINI, J., AND BRABEC, T. 2006. Ion charge state distribution in the laser-induced coulomb explosion of argon clusters. *Journal of Physics B: Atomic, Molecular and Optical Physics* pp. 625–632.
- KUMARAPPAN, V., KRISHNAMURTHY, M., AND MATHUR, D. 2001a. Asymmetric high-energy ion emission from argon clusters in intense laser fields. *Phys. Rev. Lett.* 87:085005.
- KUMARAPPAN, V., KRISHNAMURTHY, M., AND MATHUR, D. 2003. Asymmetric emission of high-energy electrons in the two-dimensional hydrodynamic expansion of large xenon clusters irradiated by intense laser fields. *Phys. Rev. A* 67:043204.
- KUMARAPPAN, V., KRISHNAMURTHY, M., MATHUR, D., AND TRIBEDI, L. C. 2001b. Effect of laser polarization on X-ray emission from Ar_n ($n = 200 - 104$) clusters in intense laser fields. *Phys. Rev. A* 63:023203.
- LAMOUR, E., PRIGENT, C., ROZET, J. P., AND VERNHET, D. 2005. Physical parameter dependence of the X-ray generation in intense laser-cluster interaction. *Nucl. Instr. and Meth. B* 235:408–413.
- LAMOUR, E., PRIGENT, C., ROZET, J. P., AND VERNHET, D. 2007. X-ray production in short laser pulse interaction with rare gas clusters. *Journal of Physics: Conference Series* 88:012035 (9pp).
- LANDI, E., DEL ZANNA, G., YOUNG, P. R., DERE, K. P., MASON, H. E., AND LANDINI, M. 2006. CHIANTI-An atomic database for emission lines. VII. New data for X-rays and other improvements. *The Astrophysical Journal Supplement Series* 162:261–280.

- LARKINS, F. P. 1971. Charge state dependence of X-ray and Auger electron emission spectra for rare-gas atoms. i. The argon atom. *Journal of Physics B: Atomic and Molecular Physics* 4:1–13.
- LAST, I. AND JORTNER, J. 2007. Scaling procedure for simulations of extreme ionizations and coulomb explosion of large clusters. *Physical Review A (Atomic, Molecular, and Optical Physics)* 75:042507.
- LEZIUS, M., DOBOSZ, S., NORMAND, D., AND SCHMIDT, M. 1997. Hot nanoplasmas from intense laser irradiation of argon clusters. *J. of Phys. B* 30:L251–L258.
- LOTZ, W. 1968a. Electron-impact ionization cross-sections and ionization rate coefficients for atoms and ions from hydrogen to calcium. *Zeitschrift für Physik A* 216:241–247.
- LOTZ, W. 1968b. Subshell binding energies of atoms and ions from hydrogen to zinc. *J. Opt. Soc. Am.* 58:915.
- MEGI, F., BELKACEM, M., BOUCHENE, M. A., SURAUD, E., AND ZWICKNAGEL, G. 2003. On the importance of damping phenomena in clusters irradiated by intense laser fields. *J. of Phys. B* 36:273–282.
- MEWE, R. 1972. Interpolation formulae for the electron impact excitation of ions in the H-, He-, Li-, and Ne- sequences. *Astronomy and Astrophysics* 20:215–221.
- MICHEAU, S., JOUIN, H., AND PONS, B. 2008. Modified nanoplasma model for laser-cluster interaction. *Physical Review A (Atomic, Molecular, and Optical Physics)* 77:053201.
- MITCHER, M. 1973. Partially Ionized Gases. John Wiley & Sons, Inc.
- MORAWETZ, K. 2000. Nonlinear relaxation field in charged systems under high electric fields. *Phys. Rev. E* 62:6135–6148.
- MOTT, N. AND MASSEY, H. 1965. Theory of Atomic Collisions. Oxford University Press, New York.
- NANBU, K. 1997. Theory of cumulative small-angle collisions in plasmas. *Phys. Rev. E* 55:4642–4652.
- O’CONNELL, D., GANS, T., VENDER, D., CZARNETZKI, U., AND BOSWELL, R. 2007. Plasma ionization through wave-particle interaction in a capacitively coupled radio-frequency discharge. *Physics of Plasmas* 14:034505.

- J. Posthumus (ed.) 2001. Molecules and clusters in intense laser fields. Cambridge University Press.
- PRESS, W. H., TEUKOLSKY, S. A., VETTERLING, W. T., AND FLANERY, B. P. 1986. Numerical Recipes in Fortran 90. Cambridge University Press.
- PRIGENT, C. 2004. Emission X, un outil et une sonde pour l'interaction laser-agrégats. PhD thesis, Université Pierre et Marie Curie, Paris VI. available online at <http://tel.archives-ouvertes.fr/tel-00008159/>.
- PRIGENT, C., DEISS, C., LAMOUR, E., ROZET, J.-P., VERNHET, D., AND BURGDÖRFER, J. 2008. Effect of pulse duration on the x-ray emission from ar clusters in intense laser fields. *Physical Review A (Atomic, Molecular, and Optical Physics)* 78:053201.
- PURCELL, E. 1985. Berkeley Physics Course, Vol. 2. McGraw-Hill.
- RALCHENKO, Y., KRAMIDA, A., READER, J., AND NIST ASD TEAM 2005. NIST Atomic Spectra Database (version 3.0.3). available online at <http://physics.nist.gov/asd3>.
- ROSE-PETRUCK, C., SCHAFER, K. J., WILSON, K. R., AND BARTY, C. P. J. 1997. Ultrafast electron dynamics and inner-shell ionization in laser driven clusters. *Phys. Rev. A* 55:1182–1190.
- ROZET, J.-P., CORNILLE, M., DOBOSZ, S., DUBAU, J., GAUTHIER, J.-C., JACQUEMOT, S., LAMOUR, E., LEZIUS, M., NORMAND, D., SCHMIDT, M., AND VERNHET, D. 2001. State selective measurements of HCI produced by strong ultrashort laser-clusters interaction. *Physica Scripta* T92:113–118.
- SAALMANN, U. AND ROST, J.-M. 2003. Ionization of clusters in intense laser pulses through collective electron dynamics. *Phys. Rev. Lett.* 91:223401.
- SAALMANN, U., SIEDSCHLAG, C., AND ROST, J. M. 2006. Mechanisms of cluster ionization in strong laser pulses. *J. of Phys. B* 39:R39–R77.
- SALVAT, F. AND MAYOL, R. 1993. Elastic scattering of electrons and positrons by atoms. *Comp. Phys. Commun.* 74:358–374.
- SCHUTTE, S. AND BUCK, U. 2002. Strong fragmentation of large rare gas clusters by high energy electron impact. *International Journal of Mass Spectrometry* 220:183–192.

- SIEDSCHLAG, C. AND ROST, J. M. 2003. Enhanced ionization in small rare-gas clusters. *Phys. Rev. A* 67:013404.
- SOBEL'MAN, I. I., VAINSHTEIN, L. A., AND YUKOV, E. A. 1995. Excitation of atoms and broadening of spectral lines. Springer Series on Atoms and Plasmas, Berlin.
- SPRINGATE, E., ASEYEV, S. A., ZAMITH, S., AND VRAKING, M. J. J. 2003. Electron kinetic energy measurements from laser irradiation of clusters. *Phys. Rev. A* 68:053201.
- SZYDLIK, P. P. AND GREEN, A. E. S. 1974. Independent-particle-model potentials for ions and neutral atoms with $Z \leq 18$. *Phys. Rev. A* 9:1885–1894.
- TAGUCHI, T., THOMAS M. ANTONSEN, J., AND MILCHBERG, H. M. 2004. Resonant heating of a cluster plasma by intense laser light. *Phys. Rev. Lett.* 92:205003.
- TAKIZUKA, T. AND ABE, H. 1977. A binary collision model for plasma simulation with a particle code. *J. of Comput. Phys.* 25:205–219.
- VAN DE WAAL, B. W., TORCHET, G., AND DE FERAUDY, M. F. 2000. Structure of large argon clusters Ar_N , $10^3 < N < 10^5$: experiments and simulations. *Chem. Phys. Lett.* 331:57–63.
- VAN REGEMORTER, H. 1962. Rate of collisional excitation in stellar atmospheres. *Astrophysical Journal* 136:906–915.
- VENDER, D. AND BOSWELL, R. W. 1992. Electron–sheath interaction in capacitive radio-frequency plasmas. *J. Vac. Sci. Technol.* 10:1331–1338.
- VERLET, L. 1967. Computer "Experiments" on Classical Fluids. I. Thermodynamical Properties of Lennard-Jones Molecules. *Phys. Rev.* 159:98.
- ZOU, Y., AWAYA, Y., BHALLA, C. P., KAMBARA, T., KANAI, Y., OURA, M., NAKAI, Y., ANDO, K., HITACHI, A., AND KRAVIS, S. 1995. Inner-shell vacancy distribution in energetic Ar ions by penetration in solids. *Phys. Rev. A* 51:3790–3798.

Cornelia Deiss

Contact

Institut für Theoretische Physik
Technische Universität Wien
Wiedner Hauptstraße 8-10/136
A-1040 Wien, Österreich
Tel: +43 1 58801-13633 Fax: +43 1 58801-13699
email: cornelia@concord.itp.tuwien.ac.at

Persönliche Daten

geboren am 15. Januar 1982 in Brüssel, Belgien
Österreichische Staatsbürgerschaft

Ausbildung und Beruf

- 03/2006-03/2009 Mitglied der "International Max Planck Research School on Advanced Photon Science" in Garching, Deutschland.
- 11/2005-03/2009 Universitätsassistentin am Institut für Theoretische Physik der TU Wien
- 04/2005-03/2009 Dissertation am Institut für Theoretische Physik der TU Wien.
- 03/2005 Abschluss (Dipl.-Ing.) mit Auszeichnung, Diplomarbeit am Institut für Theoretische Physik: *Laser-cluster interaction - production of hot electrons by short laser pulses* unter der Anleitung von Prof. Joachim Burgdörfer.
- 07/2003-08/2003 Praktikum bei Philips Austria
- 09/1999-03/2005 Studium der Technischen Physik an der Technischen Universität Wien
- 06/1999 Baccalauréat (französisches Abitur) mit Auszeichnung
- 09/1997-06/1999 Lycée français, Wien
- 09/1994-06/1997 Lycée français, Budapest, Ungarn
- 09/1990-06/1994 Lycée français, Neu Delhi, Indien
- 09/1988-06/1990 Lycée français, Wien

Lehrerfahrung

- 10/2006-01/2007 Übungsleiterin der Pflichtlehrveranstaltung "Quantenmechanik 1"
- 09/2001-01/2005 Tutor an der TU Wien für Physik I, Physik II, Methoden der Theoretischen Physik, Quantenmechanik

09/1999–06/2003 Betreuung und Leitung des österreichischen Schülerteams beim International Young Physicists' Tournament (IYPT), einem Physikwettbewerb für Schüler. Organisation der nationalen Wettbewerbe. Jurorin beim internationalen Wettbewerb.

Auszeichnung

Preis der Stadt Wien für hervorragende Diplomarbeiten an der Technischen Universität Wien (Okt. 2005)

Publikationen

C. Prigent, C. Deiss, E. Lamour, J.-P. Rozet, D. Vernhet, J. Burgdörfer *Effect of pulse duration on the x-ray emission from Ar clusters in intense laser fields*, Phys. Rev. A 78, 053201 (2008).

C. Deiss and J. Burgdörfer, *Simulation of the dynamics of laser-cluster interaction*, J. Phys.: Conf. Series 88, 012036 (2007).

C. Deiss, N. Rohringer, J. Burgdörfer, E. Lamour, C. Prigent, J.-P. Rozet, D. Vernhet, *Laser-cluster interaction: x-ray production by short laser pulses*, Phys. Rev. Lett. 96, 013203 (2006).

C. Deiss, N. Rohringer, J. Burgdörfer, *Interaction of ultra-short pulses with clusters: short-time dynamics of a nano-plasma*, AIP Conf. Proc. 876, 143 (2006).

C. Deiss, N. Rohringer, J. Burgdörfer, E. Lamour, C. Prigent, J.-P. Rozet, D. Vernhet, *X-ray generation by laser-cluster interaction*, J. Phys. IV France 138, 55 (2006).

C. Deiss, N. Rohringer and J. Burgdörfer, *Cluster-laser interaction: fast production of hot electrons by short laser pulses*, Nucl. Instr. and Meth. in Phys. Res. B 235, 210-215 (2005).

Eingeladene Konferenzvorträge

Simulation of the dynamics of laser-cluster interactions, auf der 25th International Conference on Photonic, Electronic and Atomic Collisions (ICPEAC 2007)

Emission X générée par interaction laser-agrégats, auf dem 8ème Colloque national sur les Sources Cohérentes et Incohérentes UV, VUV, et X (UVX 2006)

Konferenzbeiträge

X-ray generation by laser-cluster interaction, Vortrag auf der International Conference on the Interaction of Atoms, Molecules and Plasmas with Intense Ultrashort Laser Pulses (IAMPI 2006)

Laser-Cluster Interaction: x-ray production by short laser pulses, Vortrag auf der 25. Tagung ueber Energiereiche Atomare Stoesse (EAS 2006)

Laser-Cluster Interaction: the role of electron-ion collisions in the production of hot electrons, Poster auf der 24th International Conference on Photonic, Electronic and Atomic Collisions (ICPEAC 2005)

Laser-cluster interaction: fast production of hot electrons by short laser pulses Poster auf dem International Workshop on Atomic Physics 2004, Max-Planck Institut für Physik Komplexer Systeme Dresden

Cluster-laser interaction: fast production of hot electrons by short laser pulses, Vortrag auf der 12th International Conference on the Physics of Highly Charged Ions (HCI 2004)

Sprachen

Deutsch, Französisch und Englisch fließend

Grundkenntnisse in Polnisch

Wien, Januar 2009